Technische Universität München
Lehrstuhl für Elektrische
Energiespeichertechnik
Prof. Dr.-Ing. Andreas Jossen

Temperature Inhomogeneity in Lithium Ion Pouch Cells

Nora Martiny

Vollständiger Abdruck der von der Fakultät für Elektrotechnik und Informationstechnik der Technischen Universität München zur Erlangung des akademischen Grades eines

Doktor-Ingenieurs

genehmigten Dissertation.

Vorsitzender:	Prof. Dr.rer.nat Alessio Gagliardi
Prüfer der Dissertation:	
	1. Prof. Dr.-Ing. Andreas Jossen
	2. Prof. Dr.-Ing. Harry Hoster

Die Dissertation wurde am 22.09.2017 bei der Technischen Universität München eingereicht und durch die Fakultät für Elektrotechnik und Informationstechnik am 21.12.2017 angenommen.

ACKNOWLEDGEMENTS

The presented work was financially supported by the Singapore National Research Foundation under its Campus for Research Excellence And Technological Enterprise (CREATE) program.
My special thanks for supporting me constantly not only in the development process of this thesis but also personally go to Prof. Andreas Jossen, Dr. Martin Lukasiewycz, Dr. Sebastian Steinhorst, Georg Hochmuth, Konrad, Eva and Agnes Martiny.
I would also like to thank Thomas Kontschinsky, Matthias Gutsche, Axel Reinfelder, Andreas von Greißing, Jan Federkeil, Florian Ebenkofler, Andre Hornung, and Thomas Mühlbauer for their valuable input.
For the great collaboration in the last years, my acknowledgments go to Prof. Harry Hoster, Prof. Jürgen Garche, Prof. Tseng King Jet, Ralph Karl, Thomas Heil, Christoph Futter, Patrick Osswald, Alexander Rheinfeld, Jan Geder, Raghavendra Arunachala, Kamyar Makinejad, Lemuel Moraleja and Rudy Tjandra.
Last but not least I would like to highlight the great support by all corporate staff in *TUM CREATE*. Many thanks for that.

This thesis is dedicated to my family who supported me through all my life.

Acknowledgements

ABSTRACT

Lithium ion batteries gain more and more in importance for our everyday life. High energy density, high power and a relatively high voltage level compared to other battery cells makes this type of cells suitable for many applications, especially also in the automotive sector.

The advantage of having a higher voltage level leads however to a higher safety risk. Especially the high flammability of the applied electrolytes is a big disadvantage. To detect and avoid safety relevant failures at an early stage, sophisticated battery management systems are employed. These help to operate batteries within a safe voltage, current and temperature range. Higher temperatures lead not only to faster aging but can lead to serious safety risks. A detailed picture of the temperature distribution is therefore important. Especially in larger scale cells, temperature inhomogeneities can be significant.

The thesis at hand deals with temperature inhomogeneities in lithium ion cells and especially in so-called pouch cells. To face this, different temperature transport mechanisms are introduced. Reasons for and effects from these inhomogeneities are discussed thereafter to motivate the present work.

Various measurable internal cell parameters are researched in terms of their temperature dependency. The resulting knowledge is used to investigate if these parameters are suitable not only for temperature detection but also for estimation of temperature distributions. It is however suggested that these methods do not suffice.

For this reason, various possibilities of temperature sensing, especially in-situ, are discussed. Prototypes are therefore developed and their functionality and integration principles described.

Since pouch cells are available in various sizes and shapes, a measure is defined that makes the comparison of different cells in terms of their temperature distribution possible. Therefore, various measures from literature are compared. A new measure is finally defined based on the Arrhenius equation.

The measure of inhomogeneity is used to investigate measurements from infrared images and from a cell sandwich. This helps to understand the exact distribution and to find suitable spots for sensors under operation.

A final experiment describes results from a fast charging experiment of an automotive battery pack. The measure of inhomogeneity is used to show that large inhomogeneities still exist despite the application of a sophisticated cooling system.

Abstract

ZUSAMMENFASSUNG (GERMAN ABSTRACT)

Lithium-Ionen Batterien spielen eine immer größer werdende Rolle in unserem täglichen Leben. Durch ihre hohe Energiedichte kombiniert mit der Bereitstellung von großen Leistungen und vergleichsweise hohen Spannungen, finden diese Zellen insbesondere im Automobil immer breiteren Einsatz.

Der Vorteil des höheren Spannungs-Niveaus im Vergleich zu anderen Batteriezellen macht Lithium-Ionen Zellen jedoch anfällig gegen Beschädigungen. Insbesondere die leichte Brennbarkeit des Elektrolyts stellt einen großen Nachteil dar. Um sicherheitsrelevante Fehler zu vermeiden, finden deshalb komplexe Battery Management Systeme ihren Einsatz, um die Zellen in einem optimalen Bereich in Bezug auf Spannung, Strom und vor allem auch Temperatur, betreiben zu können. Höhere Temperaturen führen nicht nur zu einer schnelleren Alterung der Zellen sondern können auch ein deutliches Sicherheitsrisiko darstellen. Abgesehen davon können Hot-Spots ein Indikator für innere Beschädigungen in der Zelle sein. Ein detailliertes Bild, nicht nur der durchschnittlichen Temperatur sondern insbesondere der Temperaturverteilung ist deshalb wichtig. Besonders in größeren Zellen treten, auch hervorgerufen durch externe Kühlsysteme, signifikante Temperaturinhomogenitäten auf.

Die vorliegende Arbeit beschäftigt sich mit diesen Temperaturinhomogeneitäten in Lithium-Ionen-Zellen und speziell in sogenannten Pouch-Zellen. Dazu werden zunächst, nachdem grundlegende Wärmetransportmechanismen erklärt werden, Gründe für und Effekte von ungleichmäßigen Temperaturverteilungen erläutert, um das vorlegende Thema zu motivieren.

Es werden dann verschiedenste messbare interne Zellparameter im Hinblick auf ihre Temperaturabhängigkeit untersucht. Eine eingehende Prüfung der Verwendtbarkeit dieser Parameter für die Detektion von Temperaturinhomogenitäten findet anschließend statt. Es wird daraus deutlich, dass keiner der untersuchten Parameter eindeutige Rückschlüsse auf Temperaturverteilung oder die maximale Temperaturdifferenz zulässt.

Deshalb werden daraufhin verschienste Möglichkeiten der Temperaturmessung und insbesondere der in-situ Temperaturüberwachung diskutiert. Verschiedene Protoypen und ihre Integration werden dafür beschrieben.

Da Pouch-Zellen in unterschiedlichsten Größen und Formen verfügbar sind, was Ihre Einsatzmöglichkeiten sehr vielfältig macht, wird ein Maß definiert, welches Temperaturverteilungen quantifiziert und damit zwischen verschiedensten Zellen vergleichbar macht. Dies soll es letztendlich ermöglichen, eine optimale Auswahl an Zellen und an Konfigurationen für die jeweilige Anwendung finden zu können. Um ein geeignetes Maß zu finden, werden Definitionen aus der Literatur untersucht und verglichen. Es wird letztendlich ein eigenes Maß basiert auf der Arrhenius-Gleichung, einem Maß für die Alterung elektrochemischer Systeme, definiert. Das definierte Maß wird dann auf Infrarot- und Zell-Sandwich-Messungen angewannt, und damit die entsprechenden Temperaturverteilungen exakt analysiert. Empfehlungen, wo Sensoren optimal angebracht werden, um Inhomogenitäten zu erfassen, werden darauf basierend entwickelt.

Ein finales Experiment beschreibt Temperaturmessungen an einem automobilen Batterie-Pack während des Schnellladens. Das definierte Maß der Inhomogenität wird darauf angewandt, um zu zeigen, wie, trotz Kühlsystem, erhebliche Ungleichmäßigkeiten in der Temperaturverteilung vorliegen.

Zusammenfassung (German Abstract)

ACRONYMS

ACRONYMS

AC	Alternating Current
Al	Aluminum
Ar	Argon
ARC	Accelerated Rate Calorimetry
ASIC	Application-Specific Integrated Circuit
BMS	Battery Management System
CC	Constant Current
CC-CV	Constant Current - Constant Voltage
CRC	Cyclic Redundancy Check
CSV	Comma Separated Value
Cu	Copper
CV	Constant Voltage
DC	Direct Current
DFN	Dual-Flat No-Leads
DI	De-Ionized Water
DOD	Depth of Discharge
ECM	Equivalent Circuit Model
EIS	Electrochemical Impedance Spectroscopy
EOL	End of Life
HF	Hydrofluoric Acid
HSQ	Hydrogen Silsesquioxane
IC	Integrated Circuit
IR	Infrared
LCO	Lithium Cobalt diOxide
LFP	Lithium Iron Phosphate
Li-ion	Lithium Ion
LTO	lithium-titanate
MAF	Moving Average Filter
MOI	Measure of Inhomogeneity
Ni	Nickel
NMC	Lithium Nickel Manganese Cobalt dioxide
NMP	N-methyl-2-pyrrolidone
OCV	Open Circuit Voltage
PDC	Population Distribution Chart
PI	Polyimide
Pt	Platinum
PTC	Positive Temperature Coefficient
RMS	Root Mean Square
RTD	Resistance Temperature Detector
SEI	Solid Electrolyte Interface
Si	Silicon
SOC	State of Charge, charge capacity in relation to full battery capacity in %

SOD	State of Discharge, SOD = 1-SOC in %
SOH	State of Health
SOS	State of Safety
SPI	Serial Peripheral Interface
UART	Universal Asynchronous Receiver Transmitter
USB	Universal Serial Bus
VDP	Vapor Deposition Polymerization

CONTENTS

LIST OF TABLES

LIST OF FIGURES

1

INTRODUCTION

Lithium Ion (Li-ion) batteries are utilized increasingly in everyday applications from mobile devices over power tools up to electric cars. Compared with other chemistries, the success of Li-ion batteries has its foundation in the combined high energy and power density as well as high voltage, enhanced lifetime, and the absence of severe memory effects. The relatively high voltage level demands however for organic electrolytes. These provide a meta-stability by forming protective layers on the surface of the electrodes. Damages to these layers combined with a comparably high level of flammability of the applied electrolyte though inevitably result in safety hazards.

To ensure the operation within their predefined bounds in terms of voltage, current and temperature, Li-ion batteries require sophisticated Battery Management System (BMS). With a well-designed and precise BMS, lifetime of batteries is optimized while safety risks are minimized. As a result, the demand for safe and long-lasting operation strategies is satisfied [97].

One crucial factor when dealing with Li-ion batteries is the temperature. Sub-zero temperatures lead to an increased lithium plating and therewith an enhanced capacity loss as well as the likelihood of dendrites that eventually result in internal short circuits[112]. Higher overall temperatures in the cell mainly lead to an accelerated aging, resulting from a loss of capacity and a rise in internal resistance. On the other hand, an internal cell temperature exceeding the designated range during cycling may be an early indicator for safety-relevant failures and can finally cause self-heating in the cell, which is referred to as the thermal runaway.

With the emerging trend of increasing cell sizes, particularly in automotive applications, considerable safety risk are arising. Additionally, larger inhomogeneities within the temperature distribution have to be faced. The reasons and consequences thereof are widely discussed in the thesis at hand.

Arunachala presents in [6] simulation results of cells with different sizes and cooling strategies. It is shown that temperature gradients can reach above 10 K in large-scale automotive cells. To find optimal operating conditions and to detect early failures, permanent, space resolved and reliable temperature monitoring is therefore inevitable.

In most of today's applications the monitoring is performed by attaching sensors to the surface of the cells (cf. [68]). However, active cooling systems are frequently used in larger scale applications which are cooling the battery from its surface. The resulting difference in time response between a cell's surface and its interior may result in an inappropriate battery management when only the surface temperature is monitored. Therefore, an in-situ temperature monitoring as it is described by [76], [59] and [56] is advantageous.

Furthermore, reactions in the worst case situation of a thermal runaway can happen fast and may not be detectable on the cell's surface within a timescale that allows to shut off the cell before serious damage to the surroundings occurs. Feng et al. show in [29] a sensor placed in a 25 Ah prismatic hard case cell which is formed of two pouch cells. It showed considerably large temperature gradients between the cell's center and the cell's surface (> 500 K) during a thermal runaway test.

Previous research activities presented by [88] showed that tracking the in-cell temperature is mainly beneficial during abuse scenarios and that a space resolved temperature monitoring is

crucial in order to detect critical hot spots and undesired temperature gradients. Suitable methods for temperature detection in the cell based on internal parameters as well as on sensor data need therefore to be investigated while working with the challenging cell environment.

In this thesis, the focus lies mainly on temperature inhomogeneity in pouch cells. This type of cell offers a higher energy density and flexibility in shape and design compared to hard-case cells. For the postulated automotive applications these cells provide therewith a good solution. This flexibility makes the comparison of different cells however challenging especially when it comes to inhomogeneity. It demands therefore for a scalable, size- and shape-independent measure of inhomogeneity. The scalability of this measure has to be ensured to reduce the required amount of sensing points to a minimum.

1.1 OVERVIEW

The remainder of this thesis is organized as follows: In Chapter 2 a short introduction is given into what Li-ion pouch cells are and how they are distinguished from other lithium-based cells. A description of temperature sensing types and heat transfer mechanisms that are relevant for this thesis is following thereafter. The chapter is concluded by motivating the topic of temperature inhomogeneities with different important aspects. An investigation of temperature depending internal cell parameters is provided in Chapter 3. The parameters are quantified in conjunction with measurements in order to identify the suitability of these measures for temperature inhomogeneity detection. The method of detecting temperature differences with the help of sensors is discussed in Chapter 4. Different sensing mechanisms and data transmission technologies are therefore introduced and prototypes developed to find the best possible solution. Since different cells need to be compared during different applications to find optimal operation strategies, a measure of inhomogeneity is defined in Chapter 5. A literature study shows various methods from other disciplines that provide this possibility followed by an own definition for a temperature inhomogeneity measure in Li-ion cells. Measurements from an infrared camera as well as data from within a cell sandwich, meaning two cells stacked onto each other, are described in Chapter 6 and further evaluated in Chapter 7. The thesis is finally concluded in Chapter 8.

1.2 PUBLICATIONS AND UNDERLYING THESES

Parts of this thesis have been presented and published in [66–72, 87]. In [69, 71, 87] different approaches for temperature sensor development, their integration and evaluation into Li-ion pouch cells are provided. In contrast, [70, 72] deal with the development of data transmission through the cell casing in an analog and digital setup respectively. Supporting to the work of this dissertation are the following student theses: [23, 52, 75, 86].

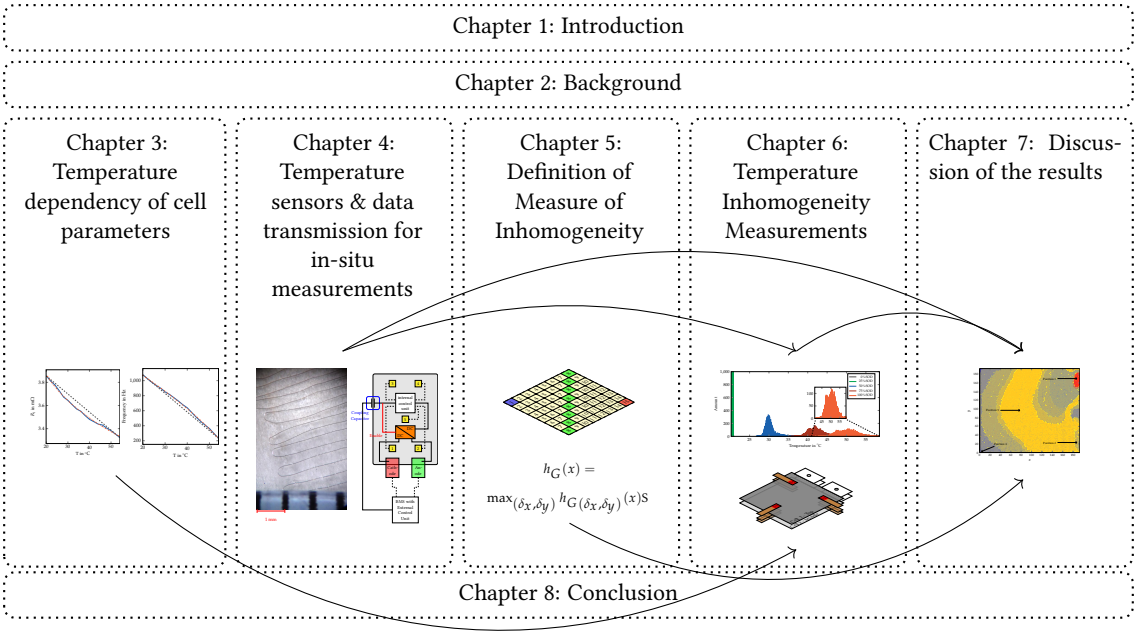

Figure 1: Interconnection of Chapters within this Thesis

2

BACKGROUND

To understand the underlying requirements and mechanisms of the topic, this chapter describes the basic structure of a Li-ion pouch cell. Li-ion cells are available in many shapes and with many different chemistries. This thesis focuses however on temperature inhomogeneities in Li-ion pouch cells. While most described phenomena might be applicable to other configurations like cylindrical or prismatic hard case cells as well, pouch cells are chosen to narrow the scope. This type of cells is applied in the electric taxi *EVA* which has been developed in *TUM CREATE*.

Heat transfer mechanisms are introduced in the following as well and from that reasons for temperature inhomogeneities are derived. The chapter is concluded by discussing the effects of temperature inhomogeneities on the battery cells.

2.1 LITHIUM ION POUCH CELL

Similar to other battery cells, a pouch cell consists of multiple layers of electrode pairs, stacked on each other and separated by a polyolefin-based separator, or - in latest cell developments - ceramic separator or ionic conductive polymer. The separator, on the one hand, has the task of preventing electrodes from electric short circuits while providing an optimal ionic flow from one electrode to another. On the other hand, especially polymer based separators also provide a safety-shut down option. If the cell temperature exceeds roughly 120 °C, the polymer starts deforming and therewith stops the ionic flow to prevent electrochemical processes that lead to a self-heating of the cell.

The cell stack is soaked in a liquid or jelly-like non-aqueous electrolyte mostly on base of $LiPF_6$-salts solved in organic solvents. This type of electrolytic solution is used due to the high voltage level, that lithium-based battery cells offer. Aqueous electrolytic solutions would dissolve under the present potential. The applied organic solvents however bear a higher safety risk thanks to their high flammability.

The cathodes usually consist of an aluminum current collector with a chemical compound with lithium (e.g. Lithium Nickel Manganese Cobalt dioxide (NMC) or Lithium Iron Phosphate (LFP)) as active material, coated on both sides of the current collector. The anodes in contrast are composed of a copper current collector coated with mostly graphite, that can store lithium.

What distinguishes pouch cells from other cell shapes is a soft casing, made of aluminum laminate, where the electrode stack is sealed in under vacuum. Nickel tabs for the anode and aluminum tabs for the cathode are fed through the sealing as cell terminals. The light, soft casing leads to a higher energy density compared to other cell casings. Typical dimensions for the layers of such a cell and a schematic setup for a single layer of electrodes can be seen in Fig. 2 as they are mentioned by Maleki et al.[65]. Note that the cell described by Maleki is a commercial cell and has therefore double coated electrodes, while the here drafted setup shows the active material only on one side of the current collector. The thicknesses of the layers have been adjusted accordingly and are taken from a 63 Ah pouch cell from *Kokam* as it is used in the electric vehicle project *EVA* from *TUM CREATE*. In Fig. 3 the structure of the soft aluminum-laminate casing of a pouch cell is exemplary shown. Fig. 4 shows a pouch cell with the coordinate system that will be applied in the whole thesis.

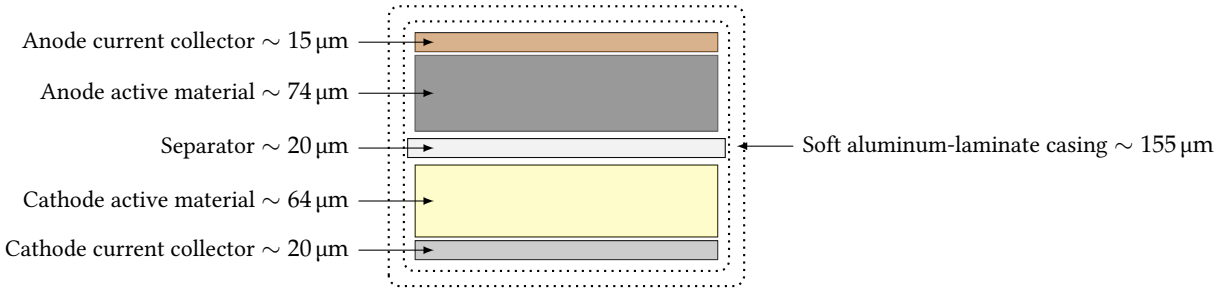

Figure 2: Setup of one electrode stack of a Li-ion pouch cell with thicknesses for each layer according to measurements on a 63 Ah pouch cell from *Kokam*.

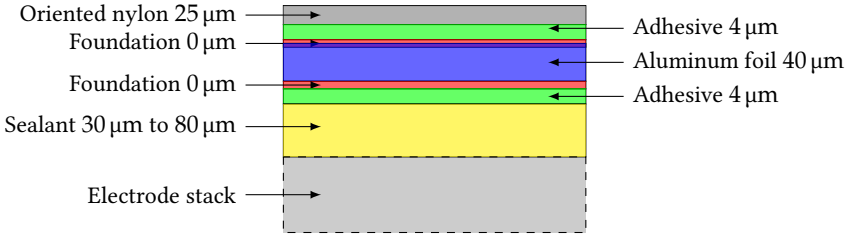

Figure 3: Set up of the soft aluminum-laminate casing according to [101] as an example. The set up was chosen such that it fits the dimensions of the cell displayed in Fig. 2.

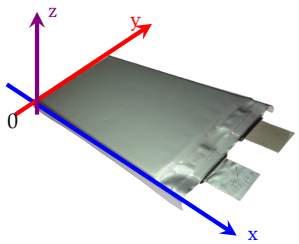

Figure 4: Pouch cell with the coordinate system, as it is used in the whole thesis.

2.2 TEMPERATURE SENSING

Temperature sensing possibilities are manifold: touching and non-touching, thermo-resistive, thermoelectric, with the help of semi-conductors with acoustic or optical principles and many more[31]. In the following a selection of sensing principles is described according to the methods used in this thesis. For a full list of methods refer to [31, 32] and others in literature.

2.2.1 *Resistance Temperature Detectors*

The term Resistance Temperature Detector (RTD) is usually used to describe metal sensors. The fact that the resistance of all metals is changing over temperature is utilized here. Although in principle all metals can be used for this purpose, the most commonly used metal is platinum due to its "predictable response, long-term stability, and durability" [31, p.462]. RTDs are available either in wire-based or in thin-film technology.

All RTDs have in common that they are absolute sensors. This means that once they are calibrated an absolute temperature can be measured without the need of reference points.

The temperature dependency of metals is generally approximated with a fourth-order polynomial function for values between $-200\,^{\circ}\mathrm{C}$ to $0\,^{\circ}\mathrm{C}$ and with a second-order polynomial function for temperatures between $0\,^{\circ}\mathrm{C}$ to $630\,^{\circ}\mathrm{C}$ [31, p.463] as written in (1). R_Θ represents thereby the resistance at a specific temperature Θ and R_0 the resistance at $0\,^{\circ}\mathrm{C}$. A, B and C are material dependent constants.

$$\begin{aligned} R_\Theta &= R_0[1 + A\Theta + B\Theta^2 + C\Theta^3(\Theta - 100)], && \text{for } \Theta = -200\,^{\circ}\mathrm{C} \text{ to } 0\,^{\circ}\mathrm{C} \\ R_\Theta &= R_0[1 + A\Theta + B\Theta^2], && \text{for } \Theta = 0\,^{\circ}\mathrm{C} \text{ to } 630\,^{\circ}\mathrm{C} \end{aligned} \tag{1}$$

A rather linear behavior between $0\,^{\circ}\mathrm{C}$ to $100\,^{\circ}\mathrm{C}$ according to (2) [31, p. 63] makes especially platinum RTDs easy to use in the range, where they are also operated in battery applications. Platinum is additionally widely known to be resistant in many acids including Hydrofluoric Acid (HF), which also makes a promising candidate as discussed further in Chapter 5.

$$R_\Theta = R_0(1 + \alpha(\Theta - \Theta_0)) \tag{2}$$

SUITABILITY FOR BATTERY APPLICATIONS: RTDs are thanks to the aforementioned linearity in the required temperature range and the suspected stability in electrolyte suitable for both, in-cell and on-cell temperature measurements for Li-ion cells. The potential to manufacture this type of sensor in various shapes and especially also in a thin-film process makes them additionally relevant. If the sensors are built on a flexible substrate, they can easily be integrated either between electrode stacks or on the surface of a cell by ideally using thermal conduction without bigger losses. The fact that this type of sensors measures absolute temperatures and therefore doesn't require temperature compensation but only initial calibration makes it possible to build them in even smaller sizes.

2.2.2 *Thermocouples*

Thermocouples are thermoelectric contact sensors. The principle is to connect two different metals at the so called hot junction, which corresponds to the sensing point, and measure the variation of the thermoelectric potential between both materials over the temperature on the cold junction (cf. Fig. 5). It is required to hold the contacts, where the potential is measured either at a defined constant reference temperature or to measure the temperature at this place with a reference sensor. The reason is that thermocouples are only able to detect potential changes and therewith relative temperature differences with this principle.

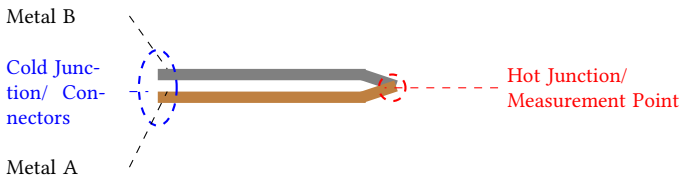

Figure 5: Setup of a thermocouple temperature sensor

Depending on the used metals, different temperature ranges can be covered. The dependence of the voltage difference dV on the temperature difference dT is given by [32, pp.88-89] according to (3). $\alpha_{AB} = \alpha_A - \alpha_B$ is thereby the differential Seebeck coefficient of metal A and B, calculated from the unique parameter α_x for each material.

$$dV_{AB} = \alpha_{AB} dT \tag{3}$$

The selection of metals applied in thermocouples should be performed such that a highest possible resolution can be achieved. This is the case, if the differential Seebeck coefficient α_{AB} is as high as possible in the required temperature range. [99] provides a table for the Seebeck coefficient of commonly used metals. The thermoelectric potential is given for room temperature in reference to platinum. While semiconductors show, depending on their doping, a much higher thermoelectric potential, for investigations on self-made thermocouples, only metal pairs are considered here since their processibility is considered to be easier. Copper and Nickel build a sufficiently high differential Seebeck coefficient of $22.5\,\mu V\,K^{-1}$. They are especially of interest, since both metals are used as current collectors in Li-ion batteries and considered to provide stability in the used chemical environment.

Table 2: Seebeck coefficients of selected metals vs. platinum [98, p.552-553].

Material	Seebeck Coefficient in $\mu V\,K^{-1}$
Copper	7.5
Silver	7.3
Gold	7.0
Lead	4.4
Aluminum	3.9
Carbon	3.0
Graphite	2.2
Platinum	0
Sodium	-2.0
Nickel	-15
Cobalt	-17
Constantan	-65

Off-the-shelf thermocouples are mainly wire-based. Often alloys are applied there as one partner of the thermocouple like NiCr, PtRh or Constantan since they provide a higher durability and stability over a wide temperature range. If thin-film technology is used, the voltage response to temperature changes is usually smaller according to [18] and [111].

$$S_F = S_B \left[1 - \frac{3}{8}\left(\frac{\lambda}{t}\right)(1-p)\frac{U}{1+U}\right] \tag{4}$$

In equation (4)[18], S_F and $S_B = \alpha_{AB}$ are the Seebeck coefficients of the thin-film and of the bulk material respectively, p is the scattering coefficient of the film surface, t the thickness of the film and λ the electron mean free path. The mean free path is the distance that one particle travels in average between two collisions with other particles[98, p.707]. According to the Bloch quantum theory of electrical conduction in metals, it can be assumed that $U = \left(\frac{\partial \ln \lambda}{\partial \ln E}\right)_{E=\zeta} = 2$, with E as the energy function and the fermi energy ζ . The scattering coefficient can be assumed to be $p = 0$ [18, p.420]. With these assumptions (4) can be simplified to (5).

$$S_F = S_B \left[1 - \frac{1}{4}\left(\frac{\lambda}{t}\right)\right] \tag{5}$$

The electron mean free path λ is approximated with equation (6) for solids by [103, p.578].

$$\lambda = \frac{1}{n_V \pi d^2} \tag{6}$$

with n_V as the number density of molecules and d as the distance between two molecules. The distance depends on the measuring method. Therefore, the values given by [98, pp.552-553] and used for the calculation of the thin-film Seebeck coefficient are only estimated reference values. The ion radius is taken for the fully charged state. n_V can be calculated according to equation (7) with the mass density ρ_m, Avogadro's number N_A and the molar mass M[103, p.842]. In [33], the mean free paths for various metals are disclosed. According to this publication $\lambda_{Cu} = 39.9\,\text{nm}$ and $\lambda_{Ni} = 5.87\,\text{nm}$. Fig. 6 shows the ratio of S_F/S_B, the thinfilm vs. the bulk Seebeck coefficient over the thickness of the film. It shows especially for copper that for thicknesses above 100 nm the thinfilm coefficient does hardly differ from the bulk coefficient. The ratio of S_F/S_B at 100 nm is 0.985 for Ni and 0.900 for Cu. In the range of 25 µm, this ratio rises to 1 for both materials. If sputtering is used as a method for deposing the thin-film metals on a substrate, the thicknesses are usually above 100 nm. For that reason the thin-film effect is negligibly small. The thin-film effects are further highlighted in Section 4.6 for self-made thermocouples.

$$n_V = \frac{\rho_m * N_A}{M} \tag{7}$$

SUITABILITY FOR BATTERY APPLICATIONS: Similar to the RTD sensors, also thermocouples provide a great suitability for battery applications thanks to their wide temperature range with a predictable and stable temperature dependency, flexibility in the production process and, depending on the used materials, stability in electrolyte. They can be like RTDs built on a thinfilm substrate and therefore provide equivalently good thermal conduction between the heat source and the sensing point. One disadvantage of this sensor type however is the requirement for applying a reference sensor, since only relative temperature differences between the sensing point and the cold junction can be detected.

2.2.3 *Integrated Circuit Sensors*

Many ICs provide integrated temperature sensing. The sensing principle uses the P-N junction of semiconductor diodes or transistors, as exemplified in Fig. 7 for a forward-biased semiconductor junction. When a constant current is applied to this junction, the respective voltage shows a linear dependency on the temperature. This relation is presented in Eq. (8). In this equation "E_g is the energy band gap of silicon at 0 K [...], q is the charge of an electron, and K is a temperature-independent constant"[32, p.489]. This constant can be determined based on (9), where b is the linear slope when a constant current flows over the junction. According to [32, p.489], "typically,

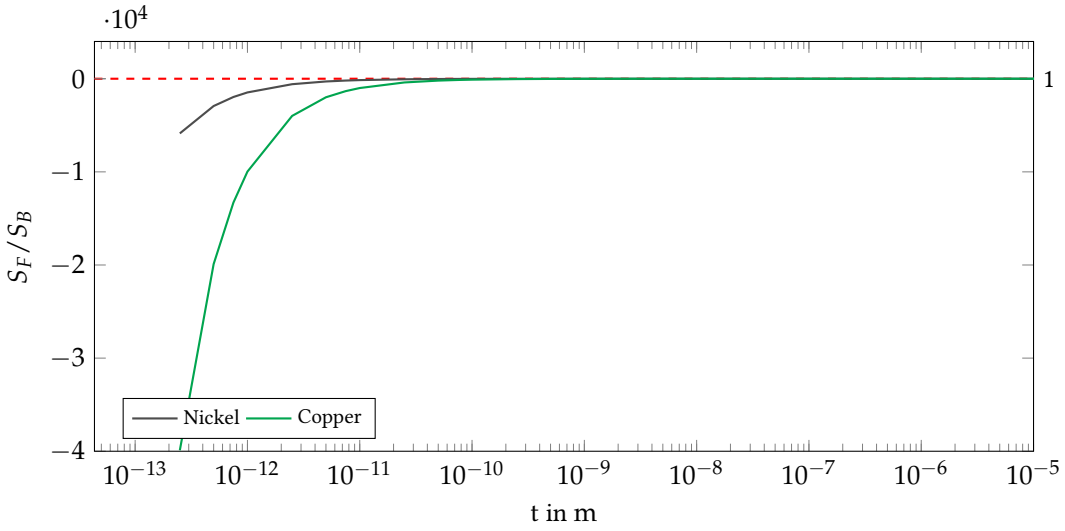

Figure 6: Thinfilm Seebeck coefficient S_F vs. bulk coefficient S_B over the film thickness t for Nickel and Copper.

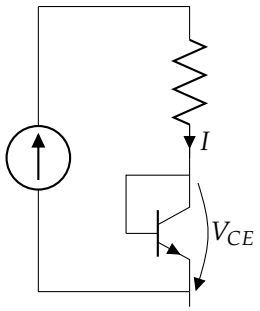

Figure 7: Forward-biased p-n junction temperature sensor with a diode-connected transistor according to [32, p.488] as it is used in ICs.

for a silicon junction operating at 10 µA, the slope (sensitivity) is approximately $-2.3\,\mathrm{mV\,°C^{-1}}$ and it drops to about $-2.0\,\mathrm{mV\,°C^{-1}}$ for a 1 mA current."

$$V_{CE} = \frac{E_g}{q} - \frac{2kT}{q}(\log K - \log I) \tag{8}$$

$$b = \frac{dV}{dT} - \frac{2k}{q}(\log K - \log I) \tag{9}$$

The advantage of this sensor type is that, thanks to the integrated design, it can be built with high precision, very small sizes and inexpensively. Additionally, the digital data provided by these sensors are less prone to errors and can be easily verified with respective transmission protocols. In Section 4.9.2 sensors of this type are further addressed.

SUITABILITY FOR BATTERY APPLICATIONS: Integrated circuit sensors can be built inexpensively in very small sizes. By providing digital temperature data, they can be used for both wire-based and wireless data transmission solutions. An integration into sensor networks is therewith easily realizable. The ICs can be encapsulated into an electrolyte-resistant coating without a sus-

pected loss in functionality. Additionally, absolute temperatures can be measured and re-calibration can be performed without the necessity to dismount the sensor from its environment. Compared to thermocouples or RTDs the production process requires a bigger effort. Nevertheless, the major properties make this type of sensor suitable for both in-cell and on-cell measurement.

2.2.4 *Infrared sensing*

An infrared temperature sensor, other than the sensors described above, is a non-contact sensor. It measures in fact not the actual temperature but the heat that radiates from an object. A big advantage of this type of sensor is that areas and not only single points can be monitored. According to [32, p.426], their "operating principle is based on a sequential conversion of thermal radiation into heat and, then, conversion of heat level or heat flow into an electrical signal by employing conventional methods of heat detection." Similar to the thermocouples, an infrared detector needs a reference temperature sensor that measures the initial temperature in comparison to the measured temperature. Aside from the actual infrared detector, several other rather bulky and expensive components are necessary for the temperature measurement. This is for instance a supporting structure to hold the sensors, a housing and a protective window that filters an undesirable portion of the spectrum. For this reason, infrared sensors are mainly used for laboratory applications.

For the detection of thermal radiation with a sensor, the Stefan-Boltzmann law as written in (10) is the underlying approximation when the spectrum of wavelength embraces more than 50 % of the total radiated power, which can be assumed for infrared sensors. In this equation A is the geometry factor, ε the emissivity which is assumed to be wavelength independent and σ is the Stefan-Boltzmann constant.

$$\Phi_b = A\varepsilon\sigma T^4 \tag{10}$$

This equation, however, is assuming the radiation from an object into an "infinitely cold space (at absolute zero)" [32, pp.103-104]. For infrared detectors, the net flux which is the radiation from the sensor towards the object needs also to be taken into account. (11) shows this correlation with the sensor's radiation Φ_s, emissivity ε_s and temperature T_s respectively.

$$\Phi = \Phi_b + \Phi_s = A\varepsilon\varepsilon_s\sigma(T^4 - T_s^4) \tag{11}$$

The wavelengths for infrared radiation are in the range of 780 nm to 1 mm, while the visible light operates between 380 nm and 780 nm. This means that if a sensor covers the whole infrared spectrum, the likelihood for sensibility to visible light is high at transition wavelengths. For this reason, researched surfaces have to be non-reflective. An aluminum-laminate surface as lithium-ion pouch cells offer it has therefore to be covered with a non-reflective coating like a matt spray.

SUITABILITY FOR BATTERY APPLICATIONS: As mentioned above, infrared temperature sensors demand bulky and rather expensive components together with a reference temperature sensor to measure temperatures. For this reason, they are not suitable for applications under real operation, especially when researched cells are assembled in a battery pack. In contrast to the before mentioned sensors they however provide space-resolved temperature data even from larger surfaces. Compared to the previously described sensor technologies, the IR technology offers contactless sensing since only thermal radiation contributes to the measurement. This means that the temperature monitoring does not influence the temperature of the researched object and therefore provides undistorted data. For laboratory applications and to receive qualitative information about space-resolved temperature distributions, IR sensors represent an excellent solution.

2.3 HEAT TRANSFER

Heat transfer happens in three different ways: heat conduction, convection and radiation [61]. At the surface of a body, all three phenomena are combined. A definition of all three in the steady state is given in the following.

Thermal convection only exists in moving media while it is absent in solids[99]. This means for batteries that heat convection only takes place at the surface. The emitted heat ΔQ is depending on the heat transfer coefficient α, the contact area A between the solid and the surrounding liquid, the temperatures of both media (T for the solid and T_L for the liquid) and the time interval Δt. The resulting heat flow is defined in Eq. (12)[98]. For passive cooling systems natural convection takes place, while if active cooling systems are applied the effect gets intensified.

$$\Phi_{conv} = \Delta Q / \Delta t = \alpha \cdot A \cdot (T - T_L) \tag{12}$$

Thermal radiation in contrast is a phenomenon that concerns all bodies. It is the process of emitting energy through electromagnetic radiation. "The intensity of such energy flux depends upon the temperature of the body and the nature of its surface"[61]. Stefan Boltzmann's law builds therefore the correlation between the radiated heat energy of an area A with the temperature T per unit of time and the temperature [99]. The total radiant flux is therewith defined according to (10) with the Stefan-Boltzmann constant $\sigma = 5.670\,400\,1 \times 10^{-8}\,\mathrm{W/(m^2K^4)}$ and the material dependent emissivity ϵ [61, 99] which is $\epsilon = 1$ for black bodies and $\epsilon = 0.86$ for a laminated pouch cell, according to measurements performed at the University of Waterloo [73].

Heat conduction is present within one body as well as on the surface. The heat flow through a homogeneous medium in the steady state is defined according to (13) with the material dependent coefficient of thermal conductivity λ, the contact area A, the thickness of the medium s through which the heat flows and the temperature difference between one side of the medium and the other ΔT[99].

$$\Phi_{cond} = \lambda \cdot \frac{A}{s} \cdot \Delta T \tag{13}$$

If n different objects are placed in series to each other, as it is the case in an electrode stack of a pouch cell, the total heat flow can be calculated according to (14)[99]. ΔT is again the temperature difference between each side of the stack, while R_i is the heat resistance of each single object or layer.

$$\begin{aligned} \Phi_{cond,stack} &= \frac{\Delta T}{\sum_{i=1}^{n} R_i} \\ R_i &= \frac{s_i}{\lambda_i A_i} \end{aligned} \tag{14}$$

The conducted heat, as defined in (15) with the time difference dt, results thereof.

$$dQ = \Phi_{cond} \cdot dt \tag{15}$$

In real systems heat transfer is normally a combination of heat conduction with or without convection and thermal radiation. Sometimes specific mechanisms can be negligible[80]. In case of a pouch cell, the heat is transported by conduction from one electrode to another and to the surrounding by free convection and thermal radiation.

In the non-steady state, where the warming process of the material is considered, and hence the temperature T and the time difference dt is not constant, above equations are not applicable. In this case the heat equation is used with the thermal diffusivity α. (16) shows the one-dimensional heat equation. This equation is obtained by combining Fourier's law with the first law of thermodynamics[61]. α is a measure that shows how quickly a temperature difference is equal-

ized in a medium [61, 99]. It depends on the above mentioned thermal conductivity λ, the material specific density ρ and heat capacity c. The universal equation for multidimensional problems is given in (17) with the Laplace operator Δ.

$$\begin{aligned} \frac{\partial^2 T}{\partial s^2} &= \frac{1}{\alpha}\frac{\partial T}{\partial t} \\ \alpha &= \frac{\lambda}{\rho c} \end{aligned} \tag{16}$$

$$\nabla^2 T = \Delta T = \frac{1}{\alpha}\frac{\partial T}{\partial t} \tag{17}$$

Solutions for this equation can be found with standard methods for solving partial differential equations, like the separation of variables, as for instance described in [61]. Specific boundary conditions help to find the necessary constants.

2.4 REASON FOR TEMPERATURE INHOMOGENEITY

When looking at the above stated heat equations, it is obvious that the heat transfer in a medium is depending on time and location. Accordingly, also the Measure of Inhomogeneity (MOI), which is closer discussed in Chapter 5 and a measure for quantifying the temperature inhomogeneity in battery cells, depends on these variables $MOI = f(A, s, t)$. In the following a closer look is taken into externally and internally triggered reasons for temperature inhomogeneity.

2.4.1 *External causes*

To understand external causes for a temperature inhomogeneity in Li-ion cells and from that to derive the demand for an appropriate temperature monitoring, two major applications and their recent developments need to be considered: automotive and mobile applications.

In **automotive applications** large scale cells of more than 50 Ah are often used to increase the overall energy density of the battery pack and to reduce the assembling effort. The demand for fast charging, energy recuperation and the normal drive cycle lead to sometimes high peak currents and therewith an increase in the internal temperature. Higher temperatures however decrease the lifetime of a cell significantly. According to measurements and simulations from Deshpande et al. [20] a cell operated at 60 °C reaches only one quarter of the cyclic lifetime of a cell operated at 15 °C. Sources like [14] and [49] mention a calendar life degradation of lithium ion batteries that follows the Arrhenius law as further highlighted in Section 2.5. This correlation shows that capacity degradation during calendaric aging increases by roughly a factor of 2 with a temperature increase of only 10 K. Depending on the chemistry of the cell this factor can vary a little bit, but the tendency of lifetime degradation with increased temperature is alike. Additional serious safety risks through high temperatures make active cooling systems crucial. While **cooling systems** help to decrease the overall temperature of a cell, as a drawback the temperature inhomogeneity increases, depending on the type of the applied cooling system. In battery systems today the cooling is done by completely or partially cooling the surface of a cell or cell stack. This leads to inhomogeneities since the heat arises volumetrically in the cell and the inner layers experience therewith higher temperatures than the cooled surface. In [68] different cooling strategies have been simulated and the temperature inhomogeneity has been depicted. Gerschler investigates this topic via space-resolved simulation in [38] for single cells and different cooling strategies. In his comparison of natural convection and active cooling at the cell casing he outlines an overall temperature decrease for the active cooling system. However, depending on the temperature of the coolant, temperature inhomogeneities rise by a factor of up to 4.5. With this temperature inhomogeneity also differences

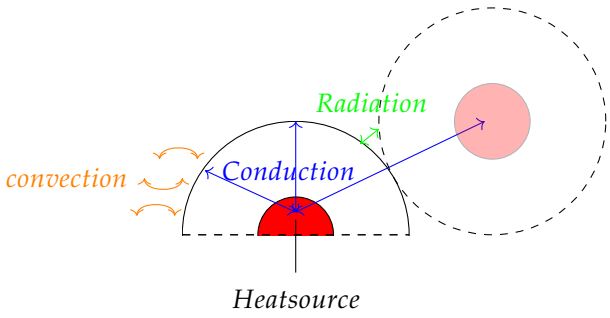

Figure 8: Heat transfers depicted on an example of two adjacent cylindric cells in a pack configuration.

in the space-resolved Depth of Discharge (DOD) of up to 18.34 % arise for active cooling, compared to less than 2 % for natural convection.

For **mobile applications** like smart phones and tablets the recent development has been, to make devices lighter and thinner while increasing the display size. Through the added features the energy demand increased significantly in the last years and the capacity of the used cells also increased. These developments result in a dense packaging, making temperature hot spots on the cell unavoidable as ICs like the microcontroller or the GPS module produce local heat.

Another cause for temperature inhomogeneity in a cell can be of **mechanical origin**. This concerns especially pouch cells that through their soft casing are more prone to mechanical stress and damage than hard case cells. Spotnitz mentions in [95] that during abusive tests, like nail penetration and crush, but also when the cell is short-circuited, rapid localized heating takes place which leads to high temperatures that activate further chemical reactions in the cell, i.e. the so called thermal runaway. Cannarella shows in [17] that also local stress leads to damages in a cell which causes locally high electrochemical activity and can lead to lithium plating or, presumably, to increased local temperatures.

2.4.2 *Internal causes*

Internal causes for temperature inhomogeneity in Li-ion cells are manifold. The most severe cases are discussed in the following.

The **cell shape and structure** is probably one of the most obvious causes for temperature inhomogeneities. In [47] it is shown that aside from the size of a cell, also the shape has a big influence on the internal temperature. This is caused by the fact that heat is caused by the voltage drop in the cells. Different cell designs lead therewith to an inhomogeneous current distribution and, caused by that, inhomogeneous heat development. Another influence is the heat dissipation in a cell or in a pack. While from the core of the cell towards the outside, only thermal conduction takes place, the outside is exposed to convection and radiation to the surrounding. More heat is dissipated faster on the surface than in the core, which, depending on the shape of the cell, leads to larger or smaller inhomogeneities. In Fig. 8 the **heat transfer** in two adjacent cells is exemplary displayed. Through the fact that some cells or parts of a cell are subjected to radiation and convection, while other parts are only subjected to either conduction or convection, the heat is not dissipated homogeneously in a cell. This is obviously influenced by both external causes as mentioned above like the type of application, the pack set-up structure or the cooling system, but also by internal causes, like the shape of a cell or the power of the heat source which leads back to the type of cycling.

The temperature distribution for differently shaped prismatic cells, all with a capacity of 9 Ah have been investigated through simulation at the end of a 1 C discharge. Not only the temperature

gradient, but also the average temperature decreases with a higher area-to-thickness ratio. [106] also mentions that "the cell design has a significant influence on temperatures and temperature gradients inside cells". This concerns not only the cell shape, but also factors like the electrode thickness or the electrode configuration, as shown by Kim in [50]. Kim shows through measurements and simulation of three 10 Ah pouch cells with different electrode configurations that are discharged at 5 C that depending on the configuration, temperature gradients can vary between 11 K and 17 K at the same State of Discharge (SOD).

Another effect that influences the temperature inhomogeneity is the **cycling** rate and phase. In [106] it is shown that "the temperatures [...] rise continuously during discharge with a constant C-rate". IR data from discharge tests done for this thesis with a 40 Ah pouch cell, that are discussed in detail in Section 6.1, show the development in the temperature distribution over different charge rates and at different SODs. These measurements present a clear increase in inhomogeneity when higher C-rates are applied.

2.4.3 *Production*

The **production process** can be a source for internal damage and hot spots in the cell. The probably most prominent case is the battery fire on board a *Boeing 787* airplane in January 2013. Reports provided by the American *National Transportation Safety Board* [45] and *All Nippon Airways*[1] showed that internal damages or impurities from the production process lead to an internal short circuit in one of the battery cells which finally caused a thermal runaway.

2.5 EFFECTS OF TEMPERATURE INHOMOGENEITY ON THE CELL

Similar to the reasons for temperature inhomogeneity in a cell, the effects that gradients and hot spots have on a cell, can be numerous.

Fleckenstein describes and quantifies in [30] **current density** and **local State of Charge (SOC)** differences that are caused by temperature gradients in Li-ion cells. The paper displays simulation and measurements results that have been approximated for cylindrical cells by investigating three parallel cells: fully isolated, semi-isolated and non-isolated. By this method, a larger cell with the triple capacity of one single cell and an inhomogeneous temperature distribution is simulated. The temperature of each cell is measured with a thermocouple. The measurements have been performed in a climate chamber and the cells have been stressed with 5 C and 8 C pulses. Temperature differences between each of the three cells of up to 20 K could therewith be provoked. Through an increased temperature in the fully isolated cell compared to the other cells during the cycling process, the fraction of current flowing through this fully isolated cell in the last cycle raised to 38 % instead of 33 %, which would be expected in three equal cells. The SOC at this stage is significantly lower by 5.3 % for the isolated cell than for the non-isolated cell. Even after a long resting period, the SOCs did not fully compensate between the cells. Fleckenstein mentions that aside from the local temperature differences that contribute according to the Arrhenius equation, which is discussed in more detail below, exponentially to the **aging** of a cell, also local current and SOC differences contribute further towards a faster degradation. Fleckenstein concludes that "In summary, deduced from literature the three observed inhomogeneities (temperature, current density and SoC) can, in common, lead to a more than linearly accelerated aging progress for the warmer inner regions inside a Li-ion cell compared to the colder outer regions. In consequence, a different and faster aging behavior of the entire cell is expected than for a cell with - hypothetically - absolutely uniform temperature distribution with the same volume averaged temperature."[30]

Gerschler investigates in [37] into different cooling strategies for pouch cells and their effect on the State of Health (SOH) distribution in the cells. It is obvious from the results that the induced current distribution is proportional to the temperature distribution. While at the End of Life

(EOL) of the researched cells, the average temperature as well as the temperature gradient increase compared to a new cell, the current gradient decreases. The SOH spread in contrast increases, according to Gerschler, continuously over the lifetime and is proportional to the temperature rise. As already suggested by Fleckenstein [30], the rate of degradation of the cell increases exponentially with temperature and voltage according to the Arrhenius equation and the Butler-Volmer equation. For a better understanding of these equations, both are introduced and discussed in detail in the following.

The Arrhenius Equation shows the dependence of the reaction rate k on the absolute temperature T in K, the activation energy E_a in J/mol, the pre-exponential factor k_0 in s^{-1}, and the gas constant $R = 8.3144\,J/mol \cdot K$ [9]. With these parameters the equation is defined according to (18). The activation energy E_a is depending on various influences like cell chemistry, SOC, temperature, cycling rate and age of a cell. For calendar aging at 50 % SOC of NMC cells, [25] derived values between $[47.97, 50.71]\,kJ\,mol^{-1}$ depending on storage time of the cells from aging tests. [60] achieves values in a similar range from tests with $Li_xNi_{0.8}Co_{0.15}Al_{0.05}O_2$ based cells for the initial stage of aging. Therefore, as an approximation, $E_a = 50\,kJ\,mol^{-1}$ is assumed in the following.

$$k = k_0 \cdot e^{-\frac{E_a}{R \cdot T}} \tag{18}$$

Yang [108] uses this equation to model the SOH of NiMH cells in a battery pack. He therefore divides the rate of cell capacity change $k = dC$ through the aging cycle dn and obtains therefrom (19) with the system-dependent factors $\Lambda = k_0/dn$ and $\lambda = E_a/R$.

$$\frac{dC}{dn} = \Lambda e^{-\frac{\lambda}{T}} \tag{19}$$

To investigate the lifetime deviation of temperature T_2 in comparison to T_1, where $T_2 > T_1$, both sides of (19) are integrated over the cell's lifespan and the two different temperatures are introduced. This leads finally to (20) with C_r being the capacitive reduction threshold defining the EOL (usually 20 %) and the cycle life deviation Δn_c. This equation shows the dependence of temperature gradients on the life time of a cell. With increasing temperature gradients, the lifetime of the cell will decrease faster.

$$\Delta n_c = \frac{C_r}{\Lambda}\left(e^{\frac{\lambda}{T_2}} - e^{\frac{\lambda}{T_1}}\right) \tag{20}$$

Belt shows in [10], among other dependencies, the temperature induced relative capacity fade over the time, based on the Arrhenius equation for temperatures up to 50 °C. The therein defined relation is given in (21) with the time t, a fixed reference temperature T_0 and the actual temperature T_{act} and the frequency factor k.

$$\Delta C_{rel} = -e^{(A+\frac{B}{T})} \cdot t = -ke^{(\frac{\lambda}{T_0} - \frac{\lambda}{T_{act}})} \cdot t \tag{21}$$

The Butler-Volmer Equation describes the fundamental relationship in electrochemical kinetics by looking into the relation between the electrode current and the electrode over-potential of an electrochemical system. Similar to the Arrhenius equation it shows an exponential dependence on the absolute temperature T in K. It is defined according to [12, 27] in (22) with the current density i and the exchange-current density i_0. I is the electrode current and A the electrode area. $\eta = E - E_{eq} < 0$ stands for the activation over-potential with the electrode potential E and the equilibrium potential E_{eq}. α is called the symmetry factor which quantifies the charge transfer at a barrier (here between electrode and surrounding). F and R represent the Faraday constant and the universal gas constant respectively.

$$i = I/A = i_0\left[e^{-\frac{\alpha_{Red}\eta F}{RT}} - e^{\frac{\alpha_{Ox}\eta F}{RT}}\right] \tag{22}$$

Löhn mentions in [62] that a temperature increase leads to an increase in the thermal energy that contributes to the reactions in a system. This means that in general the current density i increases with rising temperatures exponentially.

Aside from a faster and inhomogeneous aging, **safety** problems can also arise through locally increased temperatures, probably caused by internal or external short-circuits, and leading to a thermal runaway. In [107] the different stages of a thermal runaway are described. Wen concludes therein that the thermal runaway can be related to continued self-generated heating. Maleki, who investigated the thermal behavior for the single components of a cell through Accelerated Rate Calorimetry (ARC) in [64], mentions that the self-heating of the cell slowly starts between 123 °C and 167 °C, and after that the thermal runaway starts. "The onset of cell self-heating matches the temperature range of SEI-layer breakdown and decomposition of electrolyte and reaction of that with PE and NE [Author's note: positive electrode and negative electrode] materials. The thermal runaway temperature of the cell matches the temperature at which thermal decomposition of unwashed PE material occurs"[64]. [107] adds that the increased O_2 generation from cathodic materials at higher temperatures also favors the self-heating process.

Inhomogeneities are especially critical for the cell safety since temperature monitoring only takes place on selected spots in today's applications. In large format pouch cells a hot-spot might not be detected on time if the sensor is placed at another point on the cell surface. Space-resolved temperature monitoring is crucial in larger scale cells to be able to detect a local failure promptly.

From all above described facts the desire for a detailed understanding and estimation of the temperature inhomogeneities arises, in order to adjust operating strategies to run the cells under optimal circumstances.

3

TEMPERATURE DEPENDENCY OF CELL PARAMETERS

In this chapter the temperature dependency of different internal cell parameters is evaluated in order to see to what extend temperature inhomogeneities influence the cell parameters over the lifetime. The goal is to investigate if and how these parameters can be used to estimate the internal temperature inhomogeneity.

All methods for temperature detection that are based on internal battery parameters are per-se only ably to detect the temperature median, if no additional sensor is used e.g. on the surface of a cell. In order to be able to detect deviations in the temperature distribution from this median it is therefore necessary to find a measure that shows non-linearity in its temperature dependency. In the following sections, the measures are first recorded on single cells at varying constant temperatures. A simulated cell with temperature distributions is calculated thereof by taking measures from different temperatures in series and analyzing the deviation from the mean temperature. It is assumed that this method provides a good approximation of an inhomogeneously heated cell. The basic setup therefore is depicted in Fig. 9.

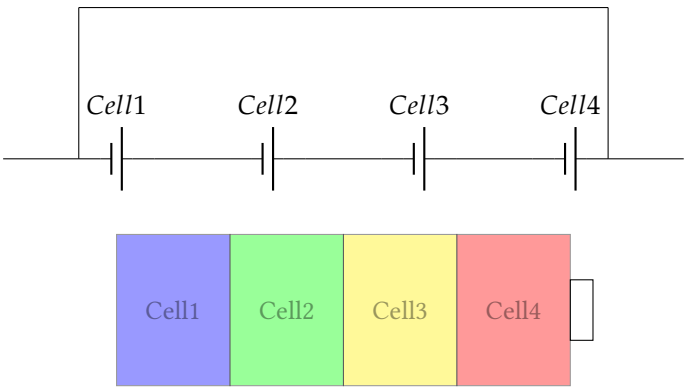

Figure 9: Setup as it is used for the following investigations on temperature inhomogeneity dependency of internal cell parameters. The corresponding temperatures for Cell1 to Cell4 are $T_1 \geq T_2 \geq T_3 \geq T_4$. The average temperature is calculated by $T_{av} = (T_1 + T_2 + T_3 + T_4)/4$.

3.1 CELL IMPEDANCE

The impedance spectrum of cells is widely used to investigate various internal mechanisms and to parameterize Equivalent Circuit Models (ECMs). These models are mainly used to estimate the remaining lifetime or current SOC during operation. For this purpose the models are fed into BMSs. In order to measure the impedance spectra, cells are exposed to alternating currents at varying frequencies. The resulting voltage response is measured and the impedance calculated in the frequency domain. Eq. (23) shows the relationship as it is defined in [48]. $\widehat{V}$ and $\widehat{I}$ represent

thereby the amplitudes of the sinusoidal voltage and current, φ_I and φ_I the phase shift, f is the frequency and t the time.

$$Z(f) = \frac{V(f)}{I(f)} = \frac{\widehat{V}e^{j(2\pi ft+\varphi_V)}}{\widehat{I}e^{j(2\pi ft+\varphi_I)}} = |Z(f)|e^{j\varphi} \text{ with } |Z(f)| = \frac{\widehat{V}}{\widehat{I}} \text{ and } \varphi = \varphi_V + \varphi_I \quad (23)$$

The method for characterization of electrochemical systems called EIS is described by Macdonald in [74] as follows: "EIS involves measurements and analysis of materials in which ionic conduction strongly predominates. Examples of such materials are solid and liquid electrolytes, fused salts, ionically conducting glasses and polymers, and nonstoichiometric ionically bonded single crystals, where conduction can involve motion of ion vacancies and interstitials. EIS is also valuable in the study of fuel cells, rechargeable batteries, and corrosion."[74] Macdonald mentions further that the resulting impedance from measurements is fitted to an equivalent circuit model "whose elements and connectivity were selected [...] to represent the various mass and charge transport physical processes thought to be of importance for the particular system."[74] To obtain the necessary parameters, the used frequency ranges from 10 µHz up to 10 MHz or higher.

In the following, different methods for temperature detection based on impedance spectra are discussed and reviewed if and how they may be suitable for inhomogeneity detection.

3.1.1 *Temperature dependency of the impedance spectrum*

In [51, 85, 89, 92, 93, 96] different approaches for estimating the internal temperature of lithium ion cells based on impedance measurements are described.

Koch introduces in [51] two different approaches for temperature tracking based on impedance measurements: the first approach selects a fixed frequency that shows as little SOC dependency as possibly on either real (Z_{real}) and imaginary part (Z_{imag}) of the impedance or phase shift ($\phi(Z)$) and absolute value ($|Z|$). These approaches were also performed by [93] and [96] respectively. [96] looked into different cell parameters like the Solid Electrolyte Interface (SEI) resistance, the anode impedance and the electrolyte resistance and gained with the help of multiple impedance measurements the dependency of each of those parameters on the temperature. It is mentioned that the effort of parameter acquisition for single components is however very high and the dependency of the phase shift $\phi(Z)$ of the whole cell on the temperature at a defined frequency provides a better approach. Koch looks into the impedance of a whole cell and finds a linear dependency of Z_{imag} at 420 Hz for the investigated cell.

The second approach that Koch describes has been similarly introduced by [85]. The idea is to select a fixed impedance value (real or imaginary part or phase or absolute value) at which the temperature dependent frequency change is tracked. Koch shows a third-order polynomial dependency of the temperature on the frequency at the phase of the impedance $\phi(Z) = 3°$. He finds the latter approach to be better suitable thanks to a reduced noise in this measure even though he finds a higher SOC influence at lower frequency values. Schmidt develops in [93] these methods in order to be able to estimate the mean temperature of a cell accurately with impedance measurement even if different temperature gradients are applied to the cell. Richardson goes one step further in [89]. He claims that based on impedance measurements it is possible to estimate non-uniform temperature distributions in a cylindric cell with the additional knowledge of the surface temperature. To prove this method, he equips a cylindrical cell with one sensor on the surface of the cell and the other sensor at the core of the cell. The cell behavior is then monitored with the help of galvanostatic EIS. The impedance is in a first step calibrated against temperature by performing the measurements in a thermal equilibrium at various temperatures. For each temperature the cell capacity is determined with a Constant Current (CC)/Constant Voltage (CV) charge and discharge cycle. For the actual impedance spectroscopy, the cell is discharged to each SOC with a current of 0.9 C and a resting

after each discharge step until thermal equilibrium between the surface sensor and the core sensor is reached. For the temperature estimation based on impedance measurement, a frequency was chosen at which the dependency of the impedance on the SOC is negligible and the temperature dependency is sufficiently high. The received impedances for the defined frequency are subjected to an Arrhenius fitting as displayed in Eq. (24) with the real impedance Z' constant k, the activation energy E_a, the universal gas constant R and the temperature T. In order to obtain the impedance of the active material from the measured impedance Z'_{meas}, [89] introduces R_{col}, a constant that reflects the electrical conductivity of the current collector, with $Z_{active} = Z'_{meas}(T) - R_{col}$.

$$Z'(T) = k \exp \frac{E_a}{RT} \tag{24}$$

The herewith estimated maximum temperature values defer by only 3 % from measured values, which suggests this method to be well suitable for inhomogeneity approximations. After the above described calibration process, the impedance measurement at the selected frequency combined with a surface temperature sensor gives a good approximation of the inhomogeneity between core and surface of the cell.

In all aforementioned publications it is proven that the impedance provides a good parameter for estimating the internal cell temperature.

Aside from the cell impedance at defined frequencies, an impedance spectrum that covers a wide range of frequencies provides information about internal cell parameters. A common approach is to fit different parts of the impedance spectrum to an ECM and therewith gain information about single parameters at defined states of the cell. In the following a short summary of this approach is given in order to provide a background for further considerations.

Fig. 10 shows an exemplary Nyquist plot of the electrochemical impedance spectrum of a 6 Ah cell from *Enertech* at 0 % SOD and 20 °C. From this plot, different parameters of the cell can be extracted by creating an ECM. [15] mentions that an equivalent circuit as depicted in Fig. 11 represents the Alternating Current (AC) behavior of a Li-ion cell accurately. The inductive part L of the Electrochemical Impedance Spectroscopy (EIS) is represented by the positive values of Z_{imag}. It depends only on the geometry of the cell, while all other parameters depend at least on SOC and temperature, according to [16]. L is therefore neglected in further discussions. R_i is the ohmic resistance, which is a combination of electrolyte resistance, the resistance of the active particles and current collectors and the connection resistance. R and C represent a non-linear RC-circuit that is displayed in the diagram by a semi-circle. $\omega = 1/RC$ builds the center of the semi-circle and R its diameter. The frequency response of an RC-circuit can be generally expressed as shown in (25). ω_c is thereby the cut-off frequency. In case of the battery ECM this circuit brings in the time dependency.

$$\omega_c = 2\pi f = \frac{1}{2\pi RC} \tag{25}$$

The Z_{ARC} element, which leads to a depressed semi-circle in the complex plane, is according to [16] a parallel combination of a constant-phase element and a resistance. The equation defining the Z_{ARC} element is given in (26) according to [16] with ξ representing the depression factor of the semi circle, the resistive part R and the Z_{ARC}-specific factor A. An approximation of this element is generally given by multiple RC circuits connected in series [11, 15, 16].

$$Z_{ARC} = \frac{R \cdot A \cdot (j\omega)^{-\xi}}{R + A \cdot (j\omega)^{-\xi}} \qquad \text{with } 0 < \xi \leq 1 \tag{26}$$

Z_W is the Warburg impedance that represents mixed diffusion processes in a porous electrode and is depicted by a slope of 0.5 in the Nyquist plot of Fig. 10.

It is, according to [24] and [41] described through (27) with the gas constant R, the temperature T, the lithium concentration c, $z = 1$ as the charge number for Li-ion batteries, the Faraday

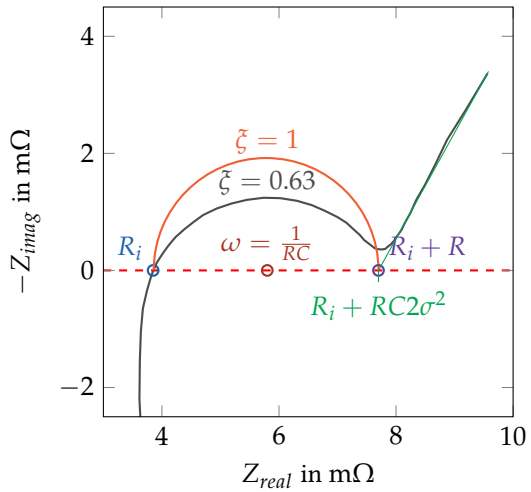

Figure 10: Nyqist plot from an EIS of measured at a 6 Ah cell at 0 % SOD and 20 °C in dark gray with the different elements of the ECM and the mass transfer parameter σ.

constant F, the diffusion distance $l = r$, which equals to the particle radius, the contact area S between electrode and electrolyte and D as the diffusion coefficient. S is defined in (28) according to [24] with the total electrode volume V_{El}, the porosity ε, the inactive part of the material p_{inact}, the volume of a single particle V_{part} and the particle radius r. [41] shows in his thesis that this equation is only valid for a finite diffusion layer with an ideal reservoir. In this case, the Warburg impedance is rather depicted by a slope of 0.5 followed by a semi-circle for very low frequencies in the Nyquist plot.

$$Z_W = \frac{RT}{cz^2F^2S} \cdot \frac{\tanh\left(l \cdot \sqrt{j\frac{\omega}{D}}\right)}{\sqrt{j\omega D}} \tag{27}$$

$$S = \frac{V_{El}(1-\varepsilon)(1-p_{inact})}{V_{part}} 4\pi r^2 \tag{28}$$

For a semi-infinite diffusion layer [41] provides Eq. (29) as the valid equation. For this case, the slope in the Nyquist plot remains at 0.5 over the whole low frequency range.

$$Z_{W\infty} = \frac{RT}{cz^2F^2S} \cdot \frac{1}{\sqrt{j\omega D}} \tag{29}$$

In a third case described by [41] a finite diffusion layer with a non-permeable boundary layer is assumed. In this case, the Nyquist plot starts with a slope of 0.5 and leads towards $Z_{imag} \to \infty$ for very low frequencies. The respective equation is given in Eq. (30).

$$Z_{WL} = \frac{RT}{cz^2F^2S} \cdot \frac{\coth\left(l \cdot \sqrt{j\frac{\omega}{D}}\right)}{\sqrt{j\omega D}} \tag{30}$$

Since the differences in all equations are only affecting the very low frequency range, which is not considered here, Eq. (29) can be used as an approximation.

Fig. 12 shows the Nyquist plots for different temperatures and for different SODs of the above mentioned 6 Ah cell from *Enertech*. In Fig. 12a data of a fully charged cell at different temperatures are displayed, while Fig. 12b demonstrates the impedance spectra at 38 °C for different SODs.

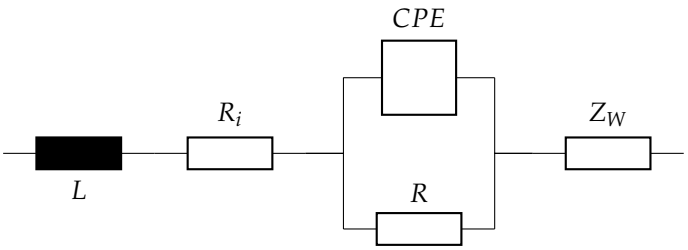

Figure 11: Basic ECM of a Lithium ion cell with the elements shown in Fig. 10.

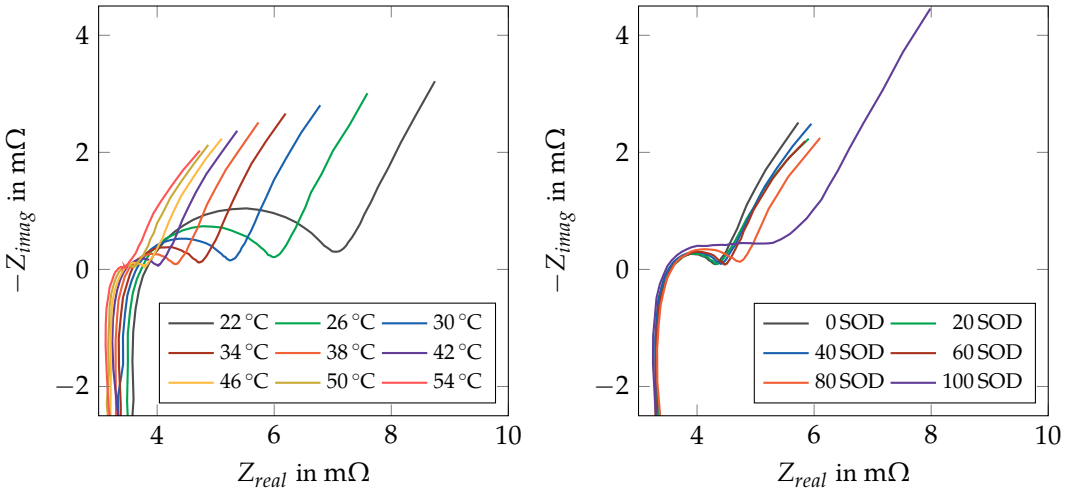

(a) EIS plot for different temperatures at 0 % SOD.

(b) EIS plot for different SODs at 38 °C.

Figure 12: Nyquist plots for EIS measurements of a 6 Ah pouch cell for different temperatures and different SODs.

The slope which represents the Warburg impedance stays, as expected, the same for all measurements. The ohmic resistance at $Z_{imag} = 0$ displays decreasing values in Z_{real} over an increasing temperature, while for different discharge states, no difference in this point is visible. Also the diameter as well as the compression factor of the Z_{ARC}-element depend much stronger on the temperature than on the discharge state, probably due to the temperature dependency of the inner resistance. This resistance corresponds to the charge transfer resistance which can be deducted from the Butler-Volmer equation which is described in detail in Section 2.5. The charge transfer resistance is proportional to the temperature devided by the exchange current density T/i_0.

Figs. 13 and 14 show the same data separated by real and imaginary part plotted over the frequency. The detail plots in each of the figures show for every distribution the maximum difference between the values (i.e. the difference of the Z_{real} and Z_{imag} values between highest and lowest temperature and between highest and lowest SOD). In Z_{real} the strongest dependencies on SOD and temperature are in a similar frequency range. Z_{imag} shows a strong peak in temperature dependency where the SOD dependency is low at around 50 Hz and still a decent dependency at the minimum of SOD dependency. This frequency range seems to be most suitable for temperature detection. The frequency value where $Z_{imag} = 0$ provides a promising point to detect temperature dependencies. It is marked in all diagrams. This finding can be either used by tracking the frequency change at $Z_{imag} = 0$ or the change in Z_{real} at this point over the frequency. Both alternatives are depicted in Fig. 15a and Fig. 15b respectively. The frequency shows a strong dependency on the temperature. The linear approximation results in a maximum error of $E_{max} = 5.72\,\%$ for the frequency dependency and $E_{max} = 13.22\,\%$ for the dependency of R_i on the temperature respec-

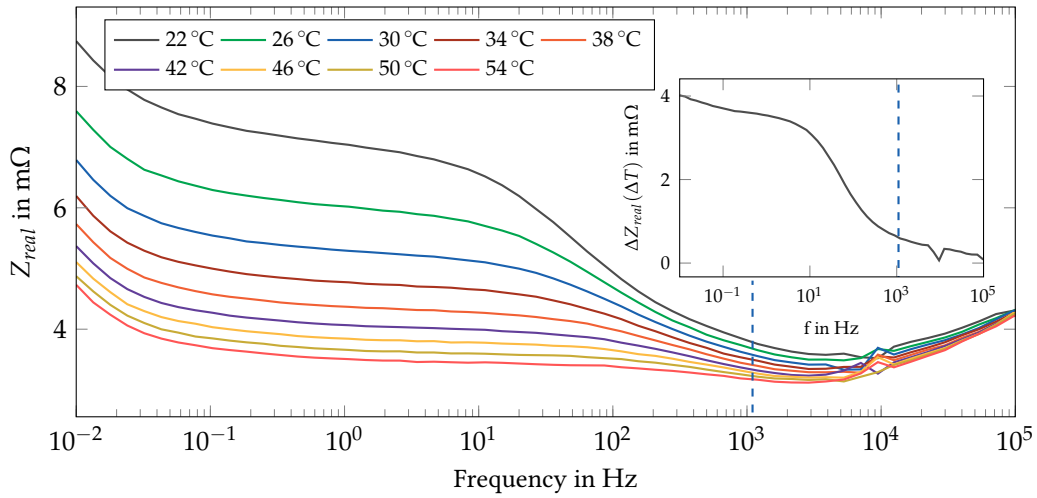

(a) Z_{real} over frequency for different temperatures at 0 % SOD.

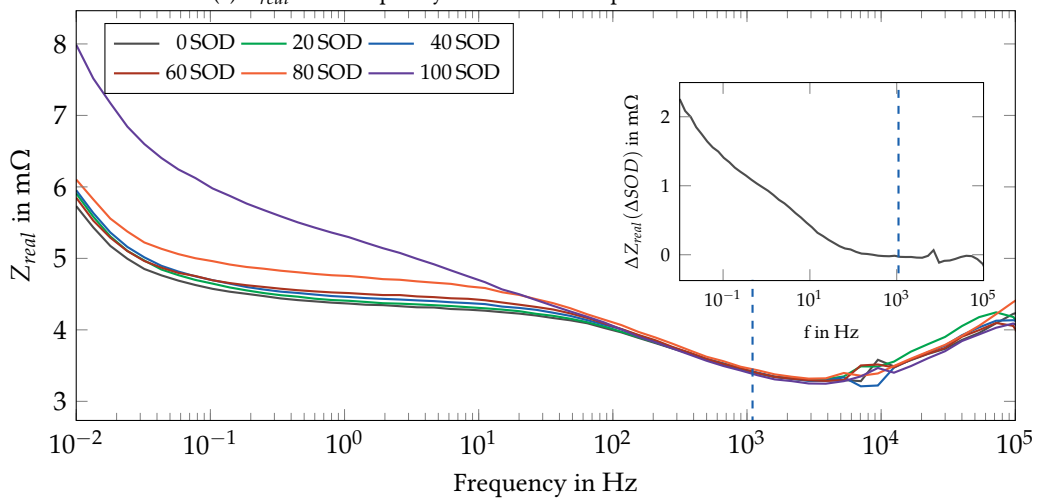

(b) Z_{real} over frequency for different SODs at 38 °C.

Figure 13: Real part of the impedance of EIS measurements of a 6 Ah pouch cell for different temperatures and different SODs with the difference between minimum and maximum temperature and SOD ΔZ_{real} in the close up.

tively. An error of less than 6 % suggests a quite linear behavior. The second approach of tracking the internal resistance change provides bigger non-linearities. A good fit can be reached with a cubic approximation. However, the dependency of R_i results in very small changes in the µΩ range which makes distinguishing between different inhomogeneous states rather hard. This measure is therefore not further regarded and a closer look taken into the suitability of the temperature-depending frequency change.

3.1.2 *Inhomogeneity detection with the help of impedance spectra*

To see the suitability for inhomogeneity detection of the temperature dependency of certain frequencies in the impedance spectrum, different tempered areas of the cell are considered to be n smaller cells connected in parallel. Distributions with variable differences from the average are

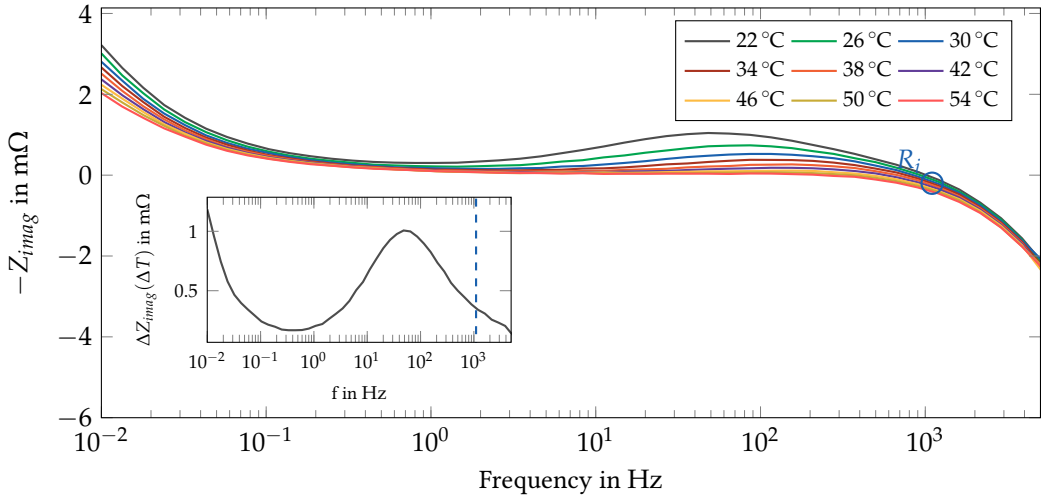

(a) Z_{imag} over frequency for different temperatures at 0 % SOD.

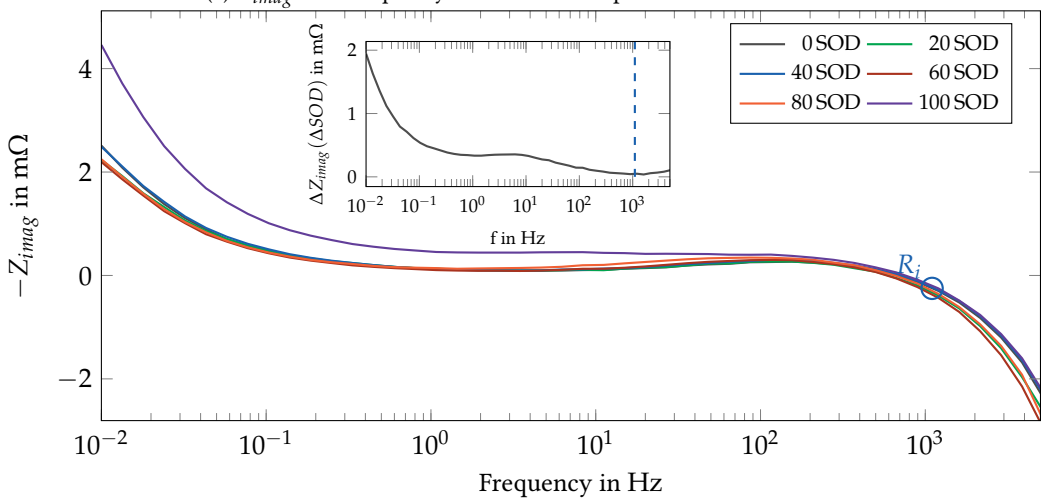

(b) Z_{imag} over frequency for different SODs at 38 °C.

Figure 14: Imaginary part of the impedance of EIS measurements of a 6 Ah pouch cell for different temperatures and different SODs with the difference between minimum and maximum temperature and SOD ΔZ_{imag} in the close up.

compared to EIS measurements of cells at constant average temperature. The total impedance is then calculated according to (31).

$$Z_{tot} = Z_{tot,real} + i \cdot Z_{tot,imag} = \frac{1}{\sum_{i=1}^{n} \frac{1}{Z_i}}, \qquad \text{with } Z_i = Z_{i,real} + i \cdot Z_{i,imag} \tag{31}$$

Fig. 16 and Fig. 17 show the resulting impedance plots for a cell with four temperature regions in comparison to a homogeneously heated cell. The underlying temperatures are given in table Table 3. The detail plots in Fig. 17 show the difference for each inhomogeneous distribution compared to the homogeneous distribution. The SOD-dependency for the respective measure is also pictured in these detail plots. Even for large temperature gradients within one cell (Cell 5 and 6) the maximum differences $\Delta Z_{real,max} = \Delta Z_{real,inhom} - \Delta Z_{real,hom}$ and $\Delta Z_{imag,max} = \Delta Z_{imag,inhom} - \Delta Z_{imag,hom}$ are only in the lower mΩ range for frequencies with a small SOD. In Table 3 the maximum deviation $\Delta Z_{real,max}$ and $\Delta Z_{imag,max}$ of the impedance for inhomogeneous temperature distributions (Cell2

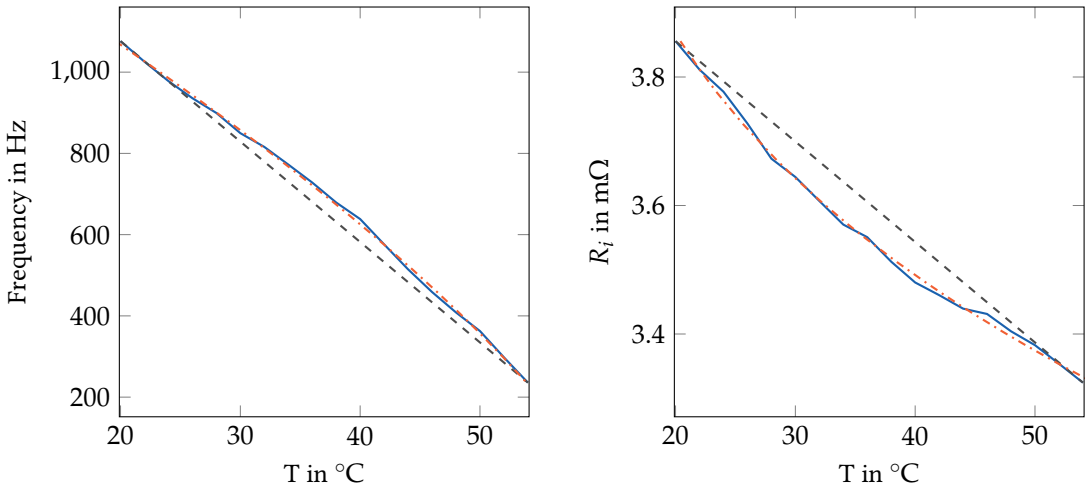

(a) Frequency over the temperature where $Z_{imag} = 0$ at 0 % SOD.

(b) R_i over the temperature at 0 % SOD.

Figure 15: Dependency of Z_{real} and frequency on the temperature where $Z_{imag} = 0$ with linear approximation (dashed) and cubic approximation (dash-dotted). The blue continuous line represents the measurement data.

to Cell6) compared to a homogeneous distribution (Cell1) is presented. Although, as [104] already suggests, the EIS semi-circle shows a diameter increase of around 2 mΩ for larger temperature gradients of more than 10 K, an inhomogeneity detecting without bigger interferences with the SOC is hardly possible.

Table 3: Temperatures for cells with $n = 4$ different homogeneous and inhomogeneous temperature distributions that are used for EIS investigations in Fig. 16 and Fig. 17 with the respective maximum deviation $\Delta Z_{real,max}$ and $\Delta Z_{imag,max}$ from the homogeneous state (Cell1). The values are the maximum values taken from the diagrams in Fig. 17 (small windows).

Cell 1	Cell 2	Cell 3	Cell 4	Cell 5	Cell 6
38 °C	36 °C	34 °C	36 °C	30 °C	22 °C
38 °C	38 °C	36 °C	36 °C	34 °C	30 °C
38 °C	38 °C	40 °C	40 °C	42 °C	46 °C
38 °C	40 °C	42 °C	40 °C	46 °C	54 °C
$\Delta Z_{real,max}$	0.19 mΩ	0.55 mΩ	0.39 mΩ	0.85 mΩ	1.33 mΩ
$\Delta Z_{imag,max}$	0.93 mΩ	0.17 mΩ	1.86 mΩ	0.07 mΩ	0.09 mΩ

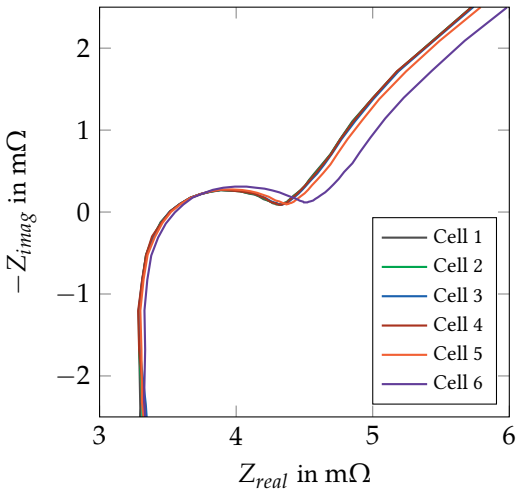

Figure 16: EIS for different inhomogeneous temperature distributions in comparison to a homogeneous distribution (Cell 1) with average temperature 38 °C at 0 % SOD.

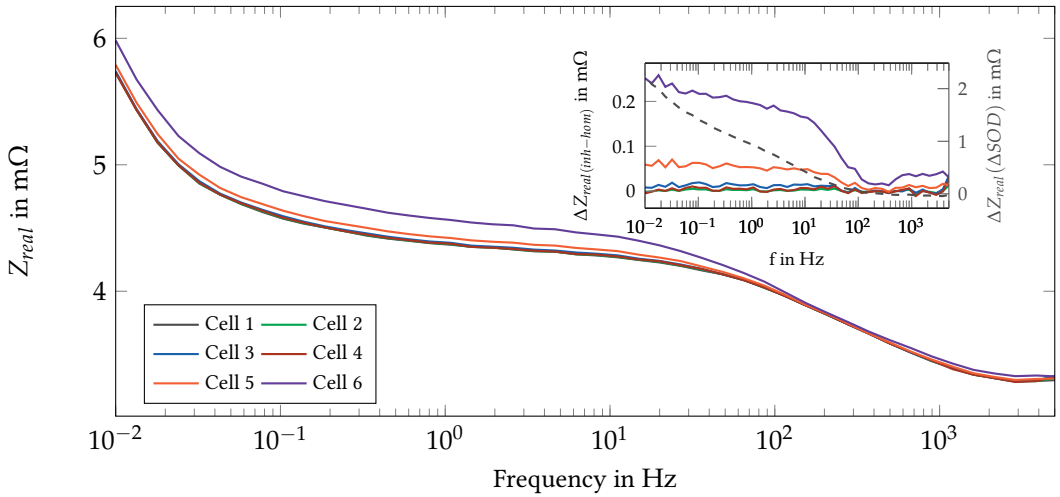

(a) Z_{real} over frequency for different temperature distributions with four unit cells. . The small window displays the differences in impedance between homogeneous and inhomogeneous distribution and the SOD-dependency (dashed line).

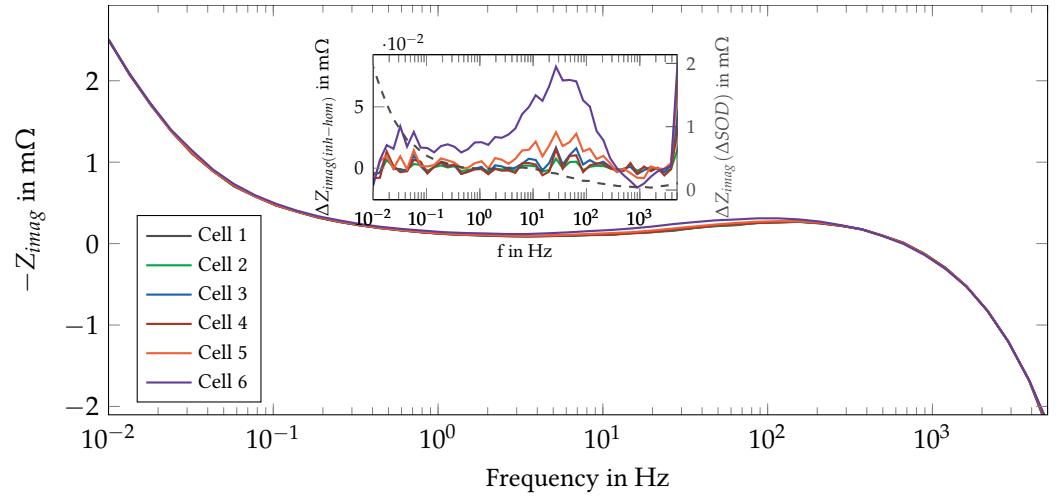

(b) Z_{imag} over frequency for different temperature distributions with four unit cells. . The small window displays the differences in impedance between homogeneous and inhomogeneous distribution and the SOD-dependency (dashed line).

Figure 17: The impedance over frequency for different inhomogeneous states at 0 % SOD. In the small charts the difference between homogeneous and inhomogeneous cells is displayed as well as the SOD-dependency over the frequency range.

3.2 RESISTANCE

As already shown in Section 3.1, the cell resistance R_i provides a clear dependence on the temperature. Fig. 15b demonstrates this correlation. A cubic dependency with a maximum error $E_{max} = 2.4\,\%$ is displayed.

In this subsection, the single components of the inner resistance are further investigated concerning their suitability for inhomogeneity detection. The following four components contribute to this:

- Electrolytic resistance
- Resistance of current collectors
- Resistance of active material
- Connection resistance

The connection resistance is not described closer here, since it is supposedly not connected with in-cell inhomogeneity.

3.2.1 *Electrolytic resistance*

The specific electrical resistance ρ of an electrolyte as the reciprocal value of the specific electrical conductivity κ is defined in (32) with the ionic charge number z, the elementary electric charge e_0, the ionic mobility $\mu_\pm$ and the ion density $n_\pm$ [99].

$$\rho = \frac{1}{\kappa} = \frac{1}{ze_0(\mu_+ n_+ + \mu_- n_-)} \tag{32}$$

In [105] a relationship between conductivity κ in $\mathrm{S\,m^{-1}}$, the $LiPF_6$ concentration c in $\mathrm{mol\,L^{-1}}$ and the absolute temperature T in K according to (33) is developed based on empirical data from research on $LiPF_6$, which is the most commonly applied electrolytic salt in Li-ion batteries. κ_{ij} represent polynomial expansion coefficients and are found by basic fitting of experimental data to the model. The coefficients hold the scaling unit $\mathrm{L^i/(mol^i K^j)}$.

$$\kappa_{Val} = c\left(\sum_{i=0}^{n}\sum_{j=0}^{k}\kappa_{ij}c^i T^j\right)^2 \tag{33}$$

$$\kappa_{Ecker} = \frac{1}{T}\kappa_0 e^{\frac{-E_a}{RT}} \tag{34}$$

Ecker et al propose in [24] the Arrhenius equation to best approximate the temperature dependency of the electrolytic conductivity according to (34). The activation energy is given as $E_a = (17.12 \pm 0.13)\,\mathrm{kJ/mol}$, T represents again the temperature, R is the universal gas constant and κ_0 a proportionality constant. Fig. 18a shows the two measures κ_{Val} and κ_{Ecker} over the temperature in comparison. The concentration is chosen to be $c = 1\,\mathrm{mol\,L^{-1}}$, the constant $\kappa_0 = 3.55 \cdot 10^5 \mathrm{S\,m^{-1}}$. For lower temperatures up to 30 °C the two measures are in good agreement. This is the temperature range that is used for parameterization in [24]. [105] and [28] both suggest (33) to be more suitable than the Arrhenius approach.

To be able to detect inhomogeneities with a parameter, non-linearities over the temperature for this parameter are necessary. When however looking at the linear approximation to κ_{Val} in Fig. 18a, it is obvious that the non-linearity of this parameter is negligible. Inhomogeneity detection is therefore not possible based on the conductance of the electrolyte.

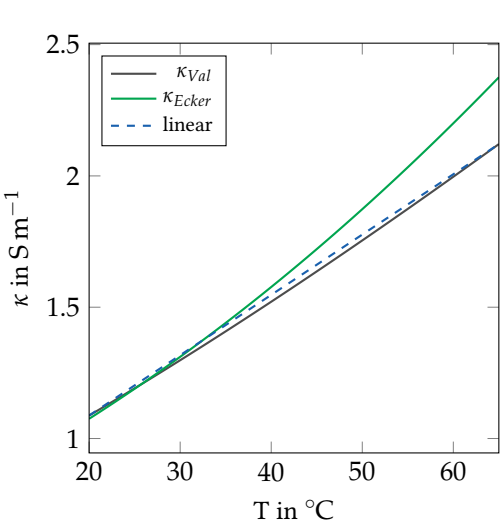

(a) Electrolytic conductivity κ over temperature.

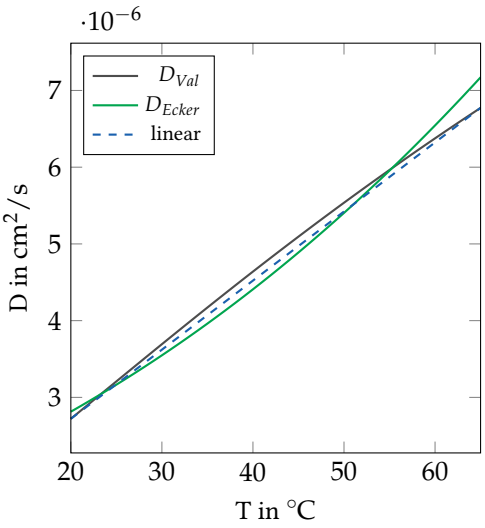

(b) Electrolytic diffusion coefficient D over temperature with an assumed concentration of $c = 1\,\mathrm{mol\,L^{-1}}$.

Figure 18: Electrolytic conductivity and diffusion from [24] and [105] in comparison to a linear approximation.

3.2.2 *Resistance of current collectors and active material*

The current collectors of the cells on which active materials of anode and cathode are coated consist usually of a Copper (Cu) foil for the anode and of an Aluminum (Al) foil for the cathode. At a temperature range between 0 °C and 200 °C the dependency of the resistance of metals can be approximated with a linear function according to (2). The linear temperature coefficients are $\alpha_{Cu} = \alpha_{Al} = 3.9 \times 10^{-3}\,\mathrm{K^{-1}}$ at room temperature[94]. This linearity, as mentioned before for the electrolyte forbids again to detect temperature inhomogeneities with the respective parameter.

For the active material of the electrodes it is, according to [24] not possible to make a universal statement. It is mentioned that values for the conductivity of electrodes vary in literature by orders of magnitude. This is attributed to different porosities, binders, SEI thicknesses etc. In the described measurements variations of 60 % in the conductivity value have been observed. A temperature dependency is not mentioned. Since the total inner resistance R_i as it is represented in above shown EIS measurements shows a linear dependency on the temperature, it can be assumed that also for the active materials of the electrode a linear dependency is present and therefore temperature inhomogeneity not detectable.

3.3 OPEN CIRCUIT VOLTAGE AND ENTROPY

The Open Circuit Voltage(OCV) is another cell-internal parameter which shows a dependency on temperature. The variation in OCV is a result of entropy changes in the reaction process due to temperature changes[104]. The general relation is displayed in Eq. (36). In order to investigate this dependency and the suitability for inhomogeneity detection, *18650* cells with LFP cathodes and graphite anodes from *PHET* and *A123* have been researched in comparison to *18650* cells with LFP cathodes and lithium-titanate (LTO) anodes. These LFP-based cell types show the biggest temperature dependency in the OCV compared to other chemistries. The reason why *18650* are applied here is that cells with LTO anodes were not available in pouch cell design. To make the measurements more comparable, cells from the same shape have been employed.

The cells are cycled to 10 %SOC, 30 %SOC, 50 %SOC and 90 %SOC respectively with 1 C discharge and charge rate, by fully charging the cell each time followed by a discharge to the desired SOC. A pause of 48 h at room temperature afterwards ensures that the system is in full relaxation state, before the temperature cycle is performed. The temperature cycle starts at 25 °C and goes in steps of 2 K down to −20 °C, up to 60 °C and back to room temperature. The temperature is adjusted in steps of 2 K. After each temperature step is set, a pause of 20 min is made so that the OCV is properly reached. In order to be able to compare the measurements despite the different voltage levels, the gradient $\Delta OCV = OCV(T) - OCV(T_{max} = 60\,°\mathrm{C})$ is used. Figs. 19a to 19c show the resulting graphs. A strong hysteresis is visible for each graph with an offset of 1 mV to 2 mV. The reason for the offset cannot be completely determined. However, since the whole cooling and heating process took over one day it can be probably attributed to self-discharging effects of the cell. This is especially likely since the self-discharge increases with higher temperatures according to Arrhenius' equation. The reasons for the hysteresis are researched in [21]. While one rather small influencing factor is the impedance, another reason given are the different reaction pathways during charge and discharge. This is explained by the fact, that the multiplicity of particles in the system with different sizes shows varying thermodynamical behaviors.

While for both graphite-LFP cells the graphs look very similar and show a decent dependency on the temperature, the temperature dependency of the OCV on the LTO-LFP cell is significantly smaller and in the same range as the offset.

Fig. 19d shows only the heating process for the *A123* cell. The graphs can be well approximated with a third-order polynomial function resulting in an error of less than 0.1 %. Depending on the SOC however, the maximum deviation from linearity is small between 0.1 % and 0.39 %. The diagrams in Fig. 19 show that the temperature dependency is strongly SOC-dependent. A similar dependency is shown in [68] for $LiCoO_2$ cells. This rather linear behavior has been already suggested by [104], [53] and [109]. Taylor's first order expansion (35), which is introduced therein, provides the correlation of OCV and entropy change. In this equation V_{ref} is the OCV at a reference temperature T_{ref} and the term $\frac{\partial V_{OC}}{\partial T}$ is a measure for entropy changes according to (36) with the charge number $z = 1$ for lithium ions and the Faraday constant F.

$$V = V_{ref} + \left(T - T_{ref}\right) \frac{\partial V_{OC}}{\partial T} \tag{35}$$

$$\Delta S = zF \frac{\partial V_{OC}}{\partial T} \tag{36}$$

The linear behavior along with the hysteresis between heating and cooling makes the OCV as a parameter to determine temperature inhomogeneity not suitable. In addition, the strong SOC-dependency along with the required waiting time to reach the OCV's equilibrium state hinders the inhomogeneity determination with the help of this method. Since the entropy is proportional to the OCV, the same is valid for this measure.

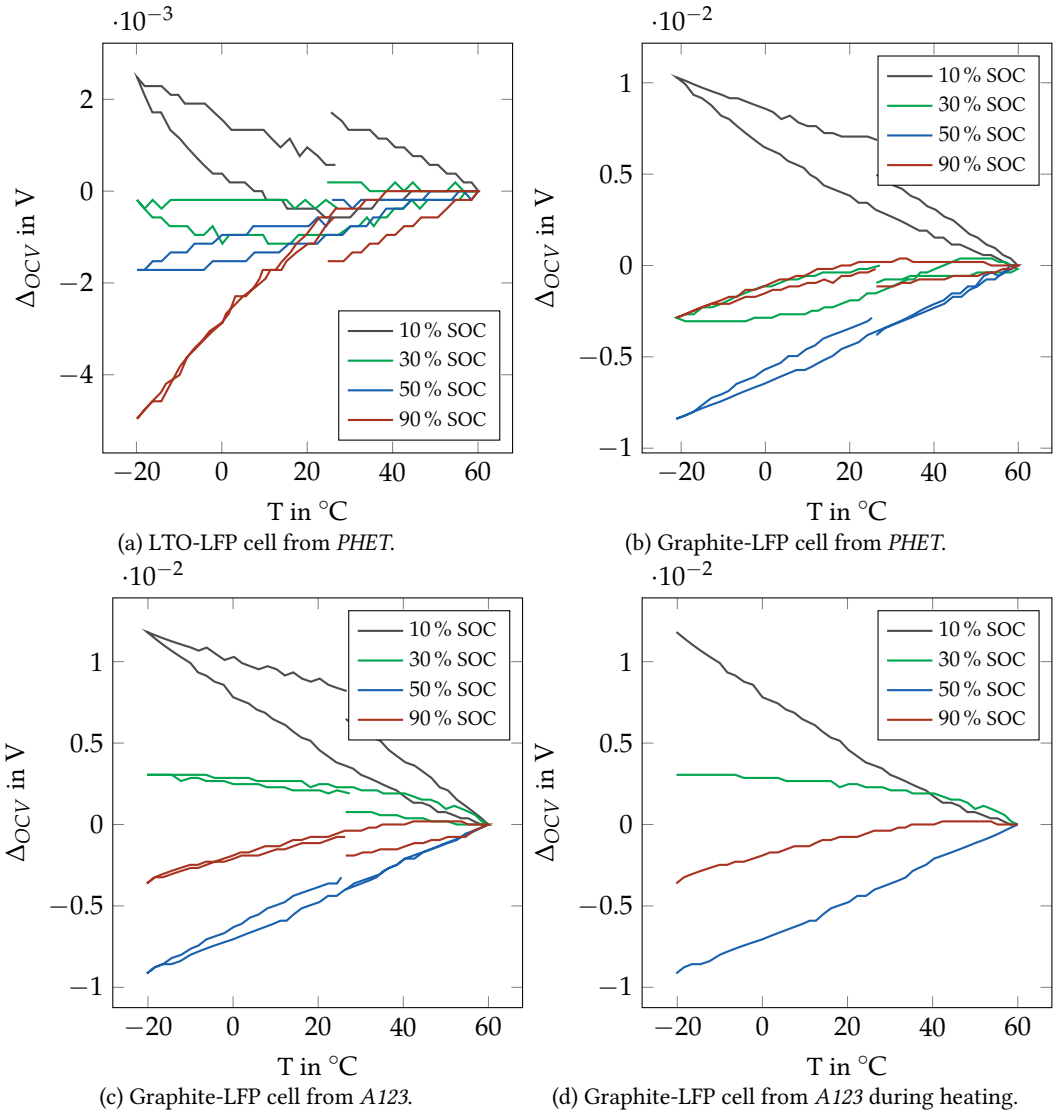

(a) LTO-LFP cell from *PHET*.

(b) Graphite-LFP cell from *PHET*.

(c) Graphite-LFP cell from *A123*.

(d) Graphite-LFP cell from *A123* during heating.

Figure 19: OCV gradient over temperature for different cylindrical cells.

3.4 CAPACITY

It has been mentioned before in Section 2.5 that the calendar life-time of a cell, which is determined by the relative capacity fade, is depending on the temperature according to Arrhenius' equation (18). Since the capacity fade is a perpetual effect, this behavior is not relevant for the here researched effects. [109] however mentions, that the battery capacity as a product of discharge current and discharge time decreases significantly with lower temperature.

This effect is researched based on a 6 Ah pouch cell from *Enertech*. The cell is cycled with 1 C full cycles with 1 h pause between the Constant Current - Constant Voltage (CC-CV) charge and CC discharge. After the discharge, 1 h pause is made before increasing the temperature in the used temperature chamber stepwise by 2 K. A temperature range from 21 °C to 55 °C is therewith covered. After the temperature increase, another pause of 1 h is made before the next full cycle.

Fig. 20a shows the resulting charge and discharge capacity over temperature and Fig. 20b the respective discharge profiles. A clear non-linear dependency is visible which, in both cases, can be approximated with a fifth order polynomial function. The non-linearity here is a good premise

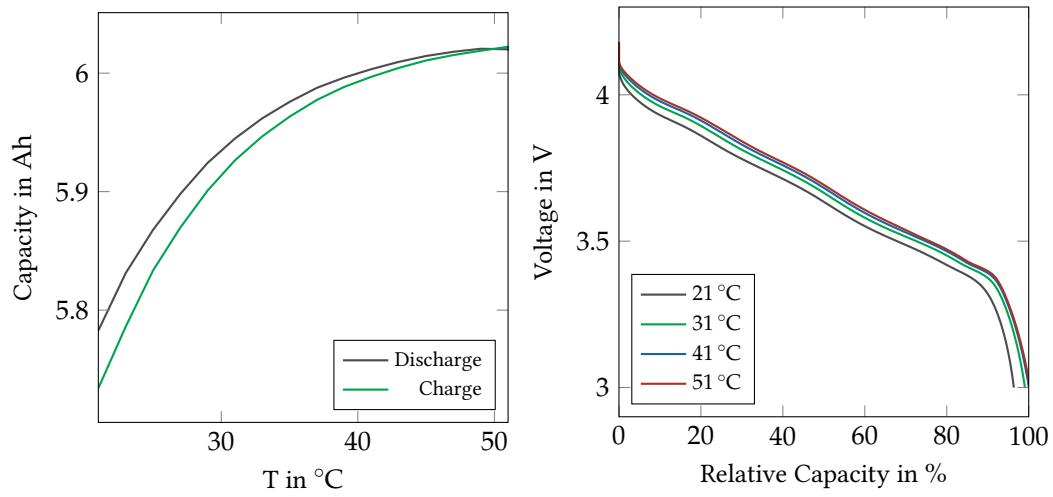

(a) Charge and discharge capacity over temperature. (b) Discharge profiles at different temperatures.

Figure 20: Temperature dependency of the cell capacity of a 6 Ah pouch cell.

for estimating inhomogeneities, as mentioned before. However, when looking at the combined curves with a 20 K temperature gradient in comparison to the curve at average temperature, discrepancies of less than 2 % are visible only at higher discharge states. This behavior is illustrated in Fig. 21. The curve for the combined temperature was simulated based on the measurements at various temperatures above, by assuming a parallel connection of two cells with homogeneous temperatures of 21 °C and 41 °C. Since temperature gradients in reality are in most cases smaller than 20 K and temperature distributions are rather continuous, the discrepancies shown in Fig. 21 are not big enough to detect inhomogeneities in a normal operation range. In addition to that, the approximation used for the simulated discharge profile in Fig. 21 assumes that the temperature during discharge and charge is identical, which in reality is hardly the case and makes this method even more unfavourable.

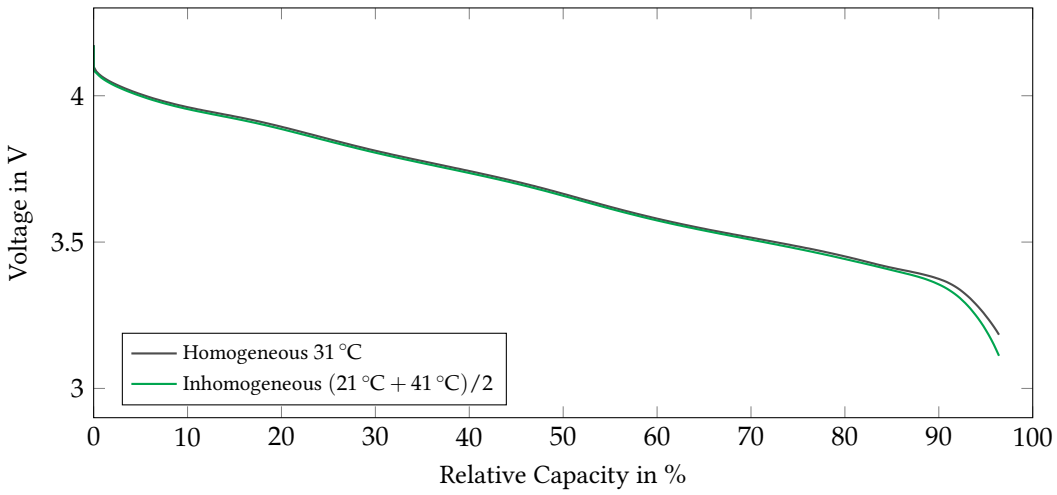

Figure 21: Simulated discharge profile for homogeneous 31 °C in comparison to the profile with a gradient of 20 K.

3.5 DIFFUSION

Aside from the conductance, according to [105], [24] and [28] the electrolyte diffusion shows also a dependency on the temperature. While [24] mentions the Einstein relation (38) to be a valid description for the diffusion, [28] and [105] found another relation according to (37). Both equations show additionally a dependency on the $LiPF_6$ concentration c, while k_B represents the Boltzmann constant, e the elementary charge and N_A the Avogadro constant. The parameters in Eq. (37) are absolute measures. Fig. 18b shows the two measures in comparison for a concentration of $c = 1\,\mathrm{mol\,L^{-1}}$.

$$D_{Val} = 10^{-0.22c-8.43-\frac{54}{T-229-5c}} \tag{37}$$

$$D_{Ecker} = \frac{\kappa_{Ecker} k_B T}{e^2 N_A c} \tag{38}$$

Both measures are displayed in Fig. 18b and show a similar behavior for temperatures up to 50 °C with a good linear approximation in this temperature range. Since for the conductivity however the measure defined by [105] is supposedly more accurate, the same assumption is made for the diffusion. Since this measure is again quite linear over the temperature, it is not suitable for inhomogeneity detections.

As mentioned above, the Warburg impedance described by (27) represents the diffusion effects in the cell. While the Warburg impedance Z_w can be determined from EIS measurements, there is no explicit solution for the solid state diffusion coefficient over the temperature. Values in literature vary by many orders of magnitude depending on the used chemistry (e.g. [28, 58] and [100]). [24] discusses two different methods to determine the solid-state diffusion. Huge discrepancies are shown between the results of the temperature depending diffusion. A clear measure for the overall diffusion in the cell is therefore hard to develop.

3.6 CONCLUSION: POSSIBILITY OF INHOMOGENEITY DETECTION WITH CELL PARAMETERS

The previous discussions in this chapter looked at different parameters and processes in the cells that show temperature dependency. Based on literature data as well as different measurements these dependencies have been highlighted and the possible usage for inhomogeneity detection investigated.

While some previous publications suggested a strong influence of inhomogeneity on impedance spectra, it could be shown here that for the used cells, only very big gradients with a rather discrete temperature distribution have a visible and measurable impact on the spectra. The biggest detectable influence is in a frequency range, where also the biggest dependency on the SOC could be detected. A clear detection of temperature inhomogeneity is therewith hardly possible.

Another temperature dependent parameter is the open circuit voltage. It is however not suitable for temperature detection and especially not for inhomogeneity investigation for several reasons: on one hand, there is a strong hysteresis between heating and cooling. On the other hand, the OCV is reached after relaxation of the system. In this case a 20 min pause is made for the temperature to adjust. During cycling the relaxation takes even longer and a pause of up to 48 h is necessary to reach the equilibrium state. The parameter is therefore not suitable for live inhomogeneity determination.

The resistance as well as the diffusion show a very linear behavior in the researched temperature range and are therefore also not eligible.

The only parameter, which shows enough non-linearity to be maybe suitable for inhomogeneity detection is the charge or discharge capacity. However, variations with 20 K temperature gradient

reached only 2 % discrepancy from the homogeneous state. Additionally, the capacity is only measurable after a full discharge or charge cycle. An on-line determination is therewith also hardly possible.

Concluding it is to say, that internal cell parameters do not provide enough information about the temperature inhomogeneity in a cell without additional sensors. As suggested before, temperature measurements at multiple points and preferably in the cell are crucial.

4

TEMPERATURE SENSORS AND RELATED CONNECTION STRATEGIES FOR IN-SITU MEASUREMENTS

Parts of this chapter have been published in [69–72].

In most current applications, monitoring is performed by attaching sensors to the surface of battery cells, as highlighted in [68]. However, this approach has severe drawbacks, particularly in large scale applications where active cooling is applied. In this scenario, battery cells are actively cooled from their surface either using cold air or liquid. The resulting temperature discrepancy between the cell surface and its interior might become significant [6], especially in the event of a thermal runaway [29]. Consequently, the delay in time response when detecting the actual cell temperature may result in an inappropriate battery management when only the surface temperature is monitored. This effect is also addressed later in Section 6.2. In-situ temperature monitoring as described in [56, 59, 76] is therefore of great value.

To gather space resolved temperature data for better detection of local inhomogeneities, a sensor matrix with measurement points distributed over the whole area of the cell is desirable. However, the collection of a large amount of sensor data is challenging when applying in-situ sensing as pointed out in [69, 71, 76] and in the following sections.

4.1 DEVELOPMENT AND INTEGRATION REQUIREMENTS

Previous publications [71, 72] listed requirements for the integration of measurement electronics into Li-ion battery cells. It is elaborated that particularly for laminated Li-ion pouch cells, the integration of measurement electronics is challenging due to the limited space, the sensitivity of electro-chemical processes on disturbances and the difficulty in sealing the pouch laminate when wires are fed through.

The overall goal when integrating measurement electronics into a battery cell is to affect the behavior of the cell as little as possible while providing vital information about internal cell parameters like the temperature throughout a whole battery life. This goal can be reached by considering the following criteria.

Chemical requirements: $LiPF_6$-based solutions are widely used as electrolyte in state-of-the art Li-ion cells. These solutions however react with traces of water to HF according to (39) and (40). Under normal circumstances batteries are assembled in super-dry environments to eliminate any traces of water since HF would also damage the cell massively. The applied electrolytic solvents are non-aqueous. The development of HF is therefore normally not an issue. However, since the sensors described here are inserted in an laboratory environment in sometimes self-made cells, the resistance against HF is required for research applications. The used components need therefore to withstand this acid to ensure an operation of the system throughout the entire battery life.

$$LiPF_6 \longrightarrow LiF + PF_5 \tag{39}$$

$$PF_5 + H_2O \longrightarrow POF_3 + 2\,HF \tag{40}$$

Electrochemical and electrical requirements: The location of the measurement system needs to be chosen such that the ionic flow between the active materials of anode and cathode is not interrupted. This is further elaborated in Section 4.5. Materials for the used devices have to be selected such that inertness in the given environment is ensured or a sufficient and long lasting coating is provided.

Since Li-ion cells have high potentials at the positive electrode and low potentials at the negative electrode, oxidation and reduction of the applied materials is fostered.

To ensure the electrical functionality of both cell and sensor and, hence, to avoid short circuits between electrodes and sensor as well as to guarantee the chemical inertness, a passivation layer on the sensor for electrical insulation is necessary. Potential materials that can be used for passivation are polyimide or parylene which promise both stability in the cell environment. These materials are discussed comprehensively below.

Shape requirements: For most applications, especially in the mobile or automotive sector, space is a limiting factor which leads to the demand of cells with a maximized energy density. Sensors or rather sensor matrices for space resolved measurements, should ideally be placed between electrodes to measure the temperature where it emerges and to detect hot spots. Irregularities in the distance between two electrodes can however lead to an inhomogeneous current density in the electrodes and therefore temperature hot spots or accelerated aging, as elaborated in Chapter 2. To avoid this, the integrated electronics have to be as small and flat as possible.

4.2 SIMULATION FOR ESTIMATING INHOMOGENEITY DISTRIBUTIONS

Parts of the content of this section have been already published in [71]. For an initial assessment of the occurring temperature spread within cells, and hence the necessary placement of sensors, three-dimensional simulation models provide good estimations. For the experiments described in Section 4.7, simulation studies have been carried out with the aid of *COMSOL Multiphysics 4.3b* on a commercial *SPB605060* pouch cells from *Enertech.* The cell offers a capacity of 2 A h and has an electrode size of $4.6\,\mathrm{cm} \times 5.2\,\mathrm{cm}$. Figs. 22a to 22c display the simulated temperature distribution at 100 % SOD according to cycling data from a 2C discharge. The discharge rate was chosen according to the maximum allowed discharge rate of the cell (see[90]).

The simulation studies are based on a linear interdependency of cell polarization and exchange current density as pointed out in [102] and [54] in order to estimate the temperature distribution within the electrodes [50] and, hence, the entire cell geometry [110]. The presented simulation results show that even for a comparably small cell under normal operation conditions, inhomogeneities in the temperature distribution occur. In-plane and through-plane gradients are in a similar range of 0.6 K. While the temperature gradients are clearly not as significant as in large size pouch cells or for higher C-rates, the results show a clear qualitative tendency. What is apparent from the simulation is that close to the tabs, which in this cell are placed on the bottom layer, the heat dissipation is biggest. This can also be observed when looking into the infrared images from the 40 A h pouch cell in Fig. 56.

In order to verify the findings and to see the significance of in-cell data, the experiment described in Section 6.2 is later carried out.

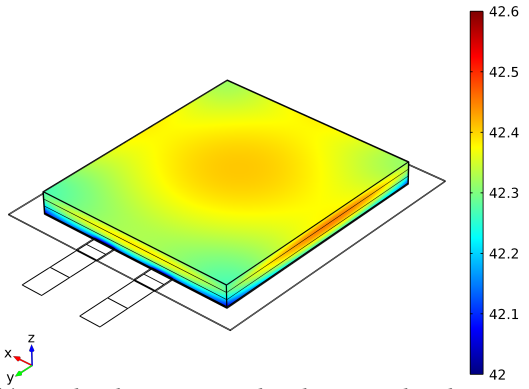

(a) Simulated temperature distribution within the entire cell stack.

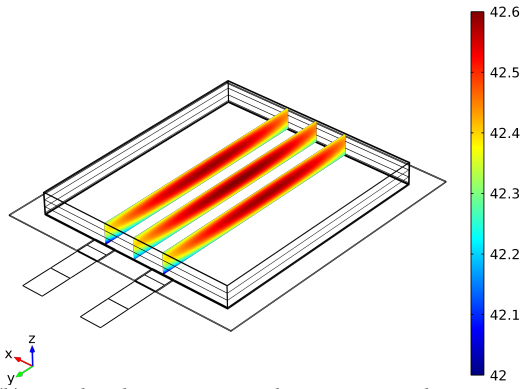

(b) Simulated cross-sectional temperature distribution within the cell stack along the tabs and within the symmetry plane (yz-plane).

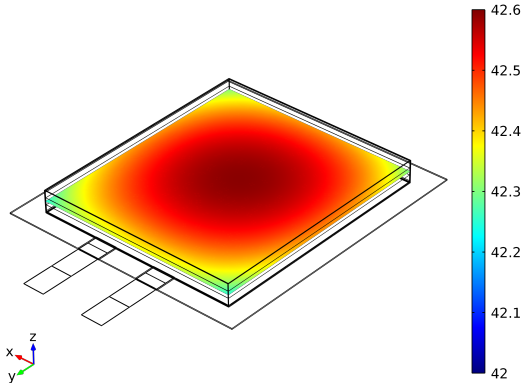

(c) Simulated temperature distribution in the middle plane (xy-plane) of the cell stack where the sensor matrix is going to be integrated.

Figure 22: Simulated temperature distribution in the *SPB605060* pouch cell with 2 Ah at a 100 % SOD at a constant discharge rate of 2C.

4.3 RELATED WORK

Due to the growing demand for Li-ion batteries and their safe and reliable operation [7, 8], the estimation of the internal temperature of Li-ion cells is a focus interest of ongoing research. Several papers use internal cell parameters like the impedance spectrum to estimate the temperature, see [93, 96]. Other research considers the integration of sensors physically into the cells [56, 57, 59, 69, 71, 76]. Both methods, however, have their specific drawbacks as outlined in the following.

While using internal parameters has the advantage of being non-invasive and in result non-influential on the cell behavior, the findings in Chapter 3 showed no suitable usage of these parameters for detection of temperature inhomogeneity and hot spots under cell operation. With the described methods, at most, an average temperature of the cell can be detected and safety hazards are hardly recognizable.

Placing physical sensors into the cells solves these problems and provides the possibility of monitoring the temperature distribution in a cell more accurately [69, 71]. Most of the present projects, however, use thermocouples for temperature measurements [59, 69, 71, 76] that require a reference temperature at the cold junction of the sensor in order to estimate absolute temperature values. A feed through the cell casing is mandatory which can lead to leakage [69–71].

In [56, 57, 70], resistance based sensors are introduced to overcome the drawbacks of requiring a reference temperature. They provide in principle the possibility of encapsulated temperature measurements in the cell if data transmission can be performed wirelessly.

[79] proposes to move the monitoring and control hardware of the lowest layer of a hierarchical battery management system closer to the cells. It is suggested that sensing elements for temperature, current, voltage, impedance and some other cell parameters along with basic cell balancing systems, data processing and the data communication system are integrated into one macro-cell. The macro-cell consists of four pouch cells, connected in series.

[63] suggests, similar to the method described in Section 4.9.2, to use a capacitive data communication for battery cell monitoring. The proposed monitoring system provides one temperature sensor, that, along with other monitoring electronics is attached to the surface of a cell. The capacitive data transmission is used to send data from each cell in a module to the common BMS. By contrast, the novelty in this chapter is that the described communication system is designed such that it can monitor multiple in-situ temperature sensors and communicate data wirelessly through the cell casing.

In [70], different methods for data transmission have been investigated without any additional wiring, showing that existing transmission systems like wireless networks, RFID or power-line communication are not applicable for Li-ion cells due to space restrictions or shielding effects of the cell casing. As potential solutions, capacitive coupling combined with frequency cross over for reading out data from multiple sensors without additional wiring has been suggested in [70]. For the detection of temperature inhomogeneities in the cell, multiple sensors distributed over the whole area are employed. Analog sine waves with a defined frequency are sent into the cell and with the help of frequency crossover, the discussed resistive temperature sensors are read out individually and simultaneously through the coupling capacitors. The setup therefore is displayed in Fig. 40 and further discussed at this point. Nevertheless, this method has its drawbacks as it is practically not implementable at a reasonable effort and costs as it is further discussed here. In the following different prototypes are described and multiple requirements therewith addressed.

4.4 PLATINUM-WIRE BASED THIN-FILM SENSOR

Platinum is a metal which is widely known to be resistant against HF. It is furthermore applied in off-the-shelf temperature sensors, since its resistance shows a linear dependency on the temperature with a positive temperature coefficient of $\alpha = 3.9825 \times 10^{-3}\,\mathrm{K}^{-1}$ in a range of 0 °C to 100 °C according to (2). This dependency can be sufficiently approximated with a second order polynomial function for higher temperatures. For temperatures below 0 °C the temperature behavior of this sensor type can be approximated with a third-order polynomial function [31]. The behavior of platinum is therefore well known and predictable. First sensor prototypes for in-situ temperature measurements are built as a prove of concept. The sensors are produced manually by winding a 10 µm platinum wire in compact meanders to obtain a PT100 sensor. (This means, the respective sensor shows an ohmic resistance of 100 Ω at 0 °C). The actual range of the resistance at 0 °C of the sensors developed in this way is between 87.3 Ω and 103.6 Ω with a temperature coefficient between $0.0038\,^{\circ}\mathrm{C}^{-1}$ and $0.0047\,^{\circ}\mathrm{C}^{-1}$. This fluctuation is casued by the scarce precision of the manual assembling process. The platinum wire is sealed between two sheets of cell-separator material and provides a sensing area of 0.5 cm × 0.5 cm. The connectors of the sensor are made with nickel tabs, like they are generally used as cathode cell-connectors. Self-made pouch cells serve as a platform for first integration tests. Fig. 23 shows the sensor and its integration in a self-made pouch cell.

Temperature tests in a climate chamber prove the proper functionality of the sensor in cell environment. Reciprocal effects from the cell on the sensor or vice versa are not detected. Detailed diagrams of these tests have been presented in [86, 87]. Long term tests could however not be performed, since the cells showed leakage after a short time. Another drawback of this system is

(a) Detail of the sensor meanders with the cell-separator as substrate and the 10 µm platinum wire

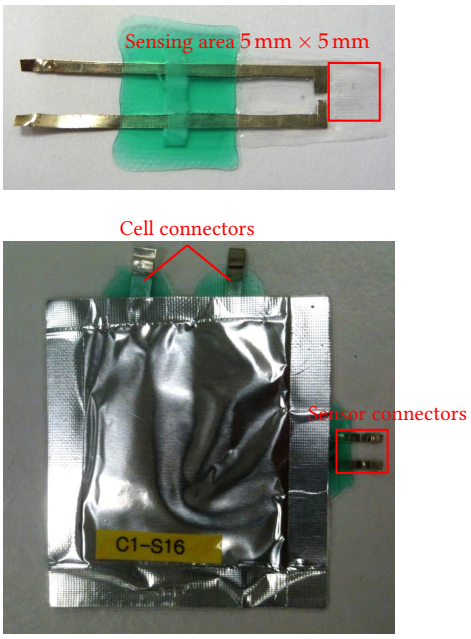

(b) Sensor with connectors sealed between sheets of cell-separator (top) and sensor integrated into a self-made pouch cell (bottom)

Figure 23: Self-made platinum wired based sensor and cell with integrated sensors.

the huge production effort and the bad reproducibility of the sensors due to the manual winding of the wire.

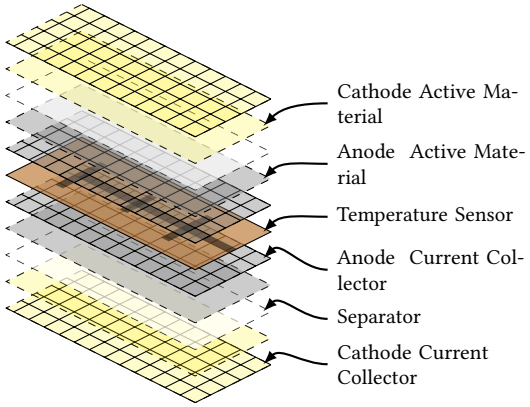

(a) Cell layers with thin-film thermocouple positioned between single-side coated anode current collectors

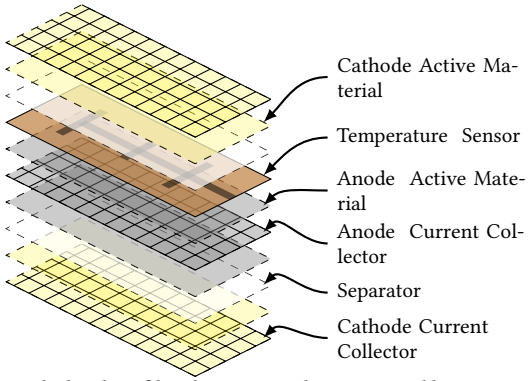

(b) Cell layers with the thin-film thermocouple positioned between anode and cathode

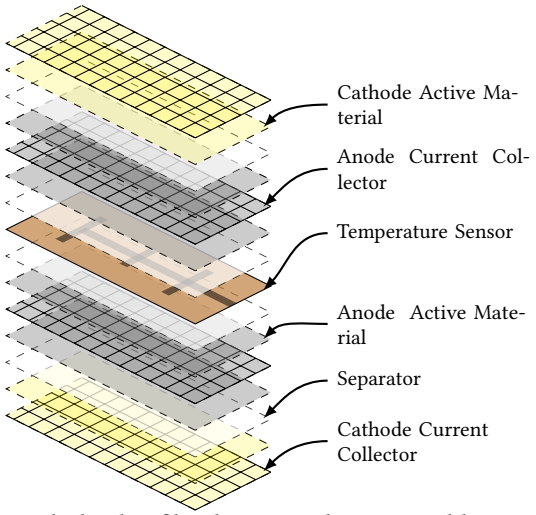

(c) Cell layers with the thin-film thermocouple positioned between two double-sided coated anodes and sheets of separator after removing the middle cathode

Figure 24: Different possibilities for sensor integration in a stack of electrodes

4.5 SENSOR POSITIONING

As mentioned before, the major criterion for the integration of sensors into a cell is to affect the behavior of the battery cell as little as possible. Aside from the above discussed shape and material requirements, the positioning plays a more critical role therefore.

If the sensor substrate does not consist of a porous material like the separator sheets applied in Section 4.4, the positioning plays a big role. Since in the following such non-permeable materials are applied, this topic is investigated in detail here. The position of the sensor needs to be chosen such that the impact on the ionic flow between active materials of anode and cathode is reduced to a minimum. Placing the sensor between a single coated, double layered current collector as shown in Fig. 24a is therefore considered to be the best solution. Since for most experiments described in this thesis, commercial cells are taken and modified, this solution is not viable. Commercial cells mostly consist of double coated electrodes for an increased energy density. This approach is chosen in the following if self-made cells are applied for the proof of concept.

Hence, the following two options for the integration remain. The first solution is to directly insert the sensor between one anode and the separator as shown in Fig. 24b, leading to a reduced ionic flow in this cell layer. It is assumed that the capacity loss due to covering the electrode area is in the same percental range as the fraction of the covered area. This means, if the sensor area covers 30 % of the area in one layer in a cell with a total of 15 double sided cathode and 16 double sided anode layers, the capacity is reduced by roughly 1.0 %. While the capacity loss is relatively small, peak currents and therewith hot spots that might lead to accelerated aging or safety issues could occur at the rim of the sensor. These influences are yet to be investigated.

Another possibility is to remove the cathode of one of the middle layers and insert the sensor between two anodes and two separators respectively. A schematic drawing of this approach is shown in Fig. 24c. The impact on the reduced cell capacity is similar to case 1, where single-sided coated anodes are employed. However, this positioning is also suitable for modified commercial cells. The advantage of this method compared to the placement between anode and cathode is that no ions flow in this layer and therewith possible peak currents on the rim of the sensor can be eliminated. The main disadvantage of this approach is a higher loss in capacity as two electrode pairs consisting of in total a double sided anode and the two single sides of the adjacent cathodes, will become inactive. The capacity loss for a cell with originally 15 layers of electrodes is therewith in the range of 6.7 %. Aside from the higher capacity loss, another disadvantage is the possible damage to other layers when removing the cathode from the assembled cell stack. For this reason the solution according to Fig. 24b is chosen for the presented proof of concept, where the sensors is inserted in a commercial cell.

To investigate the influence of a sensor between electrodes on the cell capacity better, three different types of *2016* coin cells were assembled with Lithium Cobalt diOxide (LCO) cathodes, graphite anodes and a *Celgard 2325* separator. Coin cells where chosen for these tests since they are easy to assemble on a lab scale in a reproducible way. For the investigations at hand the cell shape is irrelevant.

The chosen electrode diameter is 16 mm and the separator diameter 18 mm. 100 µL of $LiPF_6$-based liquid electrolyte in organic solvent EC:DMC:DEC (ethylene carbonate, dimethyl carbonate, diethyl carbonate) with a mixing proportion of 4:2:4 are employed. One type of coin cells is setup in the usual way with only electrodes and separator, while a second type incorporates a *Kapton 100MT* disk with the same diameter as the separator which is integrated between the electrodes. A third type is built with only half a disk - shaped like a semi-circle - of Kapton between the electrodes, covering therewith 50 % of the electrode area. While the cells with the full Kapton disk do not function due to low porosity and low Li-ion conductivity of Kapton, the other two types are cycled with 0.25 C for several cycles. By displaying the voltage as a function of SOC, Fig. 25 shows that the influence of the inserted Kapton on the cell voltage is relatively low. In contrast to that, the later discussed setup of a pouch cell with integrated sensor shows a much higher influence of the

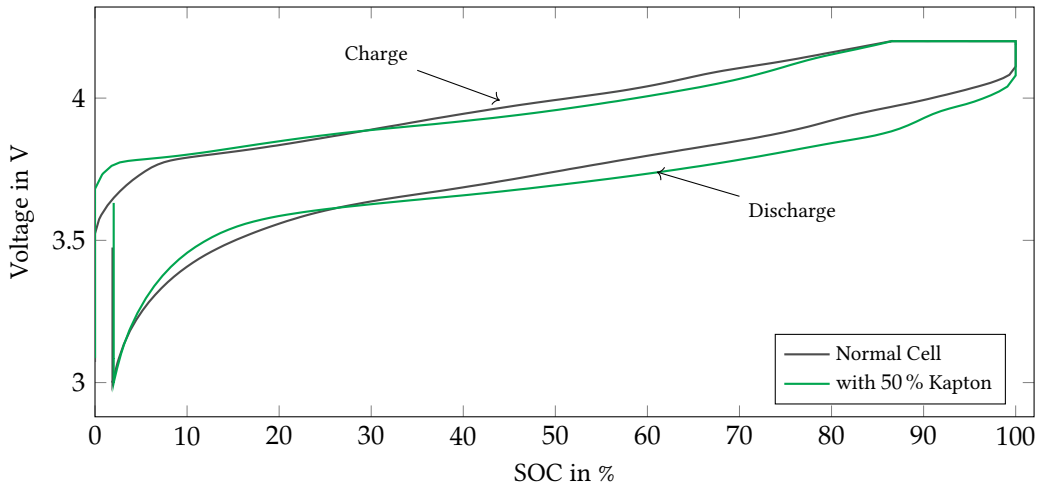

Figure 25: Comparison of Voltage over SOC for coin cells with a half Kapton disk between the electrodes and in normal setup, cycled with 0.25 C. The SOC is calculated based on the measured capacity of the coin cells, which was 4.0 mAh for the cell without Kapton and 3.85 mAh for the cell with Kapton.

sensor on the voltage drop in Fig. 35. This is probably due to the fact that the coin cell incorporates a relatively large amount of excess electrolyte that compensates part of the ionic insulation of the Kapton film. However, the voltage characteristic of the coin cell with an inserted Kapton half-disk, represented by the slopes in Fig. 25, shows bigger discrepancies in terms of non-linearity compared to the coin cell without Kapton. This is suggested to be caused by boundary effects between at the edge of the half-disk.

The thermal effects of the Kapton disk are expected to be negligibly small for the coin cell, since the produced heat in such a cell with only one electrode pair is exiguous. Additionally the chosen *Kapton 100 MT* has a thermal conductivity of 0.46 W / mK[22] which is more than 40 times higher than the thermal conductivity of the active materials of a cell (cf.[109]).

4.6 SENSOR COATED WITH PARYLENE

Sensors which are built up with cables, like standard thermocouples or PT100 sensors with connection wires, are in the following referred to as *wire-based sensors*. They have been researched in previous projects and described in [59] or [87]. In Section 4.4 this type of sensors was further mentioned. When integrating these kind of sensors into cells, they showed leakage at the sealing of the aluminum laminate casing of the pouch cell after a few days. Furthermore it is assumed that a flat film sensor, where the connection wires are built in to the sensor with thin-film technology, reduces the mechanical stress within the electrodes compared to a wire-based sensor, since irregularities in thickness can be better avoided. A further advantage of a thin-film design is that the thermal impact when including such a sensor is limited due to the relatively small thermal resistance and thermal mass of the temperature sensor. Examples for such a thin-film temperature sensor with similar design requirements are given by [3, 43, 55] for fuel cell applications and by [76] for batteries.

A simple solution that allows small measurement areas and therefore more measurement points within the area is a thermocouple matrix with a single common potential (cf. Fig. 28b). Thermocouples however can only detect relative temperature differences between the measurement point (hot junction) and the connector (cold junction) (cf. [31]). Therefore the temperature outside the cell needs to be constantly measured with a calibrated reference sensor during operation.

A first thermocouple-based solution is developed and described in [69]. Fig. 26 depicts the production process.

After taking before mentioned requirements into account, a *Kapton™100 MT* film from *Dupont* with a thickness of 25 µm is chosen as a substrate for the sensor. Thanks to its relatively high thermal conductivity amongst polymers of 0.46 W/mK[22], the influence on the effective thermal resistance of the cell can be minimized. With a glass transition temperature of almost 400 °C and no melting point, it furthermore provides an excellent stability and consequently the ability to track the temperature even under abusive scenarios.

As mentioned above, the used sensor type is a thermocouple matrix with different measurement points and a single common potential.

Looking into the thermoelectric potential of commonly used metals, also known as the Seebeck coefficient, as studied in [99], Cu and Nickel (Ni) provide a good voltage resolution with 21.5 µV/K compared to other metal pairs. Although the thin-film Seebeck coefficient is usually smaller than the bulk coefficient according to [18] and [111], the calculated thin-film coefficient according to (4) for a film thickness of 200 nm with 20.6 µV/K is close to the bulk coefficient and discrepancies are therewith considered to be negligible.

4.6.1 *Sensor Production*

The sensor production was done in collaboration with the *Chair of Technical Electronics (LTE)* at *Technical University of Munich*. For the deposition of the metal layers magnetron sputtering in Argon (Ar) atmosphere is applied. Before the deposition the base pressure of the chamber is pumped to below 5 µPa and the chamber is heated overnight to eliminate residual water molecules in the system and outgassing of the substrate. After the *Kapton MT* substrate is clean sputtered, first Ni and then Cu are sputtered to the substrate through an aluminum shadow mask. Cu provides thereby the common potential. The reason why copper is chosen for the common potential lies in the production process. The two stripes of the first (Ni) layer are used for positioning the mask for the deposition of the second layer more accurately. This would be harder if the first layer would have the shape of the common potential (see.Fig. 28).

The sequence is crucial, as Cu is much more sensitive to oxidation and a copper-oxide layer between both metals would influence the electrical contact as well as the Seebeck coefficient between both layers. The deposition of the Ni-Cu bilayers is conducted at a constant Ar flow rate of 60 sscm and a pressure of 0.4 Pa. The power density in both, Cu and Ni, targets is set to 4.4 W/cm^2. The total thickness of the metal layers has been controlled at 200 nm by using a surface profiler. A significant decrease in adhesion and an increasing susceptibility of the metal layers can be found, especially for Cu, on the Kapton substrate with an increasing layer thickness. Therefore, the thickness of 200 nm is chosen in order to optimize the adhesion between the metal layers and the *Kapton MT* substrate, as well as the flexibility and reliability of the thin-film sensor. It provides good and stable results.

Fig. 28a shows the prototype with two measurement points (circled) and a common copper potential. The total size of the sensor substrate is 2.5 cm × 6.5 cm. The width of the sputtered metal structure is 2 mm and the cross-sectional points that are circled in red in Fig. 28a have an area of 2 × 2 mm^2.

For the protective coating of the sensor, *Parylene C* from *Specialty Coating Systems* is deposited on the sensor in a Vapor Deposition Polymerization (VDP) process after the surface is treated with plasma etching. The resulting coating thickness is in the micrometer range and the overall thickness of the sensor matrix therewith less than 27 µm. As *Kapton*, *Parylene* is stable against almost all acids and provides with 35 ppm/K a similar thermal expansion coefficient as *Kapton MT*. With a melting point of 290 °C it provides good stability in the required temperature range.

For proving the concept and for investigating the influence of the sensor on the cell behavior and vice versa, different experiments are conducted. For the in-cell measurements, self-made

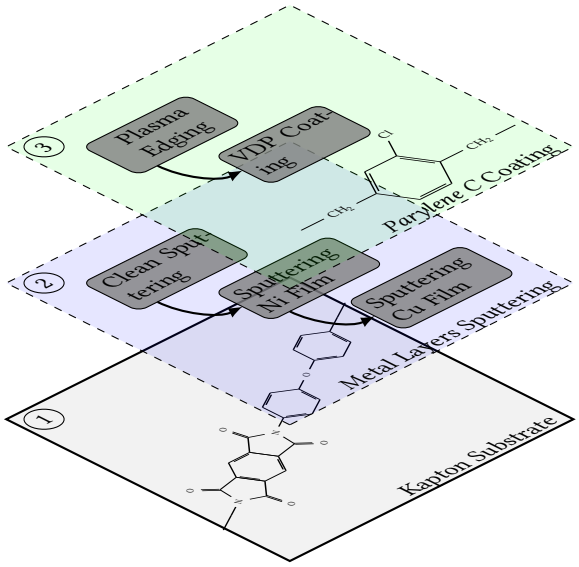

Figure 26: The production steps of the first thermocouple-based thin-film sensor from the 25 µm-thick *Kapton MT* substrate over the 200 nm metal layer sputtering to the VDP coating.

pouch bag cells with two layers of LCO cathodes and graphite anodes with an electrode area of $4\,\text{cm} \times 5\,\text{cm}$ are used. The cell had a capacity of 50 mAh. The sensor is positioned between the current collectors of single-coated anodes.

The calibration and measurement procedure is described in more detail in the following.

4.6.2 *Sensor Calibration*

The sensor calibration has been done with the coated sensor before it is integrated into the Li-ion pouch cell. The setup for calibration can be seen in Fig. 28a. The cold junction of the sensor is contacted over spring contacts to a data logger from *Agilent*. On the measurement points a Positive Temperature Coefficient (PTC) heating element is placed and heated up to 110 °C. One reference K-type thermocouple is attached to the heating element with a sticky tape while a second one is attached to the cold junction to measure the environmental temperature. The voltage of the sensor and the two temperatures of the reference thermocouples are recorded with the data logger with a sampling rate of 2 Hz. The resulting differential Seebeck coefficient of Ni vs. Cu is found to be $18.5\,\mu\text{V/K}$ and is therewith smaller than the above calculated thin-film coefficient based on Eq. (4).

The origin of the discrepancy between calculated and measured values cannot entirely be determined. 3D effects due to the surface roughness of the Kapton substrate are probably one influence that leads to a non-optimal electrical and thermal conduction between the two metal layers. Another reason might be that the calculations in (5) are based on various assumptions and may not be fully accurate.

For the required temperature range, a fifth degree polynomial function shows an accurate approximation. Fig. 27 exemplifies for one measurement point (point 2 in Fig. 28b) a temperature curve measured with a K-type thermocouple in comparison to a temperature curve calculated from the voltage values at this measurement point with a fifth degree polynomial function and a temperature curve calculated with the linear differential Seebeck coefficient $\alpha = (S_{Cu} - S_{Ni}) = 18.5\,\mu\text{V/K}$ according to (3)[31]. The polynomial function is given in (41) with the sensor spe-

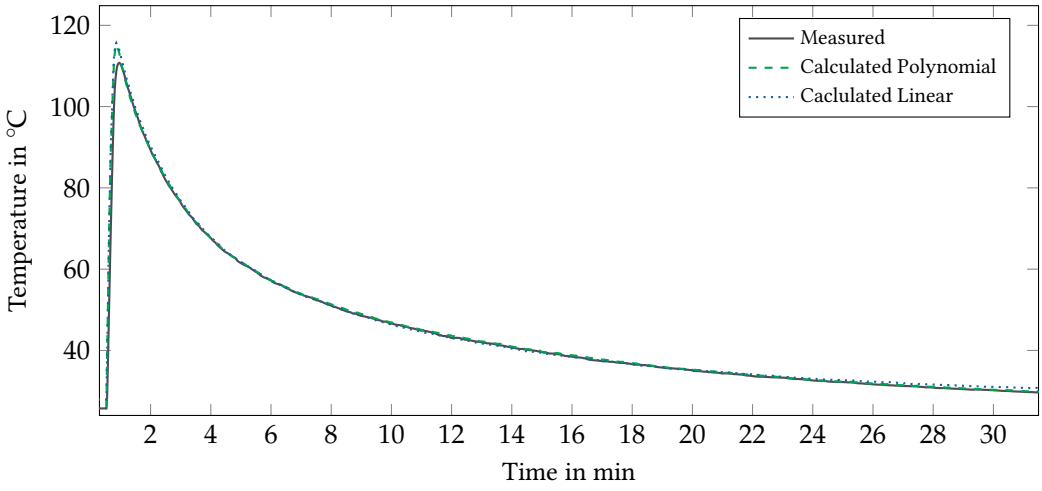

Figure 27: Temperature at a PTC heating element measured with a K-type thermocouple and calculated from the voltage values at the self-made thin-film thermocouple with a fifth degree polynomial function and the linear Seebeck coefficient

cific coefficients $A = 1.61 \times 10^{16}$, $B = -6.64 \times 10^{13}$, $C = 1.01 \times 10^{11}$, $D = -7.13 \times 10^{7}$, $E = 7.55 \times 10^{4}$ and the temperature offset $F = 26.1$.

$$T = AdV^5 + BdV^4 + CdV^3 + DdV^2 + EdV + F \tag{41}$$

Both approximations show a good agreement with the measured temperature during the cooling of the heating element and bigger discrepancies during the heating phase. This is probably attributable to the fast temperature increase at the heating element and a comparably slow response time of the data logger. An average discrepancy between calculated and measured values of 0.35 K with a standard deviation of 1.45 K for the 5th degree polynomial function and of 0.44 K with a standard deviation of 1.58 K for the linear approximation respectively is still acceptable. With slower heating rates, the accuracy of the approximation is expected to be much better.

4.6.3 *Influence of common potential and coating on temperature measurement*

In Fig. 29 voltage-over-temperature curves for the two measurement points with a common Cu potential in comparison to a coated measurement point are displayed. It shows that the coating improves linearity of the voltage-over-temperature dependence compared to the non-coated measurement points. One reason for this improvement can be a slight thermal insulation effect through the Parylene cover which decreases the thermal conduction from the heat source to the measurement points. The increased linearity is also confirmed when looking into the norm of residuals N_R, a measure for the quality of a fitting, which is used by *Matlab* and defined according to (42) with the residuals for each ith measurement point $e_i = y_{meas,i} - y_{calc,i}$.

$$N_R = \sqrt{\sum_{i=0}^{n} e_i^2} \tag{42}$$

For the linear approximation this measure for the coated sensor is with $N_{R,coat,lin} = 0.00093$ smaller than for the two uncoated measurement points where it is $N_{R,uncoat1} = 0.00122$ and $N_{R,uncoat2} = 0.00103$, respectively. Furthermore, it can be seen that the measurements on all measurement points are in good agreement. The average difference between the curves is 3.62 µV,

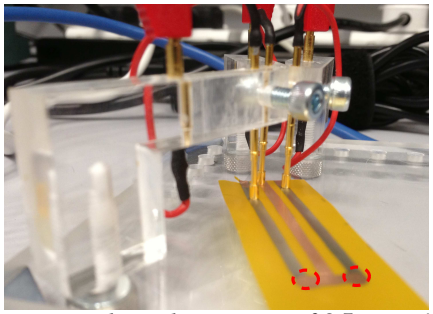

(a) Sensor matrix prototype with a substrate area of 2.5 cm × 6.5 cm, a common Cu potential in the middle and two measurement points (circled) in the calibration set-up.

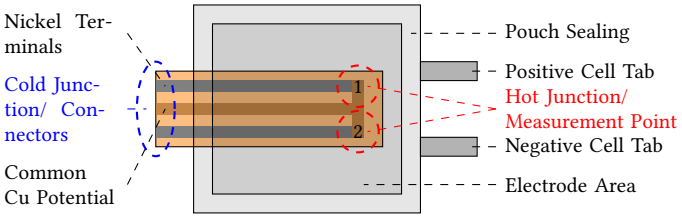

(b) Schematic setup of the prototype sensor matrix integrated in the 2 Ah pouch cell from Section 4.7 with point 1 being referred to as the left measurement point and point 2 as the right consequently.

Figure 28: Measurement setup with thermocouple matrix and the integration into a pouch cell.

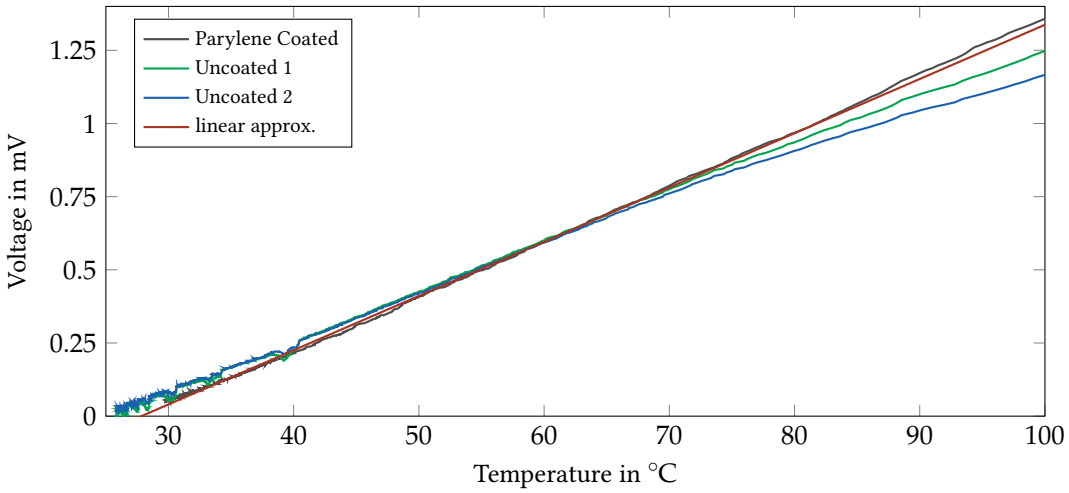

Figure 29: Voltage over temperature from a Parylene coated thermocouple with linear approximation and two uncoated thermocouples with common potential

which corresponds to 0.2 K. To see the influence of the common potential on each measurement point, further tests are conducted, where only one measurement point has been heated while the other point is left at room temperature. Reciprocal effects due to the common potential could not be observed.

4.6.4 *Stability Test*

As mentioned above, impermeability of the sensor materials is essential to avoid any interference between cell and sensor. To ensure this, the sensor has been immersed in $LiPF_6$-based liquid electrolyte in organic solvent EC:DMC:DEC with the ratio of 4:2:4 as also used above for one week and the weight, thickness and density of the sensor has been recorded before and after. No changes in these parameters could be observed.

4.6.5 *Integration Test*

The coated sensor is integrated in a lab-scale cell as described above to investigate the influence of the sensor on the cell and vise versa. The measurement points as shown in Fig. 28b were thereby inside the cell while the cold junction maintained on the outside. The sensor is sealed with the pouch of the cell to provide a tight feed through. After assembly, formation of the cell is conducted to build out the SEI and to reach a stable capacity over several cycles. Fig. 30 shows voltage over SOC of the second cycle after formation for a cell with integrated sensor in comparison to a cell without sensor. The behavior of both cells is in very good agreement.

Both cells have been cycled for ten cycles with a current of roughly 5 mA after the formation. The capacity showed a stable characteristic in both cases and an effect of the sensor on the cell could not be observed. The initial capacity of the cell without sensor was 67.06 mAh, the capacity of the cell with sensor 43.48 mAh. This is in good agreement with the earlier made assumption that the covered area relates directly to the loss in capacity. The electrode area of the used self-made cell was $4\,\text{cm} \times 5\,\text{cm}$. With the sensor having a width of 2.5 cm inserted into the cell for $1/2$ of the cell's length roughly $1/3$ of the electrode area is covered and therefore the capacity by this amount smaller.

After ten cycles the same experiment as done for calibration is repeated, but with the sensor still integrated in the cell. A significant increase in the voltage-over-temperature ratio can be observed. While the measured voltage on the sensor during calibration reaches 1.46 mV at 105 °C, the measured voltage is as high as 470 mV at the same temperature. A disassembly of the cell showed that due to the sealing of the sensor in the cell, the coating layer is damaged and massive corrosion on the copper layer took place which is probably the reason for the increased voltage. This shows again the high importance of a persistent and stable coating of the sensor.

4.6.6 *Conclusion*

A new approach for designing a thinfilm thermocouple matrix was presented. Copper and nickel as thermocouple metals show a good voltage-over-temperature dependence, even though the measured voltage was slightly smaller than the calculated thin-film coefficient. The usage of copper as a common potential for different measurement points provided very good results and a reciprocal effect between the measurement points could not be observed.

The coating of the sensor with Parylene showed an increase in linearity of the voltage-over-temperature dependence during calibration and a good stability over different measurements. The sensor has been integrated in laboratory scale pouch cells and the cell has been cycled. While no influence from the sensor on the cell could be observed, the experiments showed the necessity of an improved adhesion of the coating for further experiments to secure sensing stability also when the sensor is integrated in the cell. In further sensor prototypes, another coating solution is therefore chosen.

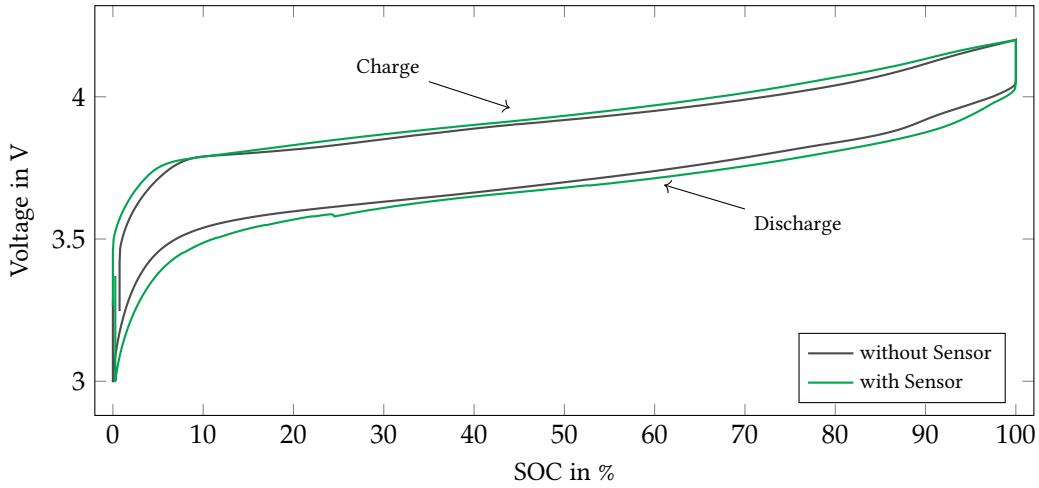

Figure 30: Voltage over State of Charge (SOC) of a cell with integrated sensor in comparison to a cell without sensor for one cycle with 5 mA (roughly C/9) cycling rate.

4.7 ALL KAPTON BASED SENSOR

In this approach, the chosen design is similar to that described in Section 4.6. The substrate *Kaptopn MT* remained the same as well as the process for the sputtering of the thermocouple. Since the *Parylene* coating showed little stability during integration, a protective layer of *Kapton MT* is selected for the following experiments instead.

For the sputtering process, all parameters were identical to the before described process. Only the film thickness of the metal layers is reduced from originally 200 nm to 120 nm in order to optimize the adhesion on the substrate. Influences on the Seebeck coefficients as described in Section 4.6.1 are assumed to be negligible according to (4) at this thickness (see Section 2.2.2). However Section 4.6.2 showed a discrepancy from the bulk coefficient due to 3D effects and surface roughness of the substrate during sputtering and the assumptions made for the calculation of the thinfilm Seebeck coefficient. Minor discrepancies are hence also expected for the here presented sensors.

In the approach described here the sensor is covered with the same *Kapton 100 MT* that has been used as a substrate for the thin-film thermocouple. Due to the increased thickness of the sensor of 54 µm compared to the one with the parylene coating (27 µm), the overall thermal conductance between the sensor and surrounding is lower. The thermal stability of the whole sensor increased significantly up to almost 400 °C thanks to the all Kapton-based design, since parylene has a lower melting point of 290 °C. Additionally, a more homogeneous setup on both sides of the sensor decreased the possibility of side-effects, such as asymmetric temperature detection, that could emerge due to different thermal conductances on each side of the sensor.

The Kapton cover has been attached to the Kapton substrate with a Kapton tape with a thickness of 25 µm. The tape was applied to all sides of the sensor and only the contacts for measuring were left free. In order to maintain the thermal conductance between sensor and surrounding, it is important not to cover the Kapton cover over the measurement points with the tape so that they are exposed to the surrounding temperature as good as possible.

4.7.1 *Sensor Calibration*

The calibration of the Kapton covered sensor is, as described before for the parylene covered sensor in Section 4.6, performed before it is integrated into a lithium ion pouch cell. The calibration setup is

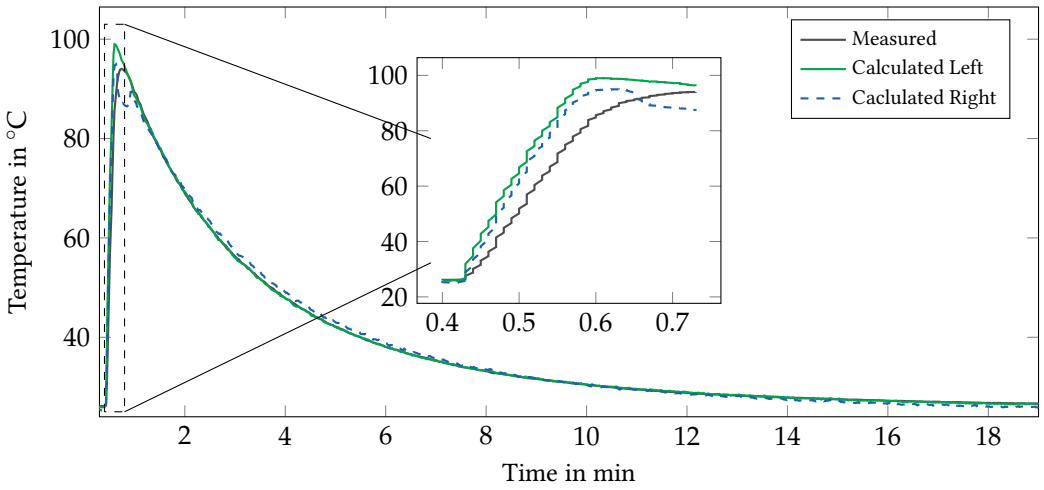

Figure 31: Temperature at a PTC heating element measured with a K-type thermocouple in comparison to the calculated temperature based on the linear Seebeck coefficient at the right and left measurement point

made identically to the one described before. The resulting differential Seebeck coefficient is again calculated as described in (2.2.2). α is thereby 8.9 µV/K for the left measurement point (number 1 in Fig. 28b) and 7.79 µV/K for the right point (number 2 in Fig. 28b) respectively, and is therewith significantly smaller than the estimated thin-film coefficient. The reason for these discrepancies that are massively bigger than in the sensor described in Section 4.6.2 can be explained with the aforementioned 3D effects due to surface roughness of the substrate which become more influential with the reduced thickness of the metal layer.

The discrepancy between the two measurement points is probably caused by variations or impurities in the production process which are inevitable on the laboratory scale.

Fig. 31 shows the temperature at both measurement points detected with a K-type thermocouple at the heating element in comparison to the temperature calculated from the voltage values at these measurement points. For the required temperature range, the linear approximation is in good accordance with the measured temperature data. The underlying Seebeck coefficients were taken according to (2.2.2).

During the heating phase this linear approximation shows slightly bigger discrepancies to the measured data compared to the consecutive cooling phase, as it has been already discussed in Section 4.6. This can be seen in the cutout of Fig. 31. Still, an average discrepancy between calculated and measured values of 0.170 K with a standard deviation of 1.488 K for the left measurement point and an average discrepancy of 0.072 K with a standard deviation of 1.408 K for the right measurement point is in a good range. This also underlines the improvement of the here described development compared to the parylene coated sensor where only an average discrepancy of 0.44 K with a standard deviation of 1.58 K could be realized.

4.7.2 *Influence of common potential and coating on temperature measurement*

Fig. 32 displays the voltage as a function of temperature for the two measurement points with a common Cu potential and a Kapton cover in comparison to the non-covered measurement points. It is apparent that due to the cover the Seebeck coefficient is slightly smaller and that the spread between the two measurement points increases. This is probably due to the unevenness of the attached Kapton tape for tightening the sensor with its Kapton cover. Additionally, since the cover is not directly connected to the sensor but a small gap exists, an increased thermal insulation between

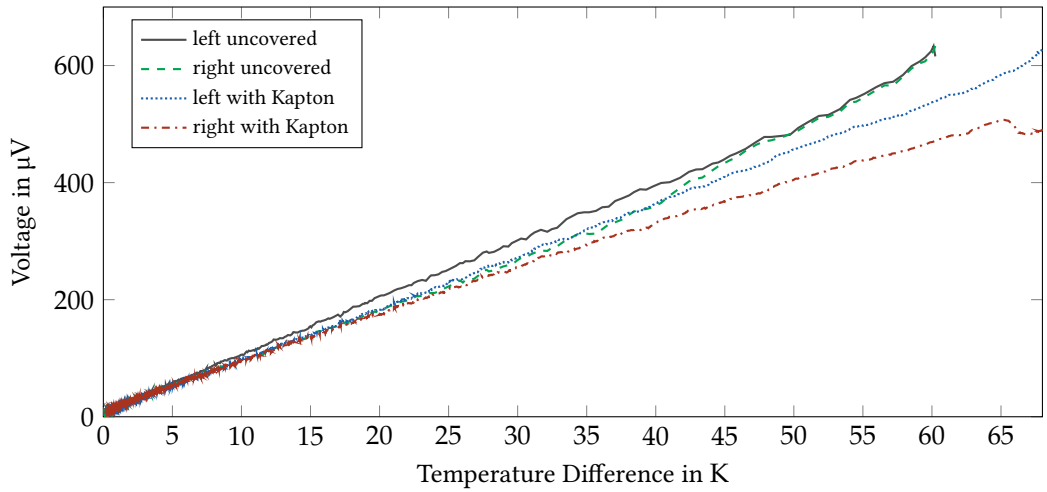

Figure 32: Voltage over temperature for two measurement points with common Cu potential in the un-covered stage and with the ready-for-integration Kapton cover

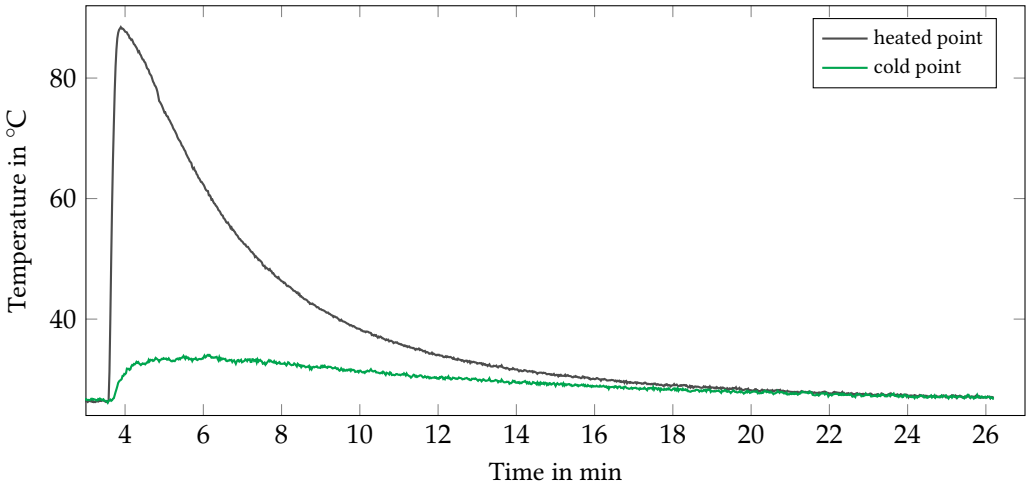

Figure 33: Temperature over time for the left heated and the right unheated measurement point from a thermocouple matrix with common Cu potential

the sensor and the surface of the cover occurs. Through that, the thermal link from the sensor to the heat source and therewith the thermal conduction to the sensing points decreases. However, when looking into the linearity of the voltage-over-temperature ratio, it has significantly increased compared to the first prototype with Parylene coating that has been described before and in [69]. This effect is probably as well due to the thermal insulation of the cover in combination with the gap between cover and sensing point. The norm of residuals according to (42) for the linear approximation of the Kapton covered sensor has been improved by 88 % in comparison to the parylene covered sensor from 0.00093 to 0.00011 for the left measurement point and by 51 % to 0.00045 for the right measurement point respectively.

Fig. 33 shows temperature data from measurements, where only one sensing point is heated and the other point is kept at room temperature. The slight increase in temperature at the beginning on the cold measurement point can be referred to unpreventable heat transfer mechanisms from the heating element to the cold measurement point. Reciprocal effects due to the common potential could not be observed.

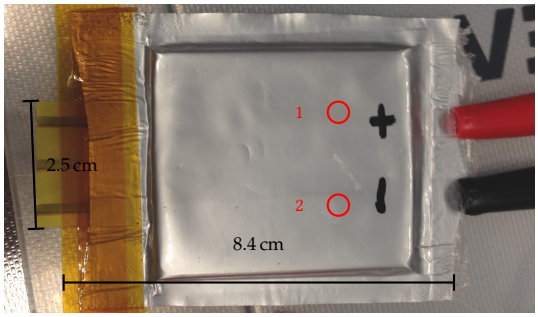

Figure 34: Cell with integrated sealed-in sensor tightened with Kapton tape on the left and the regular cell tabs on the right.

4.7.3 *Stability Test*

As mentioned above, impermeability of the sensor materials is essential to avoid any interference between cell and sensor. To ensure this, the sensor substrate together with the Kapton tape has been immersed in $LiPF_6$-based liquid electrolyte in organic solvent EC:DMC:DEC with the ratio of 4:2:4 as also used above for one week and the weight, thickness and density of the sensor has been recorded before and after that. No changes in these parameters could be observed.

4.7.4 *Integration Test*

The coated sensor is now integrated in a commercial 2 Ah-cell from *Enertech* to investigate the influence of the sensor on the cell and vice versa.

The cell is therefore opened within a glove box under Ar atmosphere by cutting the pouch bag open on the opposite side of the tabs. The sensor is then inserted for 3.5 cm into the cell between the middle pair of electrodes as shown in Fig. 28b, covering therewith an area of 3.5 cm $\times$ 2.5 cm or 43.6 % of one electrode pair, which is roughly 1.5 % of the entire electrode area. It is therewith expected that the total capacity of the cell decreases in the same percentage range.

The measurement points as shown in Fig. 28b are inside the cell while the cold junction remains on the outside. The whole cell pack is then sealed into another pouch bag with the areas near sensor interconnections additionally reinforced with Kapton tape. Fig. 34 shows the cell prepared in such manner. After assembly, the cell is cycled at low currents of 0.5 C for charging and 0.2 C for discharging respectively to prove the functionality. Fig. 35 shows the voltage as a function of SOC for the described cycle of a cell with an integrated sensor in comparison to a cell without sensor.

The behavior of both cells is in very good agreement. The capacity of the cell with the integrated sensor is 3.9 % lower than the one of the cell without a sensor and therewith larger than expected from the electrode covering. This is probably caused by the reduced physical contact between the electrodes due to the integrated sensor. It shows that the electrode layer becomes probably inactive as one electrode layer equals roughly 3.3 % of the overall cell capacity. Further losses may be attributed to electrolyte loss during assembly. Additional over-potentials and/or polarization effects emerge as a consequence of the sensor integration. This is indicated by a higher voltage profile during charge and lower voltage profile during discharge to reach the same voltage thresholds of 4.2 V as the upper cut-off limit and 3.0 V as the lower limit respectively, as displayed in Fig. 35. This further reduces the energy efficiency of the battery cell by requiring more electrical work to charge the cell, while the amount of electrical work that the cell can yield during discharge is reduced. Both cells have been cycled for 15 cycles with the above mentioned cycling rates. The capacity showed an overall stable characteristic in both cases and a further effect of the sensor on the cell could not be observed.

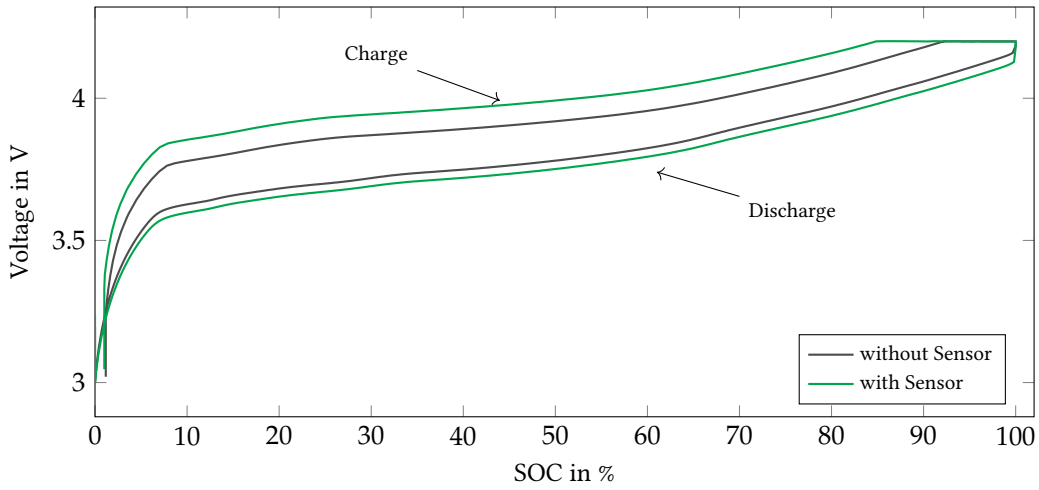

Figure 35: Voltage over SOC of a cell with integrated sensor in comparison to a cell without sensor for one cycle with 0.5C charge and 0.2C discharge rate

After five cycles the temperature measurement that has been performed for calibration is repeated with the sensor still integrated in the cell. A significant increase in the voltage-over-temperature ratio could be observed, similar to the parylene coated sensor. While the measured voltage on the sensor during calibration reached 600 µV at 95 °C, the measured voltage after cycling reached a value as high as 120 mV at 40 °C. This also resulted in unreproducible voltage over temperature data. As this behavior is similar to the behavior of the parylene coated sensor, which has been disassembled from the cell, it is assumed that a leakage in the insulating cover of the sensor is the reason. This effect is intensified through the fact that the used measurement electronic - a *34972A* datalogger from *Agilent* - is not operating potential-free for voltage measurements. A slight amount of electrolyte at the sensing metals leads to an increased electrolysis. To address this coating problem further, in the next step, a sensor built from liquid polyimide on both sides of the sensing area is developed to ensure the impermeability of the sensor.

4.7.5 *Conclusion*

The application of copper as a common potential for different measurement points provided very good results and during tests with different temperatures at each point a reciprocal effect between the measurement points could not be observed.

The coating of the sensor with Kapton showed an increase in linearity of the voltage-over-temperature dependence during calibration and a good stability during different measurements compared to the before presented approach with parylene. Due to the higher thickness of the Kapton cover, the Seebeck coefficient decreased. Measurements showed still reliable and reproducible results.

The sensor has been integrated in a commercial 2 Ah pouch cell and the cell has been cycled for 15 cycles. While no influence from the sensor on the cell could be observed, after some cycles the adhesion of the sensor cover weakened which resulted in a leakage of electrolyte. The experiments showed the necessity of an improved manufacturing process to ensure long-term sensing stability. In a next step, the sensor is built from liquid polyimide giving the possibility to integrate the metal layers directly in the substrate.

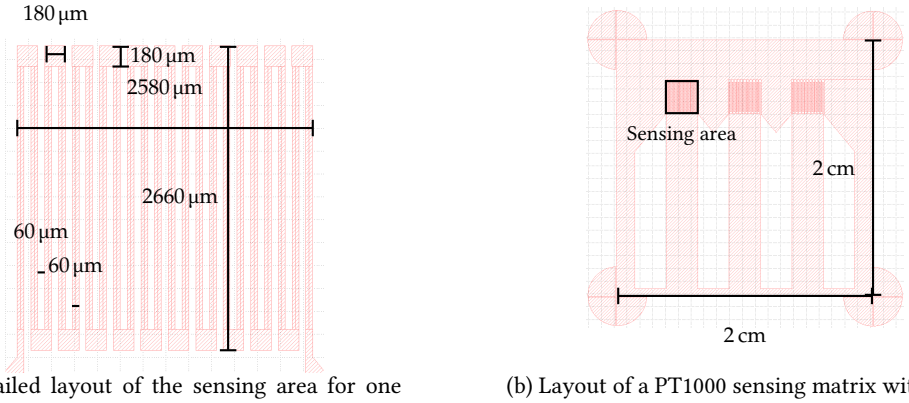

(a) Detailed layout of the sensing area for one sensing point

(b) Layout of a PT1000 sensing matrix with three measurement points

Figure 36: Mask layout for the lithographic production process for a three-measurement-point PT1000 thin-film temperature sensor.

4.8 SELF-MADE POLYIMIDE SENSOR

In order to eliminate leakage in the coating and therewith a negative influence from the electrolyte on the sensing behavior, as it is found for the previously described sensors, a method is developed to integrate the sensor in the substrate foil during the production process. A similar process is described by Pruit [82] for the production of a flexible strain gage array. In this section, the manufacturing of a *PT1000* sensor matrix, consisting of three sensing points integrated into a polyimide foil is described.

Polyimide, of which the previously used Kapton foil consists, is chosen because of its thermal stability, nonflammability and the fact that it is robust in multiple organic solvents and concentrated acids [78]. The used polyimide *PI-5878G* from *HD MicroSystems* is supplied as a polyamic acid precursor in an N-methyl-2-pyrrolidone (NMP)-based solvent. During the curing process the polyamic acid is transformed into polyimide and water is produced as a secondary product. After the curing process is concluded, the material is only soluble in 49 % HF, very strong acids and bases [42]. It is hence assumed that this material is able to persist in the given environment for a long time.

As a sensing metal, platinum is applied with the properties mentioned in Section 4.4. In order to produce *PT1000* sensors, the layout according to Fig. 36 is chosen with a layer thickness of 120 nm. Fig. 36a shows thereby a detail of the sensing area which is marked in the overall layout in Fig. 36b. This thickness provided the best results during previous tests in terms of mechanical durability.

4.8.1 *Sensor production process*

In the following the different production steps of the sensor are described. The production was done in collaboration with the *Chair of Technical Electronics (LTE)* at *Technical University of Munich*. The procedure was developed in accordance to the process described by [83]. Schematic drawings along with pictures of each steps are presented in Fig. 38.

4.8.1.1 *Wafer preparation*

As a bearing substrate for the production, a silicon wafer with 2 cm × 2 cm is used. To avoid any impurities or contaminations different cleaning steps are performed before starting the processing.

Major particles are removed with compressed nitrogen. After that, the wafer is placed into an ultrasonic bath with De-Ionized Water (DI) for 2 min, followed by 2 min DI flooding.

To eliminate organic impurities, the wafer is placed for 15 min into a rinsing solution in an ultrasonic bath at 74 °C with medium intensity. The solution consists of 6:1:1 DI:NHe=H:H_2O_2. Residuals of the solution are removed during 1 min ultrasonic bath with DI and another 2 min DI flooding.

Oxide is removed from the surface of the wafer by placing it into a plastic cup with 24 % HF for 1 min under stirring movement. To stop the etching process, the wafer is then placed into three consecutive cups with DI followed by 3 min DI flooding.

Since HF contains heavy metals that are deposited on the surface on the wafer during etching, in the next step these residuals are removed. Therefore, the wafer is placed in the ultrasonic bath for 15 min at 74 °C with medium intensity in a 42:7:1 DI:HCl:H2O2 solution. The solution is cleaned off by a 1 min ultrasonic bath in DI followed by 2 min DI flooding.

In a last step, the wafers are dried with nitrogen and on a hotplate for about 30 min.

Fig. 38a and Fig. 38b show the wafer at the end of this step.

4.8.1.2 *HSQ sacrificial layer*

Since the silicon wafer only serves as a production substrate, a sacrificial layer is applied between wafer and sensor material in order to detach the sensor. Different experiments showed that Hydrogen Silsesquioxane (HSQ) provides good results for this purpose. Since HSQ polymerizes above 5 °C and with traces of water, a quick and clean processing needs to be ensured. For this purpose, the wafers are put on a hot plate for 30 min at 200 °C to remove residual moisture. HSQ is then deposited on the wafer with a pipette until the wafer is fully covered. After 10 s resting, the wafer is spun for 30 s at 3000 rpm. The curing is performed in two steps: the first step is done for 5 min at 100 °C to evaporate carrier solvents. In the second step, the polymerization takes place during a 5 min heating at 225 °C The silicon wafer with the HSQ layer is displayed in Fig. 38c and Fig. 38d.

4.8.1.3 *Processing of polyimide*

Before application of the PI, the wafer is dehydrated for 30 min at 200 °C on a hotplate. To increase the adhesion of PI on HSQ, the surface is additionally cleaned with plasma activation. The wafers are therefore processed with 150 W for 5 min.

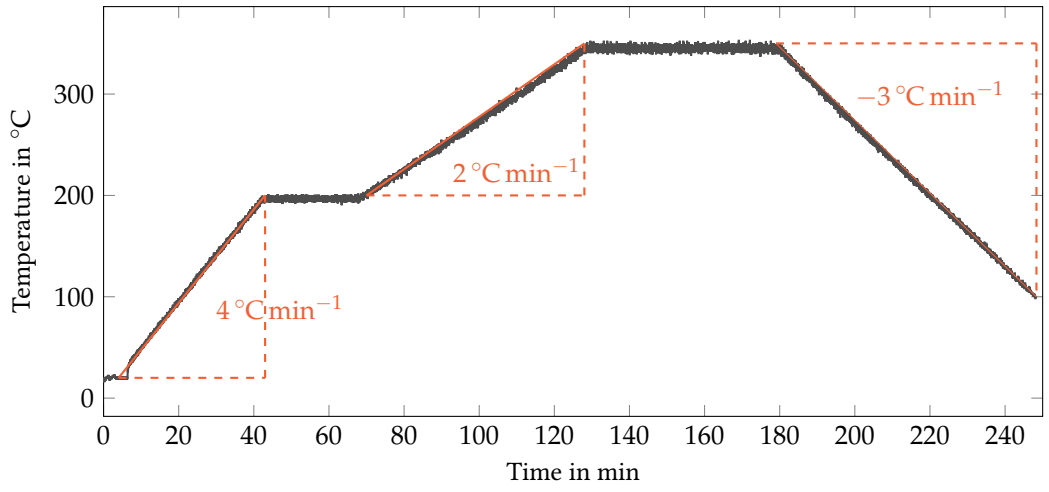

Figure 37: Curing process for the imidization of Polyimide (PI).

The polyimide is applied in three layers to gain a uniform film with the desired thickness of around 40 µm for the whole sensor. Before application of the liquid PI precursor, the surface is cleaned with nitrogen. The PI is applied with a pipette on the center of the wafer until roughly half of the diameter of the wafer is covered. The pipette is therefore placed as close as possible to the wafer to avoid air entrapment. The wafer is then spun at 15 rps for 5 s with an acceleration time of 5 s to cover the whole surface. To gain a uniform layer, it is afterwards spun with 40 rps for 30 s with an acceleration time of 3 s. A pre-bake is done on a hotplate at 135 °C for 2 min for partial polymerization and evaporation of the solvents before applying the second layer.

The second layer is applied similarly but with a dispense rate of 20 rps for 5 s and an acceleration time of 5 s followed by an increased spin rate of 45 rps for 30 s with a 3 s acceleration time. The pre-bake is done with the same parameters as before.

The dispense rate for the third layer is equal to that of the second layer followed by a 50 rps spin for 30 s. The usual pre-bake follows.

For the removal of residual solvents and in order to fully imidize the PI, it is cured in a nitrogen atmosphere with a flow rate of 260 L h^{-1}. The baking chamber with the sensor inside is therefore filled with nitrogen at room temperature and heated up to 200 °C with a heating rate of 4 °C min^{-1}. The oven is kept at this temperature for 30 min to imidize 90 % of he material. In the next step the oven is heated up to 350 °C at a rate of 2 °C min^{-1}. The film is exposed to this final temperature for 1 h to complete the imidization process. Before the sensor is removed from the chamber, cooling down to under 90 °C is performed at a 3 °C min^{-1} rate. Fig. 37 shows this process. At the end of this process step the wafer looks as depicted in Fig. 38e and Fig. 38f.

4.8.1.4 *Deposition of platinum sensor structure*

The process of depositing the platinum sensor structure onto the PI substrate consists of three steps: lithography, platinum sputtering and lift off.

For the **lithography** the PI covered Silicon (Si) wafer is first dried-out for 30 min on a hot plate at 200 °C. After nitrogen cleaning, a primer is applied on the surface and spun after 10 s drying for 30 s at 3000 rpm. Negative photo resist *ma-N 1520* from *micro resist technology* is distributed on the surface in the same way. A pre-bake follows on a hot plate at 95 °C for 120 s. After the wafer it is cooled down, the photo resist is exposed via contact exposure for 27 s to sensitize the desired structure that will be removed. It is afterwards developed in the developer *ma-D 533S* from *micro resist technology* for 65 s. The development process is stopped by dipping the wafer into DI for 30 s followed by 3 min DI flooding. The respective outcome at the end of this step is shown in Fig. 38g and Fig. 38h.

In the next step, Platinum (Pt) is **sputtered** onto the surface. To remove any undesired particles and to activate the surface, it is clean sputtered for 5 min with a working pressure of 20 µbar and a power of 100 W with an Ar flow rate of 18 sccm and plasma ignition at 20 µbar.

For the actual platinum sputtering, the plasma ignition takes place at 6 µbar and an Ar flow rate of 10 sccm. As soon as the plasma is generated, the operation pressure is reduced to 2 µbar and the power adjusted to 20 W. This ensures a sputter rate of 0.08 nm s^{-1}. To achieve the desired platinum thickness of 87.5 nm the sputtering is done for 18 min. This step is visualized in Fig. 38i and Fig. 38j.

The last step for structuring the sensor is the **lift-off**. Remaining photo resist is thereby removed by etching to gain the desired sensor structure. The etching takes places in NMP in an ultrasonic bath at 75 degrees, medium intensity level, for 5 min to 10 min. The residual NMP is afterwards removed by dipping the wafer into two consecutive cups with DI for a few seconds, followed by DI flooding for 3 min. The sensor looks after this step as depicted in Fig. 38k and Fig. 38l.

4.8.1.5 *Polyimide passivation layer*

On top of the Pt sensor structure, a passivation layer of the same PI, that has been also used as substrate is applied. In order to increase the adhesion between substrate and passivation layer, an adhesion promoter *VM651* from *HD MicroSystems* is used in a first step. The wafer together with the sensor structure is again dried at 200 °C for 30 min before plasma activation of the surface for 5 min at 150 W is performed. After the usual nitrogen cleaning, the adhesion promoter is deposited with a pipette such that the whole surface of the sensor is covered. The puddle remains for 20 s before the wafer is spun at 50 rps for 25 with an acceleration time of 10 s. A soft bake of the adhesion promoter is performed afterwards at 110 °C for 60 s.

The following PI film is created in the same way as it has been described before in Section 4.8.1.3. Only the soft-bake between each of the three layers is omitted to allow a later litographic process for the exposure of contacts. After the third layer is deposited, a soft-bake at 135 °C for 2 min is performed. Figs. 38m and 38n show the state of the end of this step. The substrate layer from Section 4.8.1.3 and the passivation layer both have a thickness of 18 µm, resulting in a total sensor thickness of 40 µm.

4.8.1.6 *Exposure of contacts*

To be able to measure the resistance of the sensor and hence the temperature, contact openings are required. Therefore, the polyimide passivation layer is structured via litography. Positive photoresist *ma-P 1225* from *micro resist technology* is used for this step. The wafer with the sensor structure must not be placed on a hot-plate to avoid polymerization of the PI. The surface is cleaned with nitrogen again and a primer is applied onto it. After 10 s rest, the primer is spun at 3000 rpm for SI30s. The photoresist is then applied and spun at 4000 rpm for 20 s. This way a resist thickness of 2 µm is achieved. Carrier solvents are removed during a 120 s bake at 100 °C. During a 25 s contact exposure, the desired structure is made sensitive to the applied developer *ma-D331*. The development requires 75 s and is stopped by dipping the wafer into DI for 30 s followed by 3 min DI flooding. As a result, the contact openings are uncovered, as depicted in Figs. 38o and 38p. The indentation in the middle of Fig. 38o shows the exposure of the contact area which is carried out in this production step. At the sides of this cross-section the final layout with the covered sensing points is visible.

4.8.1.7 *Detachment of the sensor from the silicon substrate*

In a last step, the sensor has to be detached from the silicon substrate. This can be performed in a bath with hot water since HSQ has a hydrophilic, PI a hydrophobic surface. Water can easily infringe into the structure of HSQ. The edges of the sensor are cut with a sharp knife from the substrate such that the HSQ is better exposed to the water. Nitrogen cleaning followed by 1 min DI flooding is done to remove silicon dust.

The whole structure is then placed into an ultrasonic bath at 75 °C at medium intensity. After roughly 30 min the sensor can be carefully peeled off from the bearing substrate with tweezers. The resulting sensor is shown in Figs. 38q and 38r.

4.8.2 *Measurements and evaluation*

During the production, five sensor matrices with each three measurement points according to the layout presented in Fig. 36b have been produced. For each measurement point, the resistance value at room temperature is determined. The resulting values directly after the lift-off process were lower than those received from measurements two weeks later. The resistances for the three measurement points at 21.97 °C for the left, middle and right measurement point where $R_{left} = 964.01\,\Omega$, $R_{middle} = 905.40\,\Omega$ and $R_{right} = 896.79\,\Omega$ during the first measurement and $R_{left} =$

$972.78\,\Omega$, $R_{middle} = 906.49\,\Omega$ and $R_{right} = 910.24\,\Omega$ after two weeks. The relative increase was at 0.91 % for the left, 0.12 % for the middle and 1.50 % for the right measurement point respectively. The values however remained stable thereafter.

The calibration of each measurement point on every sensor is performed by placing them into an ice bath with DI water and slowly heating it on a hot plate up to 100 °C while stirring. A commercial *PT1000* sensor served as reference. A linear and a second order polynomial approximation have been developed thereof and resistance values calculated out of the temperatures taken from the *PT1000* sensor. With this, resistance deviations of maximum 1.53 % for the linear approximation and of maximum 2.33 % for the polynomial approximation could be achieved. A linear approximation is hence considered to be suitable. The linear temperature coefficient α according to (2) is for all measurement points between $3.31 \times 10^{-3}\,\mathrm{K}^{-1}$ and $3.34 \times 10^{-3}\,\mathrm{K}^{-1}$, averaging at $3.3 \times 10^{-3}\,\mathrm{K}^{-1}$ with a standard deviation of only $0.67 \times 10^{-6}\,\mathrm{K}^{-1}$. These values are smaller than that given in literature of $3.92 \times 10^{-3}\,\mathrm{K}^{-1}$ which can be due to impurities imposed during the production process or 3D effects thanks to a non-even surface. Another effect that contributes to lower α values is the low thermal conductivity of $\lambda_{PI} = 0.361\,\mathrm{W\,m^{-1}\,K}$[39, p.787] of the PI film. With a thickness of $s_{PI} = 18\,\mu\mathrm{m}$ and a contact area of $A = 6.86\,\mathrm{mm}^2$ at each sensing point, the thermal resistance can be calculated in correspondence to (14) to $R_{\Theta,PI} = s/\lambda A = 7.27\,\mathrm{K\,W^{-1}}$. In comparison to that, the platinum sensing material has a thermal resistance of $R_{\Theta,PI} = 0.018\,\mathrm{K\,W^{-1}}$ with $\lambda_{Pt} = 0.716\,\mathrm{W\,m^{-1}\,K}$[98, p.724] and $s_{Pt} = 87.5\,\mathrm{nm}$. Hence, the thermal resistance of the PI layers is by a factor of 10 higher than that of the platinum sensor.

For testing the long-term stability of the produced sensors in electrolyte, one prototype is locked into a glass container filled with a $LiPF_6$-$1\,\mathrm{mol\,L^{-1}}$ solution in ethylene carbonate and diethyl carbonate (EC:DEC) for 14 months. The resistance values experienced a slight drift towards higher values by roughly 2 % such that at room temperature resistance values corresponding to 30 °C have been measured. This phenomenon can be explained with a slow decomposition of the platinum structure. According to (43) with the specific resistance of the material ρ , the sheet resistance R_{Sheet}, and therewith the overall resistance of the structure, increases with a decreasing thickness d of the structure.

$$R = R_{Sheet} = \frac{\rho}{d} \tag{43}$$

Another sensor is put into electrolyte and the resistance of the sensor is measured every 10 s at room temperature for one week. For this purpose an acrylic sensor holder is used for contacting purposes. A significant drift in the resistance appeared as displayed in Fig. 39. After removal of the sensor from the electrolyte, it is examined under a microscope and it is visible that the platinum at the contacts is dissolved. Additionally, the passivation layer detached from the substrate since the electrolyte dissolved the adhesion promoter that is applied during manufacturing process. The mentioned effect from Section 4.7.4 of the potential on the electrolysis of the sensing material in combination with the electrolyte adds to this dissolution of the sensing material.

A second batch of sensors with longer connections is manufactured and the adhesion promoter between sensor substrate and passivation layer omitted. However, since problems in the cooling chain of the polyimide modified the material, it combusted during the curing process. Further investigations on this sensor type could therefore not be performed.

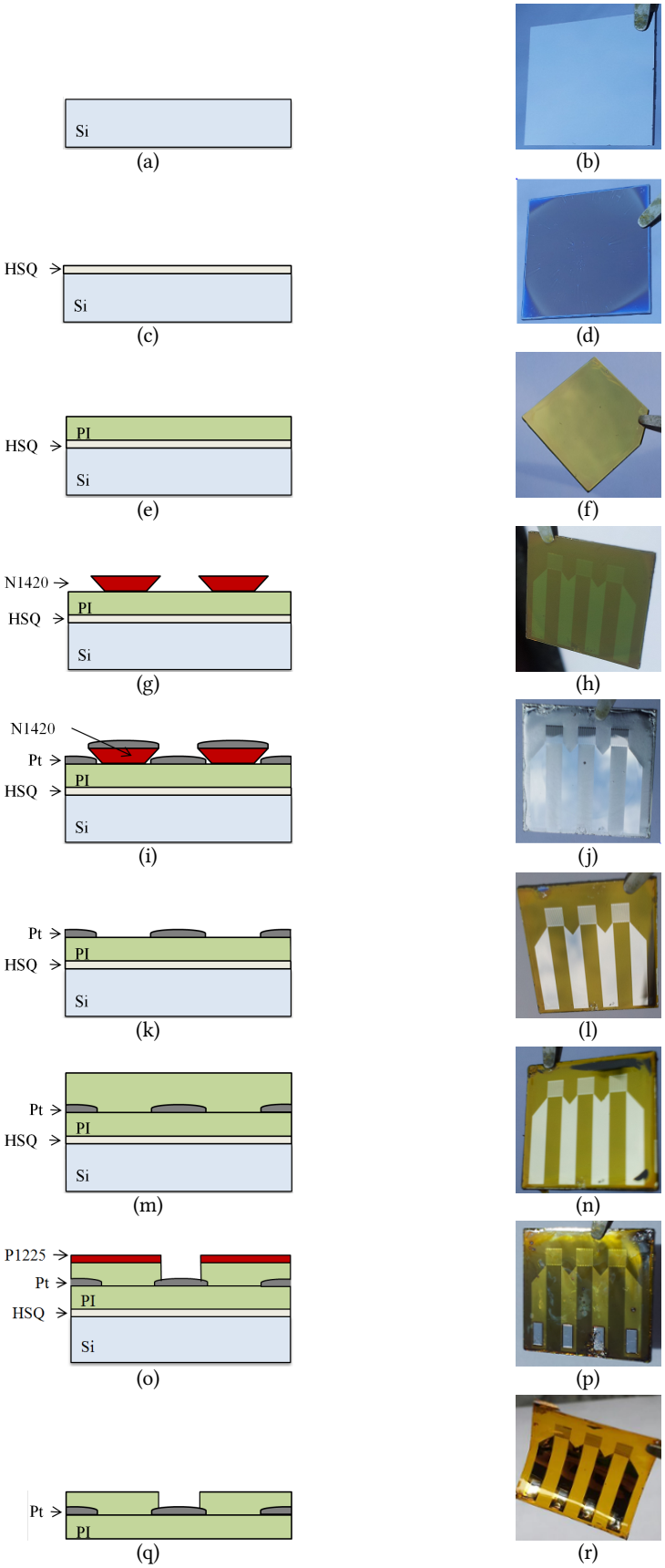

Figure 38: Production steps for the self-made polyimide-platinum sensor

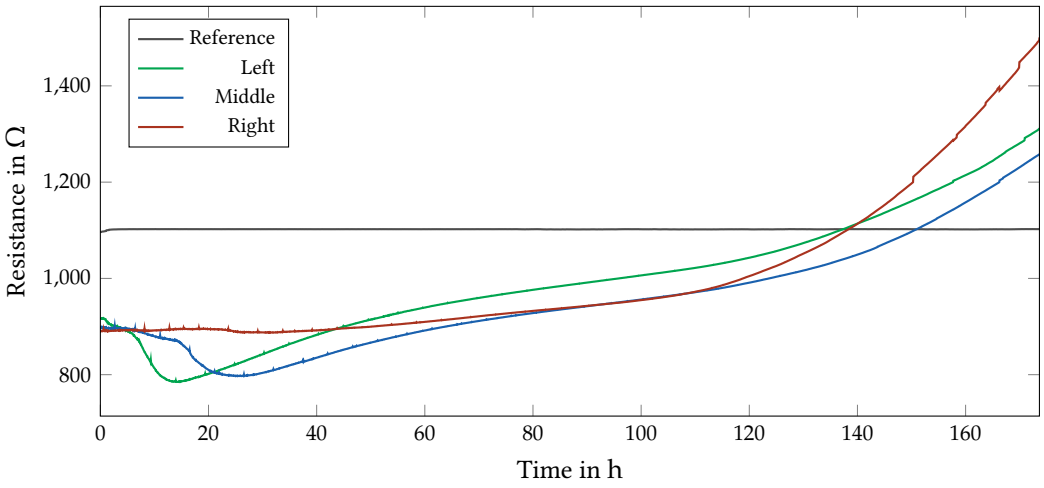

Figure 39: Resistance drift over time of a sensor in electrolyte with constant resistance measurement.

4.9 WIRELESS DATA TRANSMISSION

From above gained knowledge of sensor integration, specific requirements for data transmission evolve. The past sections showed different approaches for integrating thin-film sensors into a pouch cell. The general outcome is that the exposure of sensing material to the electrolyte has to be avoided by all means since the potential applied to the sensor by the measuring equipment leads to a fast electrolysis of the sensing material in combination with the electrolyte. In the following, wireless data transmission methods are therefore examined. They allow to produce fully integrated, fully covered sensors that operate without the necessity of a wired connection through the cell casing. This helps on one hand to get a more stable, reliable sensor and on the other hand eliminates leakage problems at the cell casing, when connecting wires of the sensor are fed through.

In a first step an analog solution is examined that researches the principle of data transmission with the help of coupling-capacitors that are placed on to the soft casing of a pouch cell. A further step describes the realization of a digital data transmission via these coupling capacitors.

4.9.1 *Analog solution*

An analog solution for transmitting data via coupling capacitors through the aluminum laminated pouch cell casing is examined. Fig. 41 shows how one capacitor plate is fixed to the aluminum laminate. The other capacitor plate is fixed to the other side of the laminate. A detailed description can be found in [70]. The system is displayed in Fig. 40. The sine wave generator module *AD9850* from *Analog Devices* creates defined sine waves at varying frequencies which are especially designated to one out of n resistive sensors $R_{meas,i}$ in the cell. The sine wave is sent with a first coupling capacitor (between point A and B) at one side of the cell stack through the aluminum laminate casing. In the cell, different band passes, also referred to as frequency crossover, filter and separate the frequencies created by the sine wave generator and by this the designated resistive sensor is addressed. The sine wave is altered through the resistive temperature sensor depending on the measured temperature and sent out through the cell casing via a second coupling capacitor (between point D and E). At the outside Root Mean Square (RMS) measurement takes place that analyses the signal change compared to the original sent-in signal and determines the measured resistance out of that. A big advantage of this solution is that no active powering of the internal electronic circuit is needed and the cell remains therefore unaffected from any parasitic power consumption through the measurement system.

Drawbacks that emerge for its practical implementation are however discussed in the following.

For investigating the signal's quality over the different branches of the frequency crossover, voltage measurements between X_i and E and between D and E according to Fig. 40 have been performed on a system which has not yet been integrated into a cell but only consisted of the

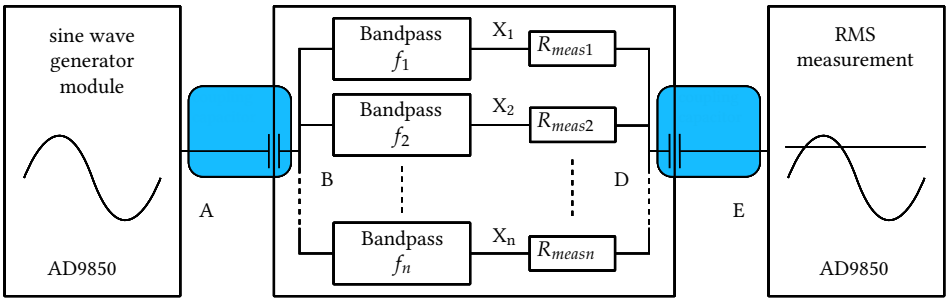

Figure 40: Setup of the analog system as proposed and simulated in [70] and realized here for suitability studies.

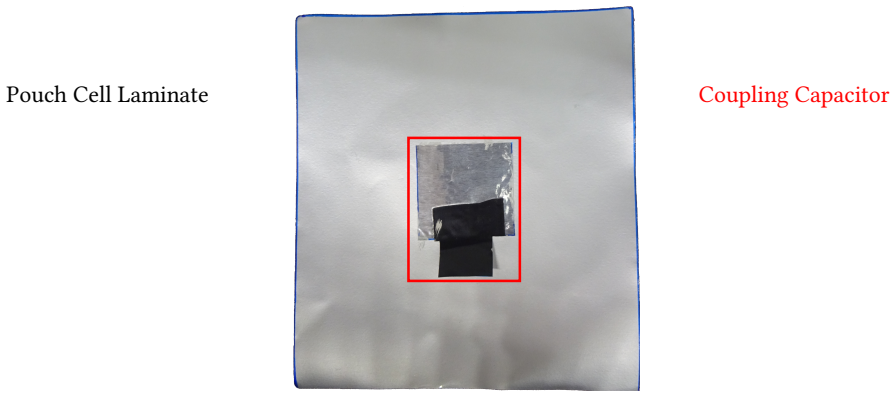

Figure 41: One coupling capacitor plate fixed to the outside of a laminated pouch casing.

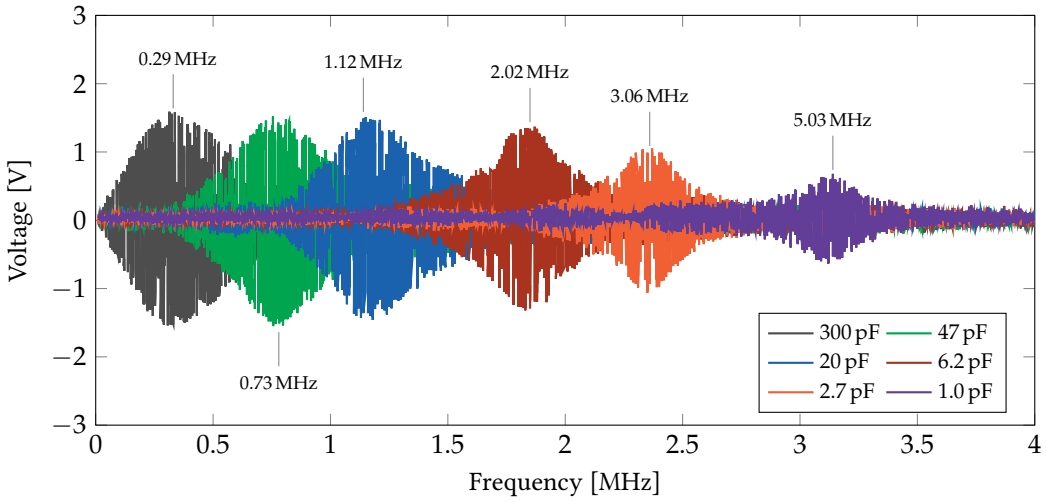

Figure 42: Measured frequency values over the different measurement resistors - from point X_i to point D in Fig. 40. The annotated values (in Mhz) depict the corresponding calculated values for fixed value resistors. The capacitances in the legend are the capacitances of the band pass filteres that filter the desired sine wave signal from the sine wave generator.

measurement setup with fixed value resistors and with sheets of aluminum laminate between the coupling capacitor's plates. The research here focuses only on the quality of the data transmission method and does not take temperature dependencies into account.

The voltage is measured between each point X_i and point E as well as between point D and E from Fig. 40. The resulting difference $V_{(X_i-E)} - V_{(D-E)}$ shows the fraction of the signal that is transmitted over a certain measurement resistor. It is displayed in Fig. 42. The peak values of each signal are in this picture compared to the expected values. The capacitors of the bandpass filters are designed such that a desired frequency range is left through. To dimension the system properly, the resulting frequencies that can be achieved with the respective bandpasses and the measurement resistor have been calculated. The annotated values in the diagram show the corresponding calculated values for the setup in comparison to the frequencies that are measured with the system - the peak values for each frequency are decisive.

It can be seen that for low frequencies, the measured values are in good accordance while for higher frequencies the measured values are much lower than the calculated values. For the sixth

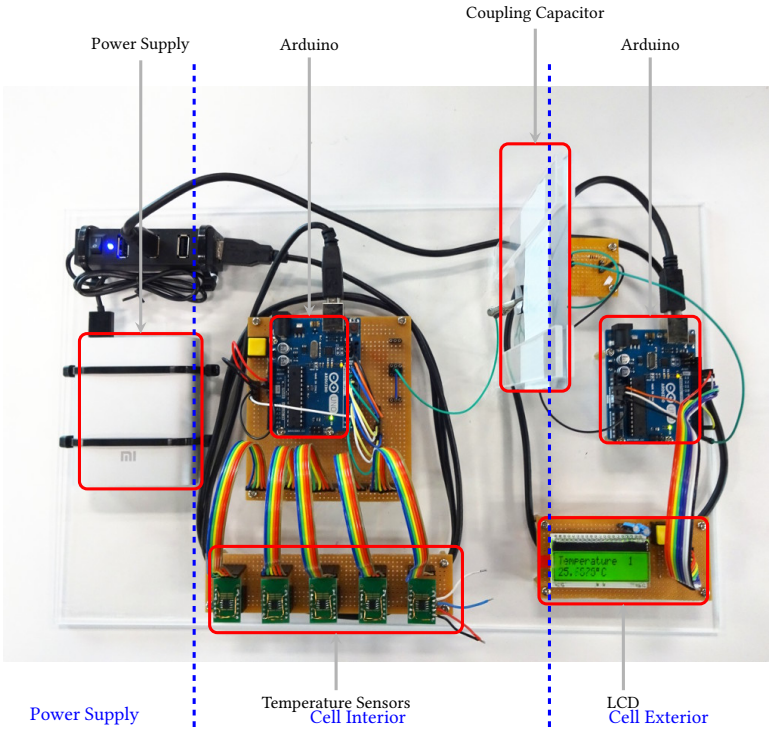

Figure 43: Conceptual hardware setup for digital data transmission through an aluminum laminate.

branch, the difference between the calculated value $f_{calc} = 5.03\,\text{MHz}$ and the measured value is in the range of 2 MHz. This can be probably attributed to parasitic capacitances in the setup.

Another significant finding when looking into Fig. 42 is the reduced signal amplitude with higher frequencies while the spread is wider. As a result, for higher frequencies the distinction between the different branches is almost impossible, since the measurement signal of one branch and the noise of the other branches show a similar amplitude. Consequently, for encountering the overlap of signals, the frequency range would need to be extended to even higher frequencies which brings in more drawbacks. With the given setup, only a limited amount of temperature signals can be transmitted. Without an overlapping of the measured frequencies, only three signals can be separated reasonably. For space-resolved temperature measurements this is not sufficient. The results show clearly that the analog method is therefore not suitable, resulting in the demand for the development of a fully digitized solution.

4.9.2 *Digitized solution*

Parts of this section have been published in [72]. Due to the mentioned limitations in the analog solution for space resolved in-situ measurement, a digital solution that can be integrated into a cell is developed. As proof of concept and to test the communication, a conceptual hardware setup is built with standard components. With this setup, schemes for transmitting the measured data through the pouch cell laminate are investigated. Coupling capacitors as used in the analog solution from [70] and Section 4.9.1 are applied for the data transmission through the cell casing.

4.9.2.1 *Setup*

The hardware setup consists of four parts that are further described in the following and outlined in Fig. 43: the power supply, the cell interior, the coupling capacitor, and the cell exterior.

Power supply: The power is supplied by a power bank, based on Li-ion cells, that provides up to 2.1 A output current and 5 V output voltage via a Universal Serial Bus (USB) plug. A USB-hub distributes the power for the interior and exterior part of the setup. In later implementations, this part can be omitted as the required power can be directly obtained from the cell at which the system is integrated.
Cell Interior: The interior is the part that for the actual implementation shall be integrated into the battery cell. Five integrated temperature sensors *ADT7310* from *Analog Devices* are used to provide distributed temperature data. The temperature sensors are connected via a Serial Peripheral Interface (SPI) to a *Arduino Uno R3* microcontroller board with an *ATmega328P* microcontroller from *Atmel*. The *Arduino* provides all required connectors. A switch for the manual selection of different program modes is added.
Coupling Capacitor: Between the interior and exterior, a mount for an aluminum laminate sheet is used which represents the battery cell casing. Capacitors of different sizes can be attached to the sheet for investigating sizing effects on the data transmission. On each side of the sheet one capacitor plate made of aluminum foil is glued to the laminate.
Cell Exterior: A 1 kΩ-resistor is connected to the exterior capacitor plate which provides two functions: On one hand, it serves as part of a voltage divider - the other part of the divider is integrated in the *Arduino* microcontroller board - to pull the signal to a desired reference level. On the other hand, this resistor is necessary to create a voltage change over the resistor out of the received current. A second *Arduino Uno R3* microcontroller board receives and processes the data and displays the values accordingly on the display on the right lower corner of the setup.
Temperature Sensor Communication: The five *ADT7310* are communicating with the microcontroller over a SPI interface. All sensors are connected via three common data lines (SCLK, MISO, MOSI) to the micro controller to provide clock signals and receive and send information. The third line of the SPI interface is used for the Chip Select (CSi) signal which is transmitted for each sensor via a separate line. With this signal the microcontroller, which acts as master, selects the sensor (slave) it wants to communicate to. Only the selected sensor reacts to information sent from the microcontroller over the MOSI line and sends data towards the microcontroller over the MISO line. After the microcontroller received the temperature value from each sensor it is transmitted to the receiver at the cell exterior. Each temperature bit string is transformed into a decimal number and the temperature is calculated based on (44) for positive temperature values and (45) for negative temperatures.

$$T_{pos} = \frac{dec(T_{binary})}{128} \tag{44}$$

$$T_{neg} = \frac{dec(T_{binary}) - 65.536}{128} \tag{45}$$

4.9.2.2 *Data transmission through the coupling capacitor*

The data transmission through the coupling capacitors is implemented using the Universal Asynchronous Receiver Transmitter (UART) standard. This method is chosen since it is a well established data communication protocol that provides a stable data transmission with little likelihood of errors.

One transmitted data set consists of one start byte, two data bytes per temperature sensor and two Cyclic Redundancy Check (CRC) bytes. As in the current setup, five temperature sensors are used, the data set has 13 bytes.

The start byte is chosen such that it is a unique binary sequence that does not correspond to any possible measured temperature value. It is set to 10101010, which corresponds to −172 °C and is outside the temperature range of the applied temperature sensors.

The CRC check sum is calculated individually for each data set by dividing the data bits by a polynomial that is known to both, transmitter and receiver, and comparing the rest. Even small changes in the transmitted data string lead thus to discrepancies in the CRC and provide a simple and reliable error detection.

In case that the start bit sequence of the start byte appears within the normally transmitted temperature values and hence is mistaken to be the start byte, the CRC returns "wrong" and the readout of the received data continues. Only if the start byte and the check sum are correct, the data string is detected as correct and further processed.

With the given setup, a much more stable data transmission than it is described in Section 4.9.1 and [70] is realized. This is mainly due to the fact that all data are transmitted digitally and errors are therefore almost omitted.

4.9.2.3 *Integration*

The development platform setup presented in this thesis is a proof of concept for the proposed data transmission scheme, using standard components. For integration into a cell, different considerations regarding size adjustments, energy consumption but also the performance of the system have to be made that are addressed in the following.

4.9.2.4 *Latency of the System*

One major reason why in-situ temperature measurement is desired is the faster detection time in case of failures compared to measurements on the cell [71]. Reactions in the worst case situation of a thermal runaway can happen fast and may not be detectable on the cell's surface within a timescale that allows to shut off the cell before serious damage to the surroundings occurs. Feng et al. show in [29] that the stage leading to a thermal runaway in a quasi-adiabatic environment during ARC takes roughly 50 s when an internal short circuit is present and the cell heating starts at room temperature. Within this stage, the capacity fades due to elevated temperatures and deintercalation of Li-ions from the anode takes place. After this stage the separator starts to melt and micro short circuits start to evolve. Closer to the separator break up, which is considered the point of no return, the velocity of heating increases. When failures are detected within the first stage, it is likely that a thermal runaway and therewith fire or explosion can be prevent with appropriate counter-measures. For the sensing system this means that temperature inhomogeneities need to be monitored continuously to detect failures like an internal short circuit before the 50 s have passed. This means that at least every second, the full set of temperature data has to be available. The optimum would be faster than that. The applied *ADT7310* sensor offers a low-power sampling rate of 1 sample/per/second. In the normal mode the sampling time is by orders of magnitude higher as it can be seen in Fig. 44.

For evaluating the time that one measurement requires with the current implementation, an experiment has been conducted where a button press triggers the system to wake up and start a measurement, which is captured with a scope. The signal curves for a symbol rate of 2 000 000 bd are shown in Fig. 44.

After receiving data from the sensors ($\overline{CS_i}$), the microcontroller requires a short period for calculating the CRC. This phase is between *Start CRC-16* and *Start UART* in Fig. 44. When the CRC calculation is done, the data are sent via the UART interface to the outside.

It is possible to reduce the duration of the SPI communication between sensors and controller ($\overline{CS_i}$). The minimum clock duration can be calculated by adding the different minimum time parameters of the SPI communication, which are given in the data sheet of the *ADT7310* [4]. It sums up to a total of 210 ns. The used default clock speed is set to 4 MHz in the library for the serial communication of the *Arduino*. This corresponds to a duration of 250 ns. As this influences the latency only marginally but makes the communication more error-prone, it is recommended not to change the clock speed.

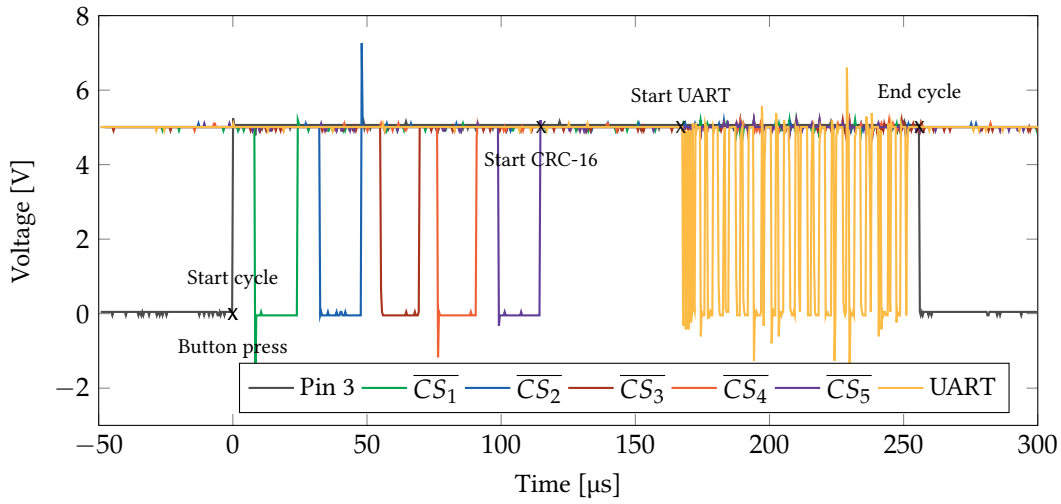

Figure 44: Latency of the measurement with five sensors and communication at 2 000 000 bd. CSi is the chip select signal for each of the integrated sensors and corresponding time for each CSi is the time, one temperature measurement requires including MOSI and MISO communication between microcontroller and sensor.

Table 4: Duration for the transfer of one bit at different baud rates and transmission time for a temperature measurement message containing 5 temperature values resulting in 130 bit in total.

Baud Rate [bd]	Duration per Bit	Duration for message
9,600	104 µs	13.52 ms
750,000	1.33 µs	172.9 µs
2,000,000	500.0 ns	78 µs

In Fig. 44 it can be seen that the calculation of the CRC-16 check sum requires 55 µs. In Fig. 44 this is the idle time between *Start CRC-16* and *Start UART*. However, the CRC-16 calculation could also be done in hardware. Since using a hardware module needs just 1 cycle per bit, the CRC-16 calculation time could be reduced to 6.875 µs for a 16 MHz controller. Further time saving can be achieved by performing the CRC-16 calculation during the transmission of the first values.

Different to the CRC-16 computation where the latency can be decreased by changing the system structure, the time for UART communication can be influenced by simply increasing the baud rate for the serial communication.

Table 4 shows the duration of the UART block from Fig. 44 for a single bit and a complete temperature message for different transmission rates.

With the above calculations, a total time for one measurement of 250 µs is estimated for the presented setup. Consequently, with 2 000 000 bd, up to 4000 measurements per second can be made. Depending on the current temperature and the load, the BMS has to decide how often it acquires the temperature values.

4.9.2.5 *Energy Consumption*

To estimate the energy consumption of the system, two different states have to be considered: the idle state and the active state.

The idle state is the state when the cell is not in use and thus the battery management system is inactive. During this time the system consumes practically no energy and only contributes with very small leak currents of the power supply module presumably in the µA-range to the self-discharge of the cell.

The active state is the state when the system is powered up, conducting a measurement and sending the values to the outside. During this time, the system has to be supplied by the power module. The energy consumption is thereby proportional to the sampling rate with a frequency dependent current I_f and a frequency-independent current I_0 according to (46).

$$I_{tot} = I_f + I_0 \tag{46}$$

The described hardware setup is powered with 5 V and not yet optimized for low power applications in the battery voltage range of 2.7 V to 4.2 V. It is therefore assumed that in a later application using a dedicated low-power System-on-Chip implementation, the energy consumption will be orders of magnitude lower than the currently consumed 100 mW under full load.

4.9.2.6 *Miniaturization*

As mentioned above, the presented hardware setup consists of standard components to test the data communication principle. For an integration into a cell, the system needs to be miniaturized. In the following, it is discussed which parts of the hardware setup are necessary for a future system. In a next step, a solution for the miniaturization of the required components is proposed.

Fig. 45 shows the modules that need to be integrated into the cell. The external control unit starts the system by sending an enable signal to the integrated DC/DC converter through the coupling capacitor. The DC/DC converter then starts supplying the system. The DC/DC converter can be designed such that it operates in the full voltage range of a cell from 2.7 V to 4.2 V with some buffer in both directions to also be able to operate in case of over-charging or deep-discharging. Whether a DC/DC converter is actually required is determined by the Application-Specific Integrated Circuit (ASIC) implementation used for the computational part of the system. The sensors 1 to 5 start measuring and the control unit reads out every sensor once. As soon as it has received the value of each sensor, it sends the data together with the calculated CRC-16 check sum through the coupling capacitor to the external control unit. After all data are sent, the internal control unit powers itself down by switching the DC/DC converter in the sleep mode for saving energy. As the external control unit is integrated in a BMS that already performs voltage sensing, access to the battery terminals is given and hence they can be used as reference points for the power supply.

The coupling capacitor is not further mentioned in this part since it is realized through a thin aluminum foil layer fixed to the pouch cell laminate and thus it does not contribute to the integrated circuits which have to be minimized in size.

FREQUENCY GENERATION As part of the control unit, a frequency generation unit is necessary. Most of the established microcontrollers have an integrated clock generation module. This is however strongly dependent on the temperature, while a crystal shows just very small dependencies on the temperature. Since the temperature inside the cell varies strongly during the operation of the system, a temperature independent clock generation unit is necessary. Thus for the considered system, a crystal oscillator is suggested. The size of this component varies depending on its frequency and is usually in the range of a few mm^2.

CONTROLLER While the microcontroller *ATmega168A* used in the development platform is already very small, most of its functions are unused in this application. For the development of a specific ASIC as a System on Chip (SoC), it is necessary to know the actual tasks of the control unit. Three main tasks have to be performed: acquiring the data from the sensors, calculation of the CRC-16 check sum and the transmission of data through the asynchronous serial interface.

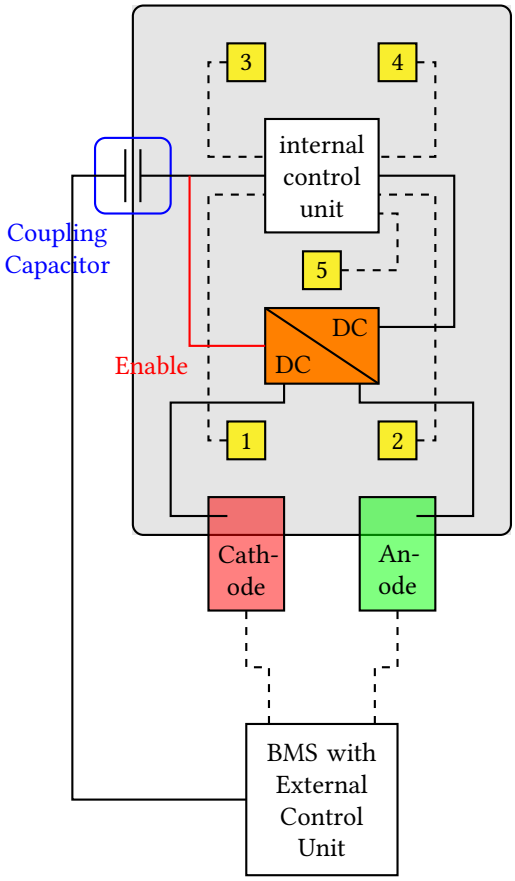

Figure 45: System setup as it can be integrated in one cell with five temperature sensors (1-5) and power supply directly from the cell.

Further functionalities other than temperature sensing could be added in a later stage. This could include for instance cell voltage measurement, pressure detection or the calculation of temperature changes over time.

For acquiring the data from the sensors, a certain request sequence has to be sent as shown in Fig. 44. This is a fixed process which can be implemented as a static logic circuit. The calculation of the CRC-16 is discussed in Section 4.9.2 and it is shown that this calculation is even faster if it is made by a hardware realization with a simple shift register and XOR gates.

Finally, the data has to be transmitted to the external control unit over the serial interface. Therefore, a clock signal is necessary on whose edges the bits are shifted out. There are no computational costs for this process which can be performed with appropriate logic. Thus, the control unit to be designed does not necessarily require a processor and could be realized with fixed logic gates, mostly representing shift registers. Consequently, the logic circuitry comprising less than 10000 transistors can be implemented as a very efficient and cheap ASIC. The footprint of such an ASIC could be in the range of a $2\,\mathrm{mm} \times 3\,\mathrm{mm}$ 6-lead plastic Dual-Flat No-Leads (DFN) package with a power consumption in the µW range.

SENSORS For further miniaturization of the sensors, a closer look at the interior of the temperature sensor *ADT7310* is taken. *Analog Devices* provides the *ADT7312*, a temperature sensor in die form. It is the same die which is also integrated in the *ADT7310* that is used in the hardware setup of this work [5].

It has a thickness of 0.092 µm. As a die has no protective coating, a protective layer needs to be added before it can be integrated into the cell. An appropriate material has to be found as it has to conduct the heat very well and has to be inert in the cell's environment.

Compared to the *ADT7310* sensor used in the development setup, a solution with less cables is given by the *DS18B20* from *Maxim Integrated*. This sensor requires only one data and an additional ground line. It communicates with the microcontroller through this data line and receives power from the same line. It also has additional features like a CRC-8 generator for calculating a check sum to ensure a reliable communication to the microcontroller. Yet the sensor is only available in relatively big packages and thus has to be put into a smaller package for an integration into the cell. The usability in the cell environment is yet to be proven. For a later integration, a minimized custom solution that is optimized for the usage in the cell environment and at cell voltage will provide a suitable solution.

POWER SUPPLY In an ASIC solution, the DC/DC converter for the power supply can either be integrated into the chip or completely avoided if the ASIC is desigend such that it can cope with the available variable battery cell power between 2.7 V and 4.2 V.

4.9.2.7 *Costs*

The protoype presented in this paper with its two *Arduino Uno R3* boards, the power bank, some smaller electronic parts and five sensors sums up to a total cost of around 100 USD. With the proposed custom ASIC solution, the costs for the whole system can be reduced to less than 1 USD per chip when mass-produced. If mentioned additional functionalities like cell voltage measurement or pressure detection are added, the costs rise only marginally. Consequently, the described system provides a cost-efficient solution.

4.9.3 *Experimental Validation*

To research the communication through the pouch cell laminate in detail, the signal before and after the coupling capacitor is measured with a *PicoScope 2205* from *Pico Technology*. One byte is transmitted from the sending *Arduino* through the pouch cell laminate. For having a highest possible bit change, the binary value 01010101 (0x55) is chosen. As the least significant bit is transferred first in the UART communication, a high edge is transmitted directly after the low START bit. At every following bit, the signal level changes until the high STOP bit is achieved after 8 data bits. With the help of these tests, the influence of different coupling capacitor sizes, the type of adhesive for attaching the capacitor plates to the aluminum laminate and the influence of different baud rates, are evaluated. In the following, output signal refers to pin TX from the sending *Arduino* and input signal to the signal at the pin RX of the receiving *Arduino*. Thus the output signal is the signal before the coupling capacitor.

For detecting the transferred values, each bit is sampled three times in the middle. However, the signal after the coupling capacitor consists of mainly peaks at the rising edge followed by a fast decline (see Fig. 46) which would make a signal detection in the middle impossible. To face this issue, the microcontroller has a Schmitt trigger integrated. Since an inverting Schmitt trigger allows a higher input resistance than a non-inverting Schmitt trigger, the former one is used in most applications. At the input of the Schmitt trigger, the signal is pulled to the reference voltage $V_{add} = 2.5\,\mathrm{V}$ by using a pull up resistor of 1 kΩ.

The trigger reacts only if the input signal surpasses the reference voltage V_{add} in one defined direction. As an inverting trigger is used, the trigger's output is set to LOW as long as the input signal is above V_{add}. Once the signal falls below V_{add}, the trigger changes its state and sets the output signal to HIGH. With this method, the microcontroller generates square waves out of the peak signals that are received on the other side of the coupling capacitor. By setting the threshold

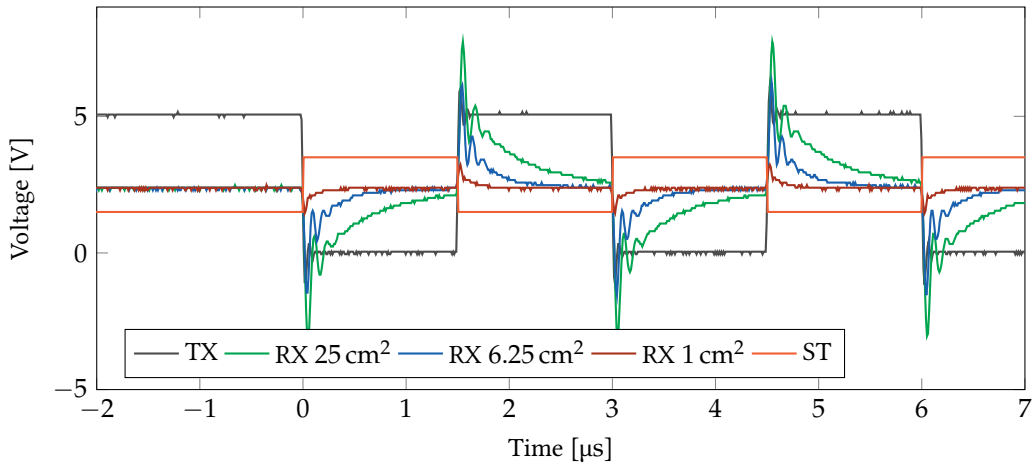

Figure 46: Influence of different capacitor sizes on the strength of the transmitted signal.

voltage to an appropriate value, even very small signal values can be solidly detected with this approach.

4.9.3.1 *Influence of Capacitor Size and Adhesive*

The aluminum layer of the pouch laminate as it is shown in Fig. 3 with the corresponding sizes influences the coupling capacitance. This results in two capacitors connected in series according to (47) with the pouch laminate's aluminum layer being one common capacitor plate for both capacitors and the attached coupling capacitor plates as shown in Fig. 41 being the respective counterparts for each of the serial capacitors. The resulting capacitances are displayed in Table 5.

$$C_{total} = \frac{C_1 C_2}{C_1 + C_2} \tag{47}$$

Table 5: Calculated and measured values for the couple capacitor with different capacitor plate sizes and the aluminum laminate in between.

Capacitor Plate Area [cm^2]	**Calculated capacitance** [nF]	**Measured capacitance** [nF]
25.00	0.78	0.7
6.25	0.19	0.2
1.00	0.07	0.1

Different sizes of capacitor plates attached to the aluminum laminate have been investigated. The goal is to use capacitor plates as small as possible to be able to integrate the system in any desired battery cell size while maintaining a signal strength strong enough to determine transmitted data reliably. For attaching the capacitor plates to the laminate, both, a thermally conductive adhesive and a normal adhesive have been researched. No difference in the signal quality could be recognized. All used capacitor plates have a quadratic shape with a side length of 1 cm, 2.5 cm and 5 cm. In Fig. 46, the output signals RX from the different capacitors are displayed in comparison to the input signal TX.

It is obvious that a bigger capacitor area leads to a stronger signal with higher peaks. This can however be solved by adjusting the voltage threshold of the Schmitt trigger that is integrated in the receiving microcontroller and responsible for identifying the signal. The output signal of the

Schmitt trigger (ST) is qualitatively shown in red. The influence of the aluminum layer in the pouch laminate can therewith be neglected as well. Parasitic effects from the electrode stack and if more than one cell are stapled together each with its own coupling capacitors are yet to be researched.

4.9.3.2 *Influence of Baud Rates*

In a further experiment, the influence of different baud rates for the signal transmission has been examined. For the investigation, capacitor plates with a side length of 5 cm haven been used. The researched baud rates have been 9600 bd, 750 000 bd and 2 000 000 bd. It has been found that contrary to the transmission of sinusoidal signals as described in [70], the transmission speed does not influence the attenuation of the signal. This effect can be explained with the steep edges of the signal. Changes between HIGH and LOW are performed within a few nanoseconds. The only limitation in this context is on one hand the resonance frequency of the setup which should not be undercut. This resonance frequency is limited by the high pass filter that is formed by the coupling capacitor and resistances parallel to it. On the other hand, above mentioned potentially existing parasitic effects from the electrode stack which could weaken the signal strength significantly have to be further dealt with.

4.10 CONCLUSION: IN-SITU TEMPERATURE SENSING

Different methods for in-situ temperature sensing have been described. Therefore, various requirements for sensor integration have been defined and possible sensor designs elaborated. Since off-the-shelf sensors do not fulfill the necessary requirements, different self-made sensors are investigated.

In Section 4.4, a wire-based platinum sensor is described that has been integrated into a double-layered separator sheet. The big production effort and the fragility of the applied platinum wire as well as the hard to reproduce lab-scale pouch cell demands for more robust solutions.

Section 4.6 and Section 4.7 look therefore into two iterations of self-made thermocouples with Kapton substrates and different coatings. Leakage of the coating led to big discrepancies between the values gained during calibration and from in-cell measurements. In Section 4.8 the production process of a platinum-based thin-film sensor that has been integrated into a polyimide foil is therefore discussed.

Since the cell leakage at the feed-through could even with this method not be fully solved, a wireless data transmission system that uses capacitive coupling through the cell's casing has been proposed in the last part of the chapter at hand. A battery-powered prototype is therefore set up to proof the concept for data transmission. Different solutions for miniaturizing the system and optimizing it in terms of cost and power-consumption have been proposed. A full realization and integration of the system is not part of this chapter.

5

MEASURE OF INHOMOGENEITY

To qualify and quantify the inhomogeneity in a cell, in the following the MOI is defined. First, a look into different existing definitions as they are used in different disciplines is taken and evaluated how suitable they are for battery applications. Example distributions are therefore used to compare the different methods. After that IR measurements from a 40 Ah cell are investigated with the finally chosen measure and the results verified.

5.1 DEFINITIONS FROM LITERATURE

In order to express the amount of inhomogeneity in a temperature distribution a valid measure needs to be defined that best reflects the state of inhomogeneity and its potential influence on other parameters in the cell. In order to find a measure that fulfills these requirements, in the following different potential definitions from literature and from different disciplines are generally described for population distributions and specifically evaluated for temperature distribution applications by applying the measure on example distributions given in Fig. 47. Unless differently stated for all equations the parameters are defined as follows. n is the total population size in a population distribution according to (48) on an area s that is sectioned into x^2 unit cells. Each unit cell has a certain value n_i with $i \in 1,\ 2,\ 3,\ \ldots,\ x^2$. The segmentation of an area is defined as $k = s/x^2$.

$$n = \sum_{i=1}^{x^2} n_i \tag{48}$$

Additionally, the average of a population distribution is defined as μ according to (49) and the weighted average in a non-random population distribution as μ_p according to (50) where p_i is the probability weight for each ith element and X the sum of the weights [84].

$$\mu = \frac{1}{x^2} \sum_{i=1}^{x^2} n_i \tag{49}$$

$$\mu_p = \frac{1}{X} \sum_{i=1}^{x^2} p_i n_i, \qquad \text{where } X = \sum_{i=1}^{x^2} p_i \tag{50}$$

5.1.1 *Linear Approach*

A very basic approach for estimating the inhomogeneity in a population distribution is to set the difference of the highest and lowest value of n_i in relation to the average value μ as shown in (51). The resulting value h_{mm} is a basic estimation on how the values of the distribution differ from the average.

$$h_{mm} = \frac{n_{max} - n_{min}}{\mu}, \qquad \text{where } n_{max} = \max_i n_i, \quad n_{min} = \min_i n_i \tag{51}$$

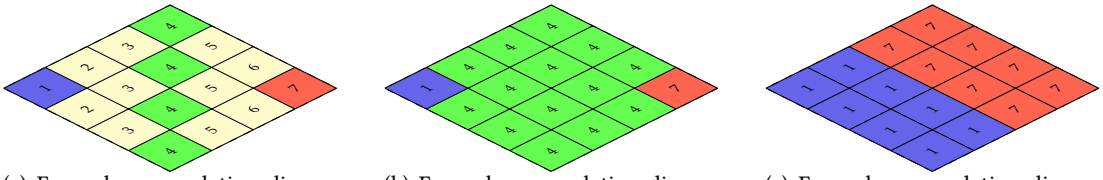

(a) Exemplary population distribution with a smooth gradient between neighboring unit cells

(b) Exemplary population distribution with one minimum and one maximum spot

(c) Exemplary population distribution with a minimum and a maximum half

Figure 47: Exemplary population distributions with $\mu = 4$ and $h_{mm} = 1.5$ with n_{max} in red, n_{min} in blue and μ in green

The resulting values are $|h_{mm}| \geq 0$, where 0 stands for a fully homogeneous distribution with every unit cell having the average value. The more the measure however deviates from 0, the wider is the spread in the values of the population distribution.
A drawback of this method is that no information about the values of the unit cells between the minimum and the maximum value are reflected in the measure. Smooth gradients in the distribution will not appear differently in the measure than saltuses if the minimum, maximum and average values are the same. Fig. 47 shows different example distributions that all result in the same value for $h_{mm} = 1.5$. Population size and probabilities for each value are similarly neglected with this approach. Also the local position of extrema can not be detected.

5.1.2 *Average value and standard deviation*

Another simple method to estimate the variation from the average of a population is the standard deviation σ. Other than the method described in Section 5.1.1 it describes the quadratic deviation of the population from the average. It therefore weights values higher that differ more from the average and gives a good estimation how widespread a population distribution is. For randomly distributed populations the standard deviation is defined according to (52) [26]. The resulting values are in the range of $\sigma \leq \sqrt{\frac{(n_{max}-n_{min})^2}{4}}$.

$$\sigma = \sqrt{\frac{1}{x^2}\sum_{i=1}^{x^2}(n_i - \mu)^2} \tag{52}$$

The achieved results for the standard deviation σ applied to the distributions from Fig. 47 is shown in Table 6. It shows a significant improvement compared to h_{mm} as it is able to distinguish between the different distributions.
In case of non-random population distributions a probability factor p_i for each element of the population is applied according to (53)[84] with the weighted average μ_p. A popular use-case for this weighted distribution is the calculation of the total mark for final exams. A thesis is weighted more than a single subject's exam.

$$\sigma_p = \sqrt{\frac{1}{X}\sum_{i=1}^{x^2} p_i(n_i - \mu_p)^2} \tag{53}$$

For a distribution like in the example Population Distribution Charts (PDCs) from Fig. 47, the probabilities should be set such that the maximum values are higher weighted than the other values. While the distributions where only one unit cell holds the maximum value n_{max} (Figs. 47a and 47b) show similar weighted standard distribution values, a significant increase in this value can there-

	Fig. 47a	Fig. 47b	Fig. 47c	min	max
μ	**4.0**	**4.0**	**4.0**	-	-
h_{mm}	**1.5**	**1.5**	**1.5**	-	-
σ	**1.58**	**1.06**	**3.00**	0	3
S_Δ	**0.133**	**0.062**	**0.496**	6.22	0
h_G	**0.67**	**0.03**	**2.4**	0	64
h_S	**0.156**	**0.047**	**0.375**	0	1

Table 6: Calculated values for evaluation of the suitability of different measures based on the simple population distributions form Fig. 47

with be observed for the PDC with more unit cells at the maximum n_{max} (Fig. 47c). This weight factor can in later applications be important to express the influence of e.g. high temperatures on the aging of materials.

5.1.3 *Q Statistic and I^2 Index*

The standard deviation, or rather its square the variance σ^2, finds application in the Q_h statistic and I^2 index. Both measures, as they are described in [46], are used in the meta-analysis mainly of social or medical research to compare an amount k of studies concerning their homogeneity. For simplification, only the case of a fixed-effects model is described here. This model can be applied if all compared studies are functionally identical and if the common effect size of the whole researched population is to be computed and not generalized for other non-researched populations [13].

A control group with size n_C and an experimental group with the size n_E are compared for these studies. A correction factor $c(m)$ as defined in (54)[40], with $m = n_C - 1$ is introduced for small sample sizes to correct the positive bias that is suffered by the standardized mean.

$$c(m) = 1 - \frac{3}{4m - 1} \tag{54}$$

With the help of this correction factor, an estimator for parametric effects is defined, e.g. according to [40] in (55) with μ_E and μ_C being the means of experimental and control group and σ_C the standard deviation of the control group (see [40, p. 105]).

$$g = c(m)\frac{\mu_E - \mu_C}{\sigma_C} \tag{55}$$

The sampling variance of the g-index is, based on this, defined in (56).

$$\sigma^2_{g,i} = \frac{n_E + n_C}{n_E n_C} + \frac{g^2}{2(n_C - 1)} \tag{56}$$

Huedo-Medina suggests d as it is defined in (57) and proposed by Hedges et al. [44] to be a better estimator for the parametric effect size [46] with σ_h according to (58) and, other than defined for (55), $m = n_E + n_C - 2$. The sampling variance is accordingly defined in (59).

$$d = c(m)\frac{\mu_E - \mu_C}{\sigma_h} \tag{57}$$

$$\sigma_h = \sqrt{\frac{(n_E - 1)\sigma_E^2 + (n_C - 1)\sigma_C^2}{m}} \tag{58}$$

$$\sigma_{h,i}^2 = \frac{n_E + n_C}{n_E n_C} + \frac{d^2}{2(n_C + n_E)} \tag{59}$$

Q_h is then defined in (60) with w_i being the weighting factor, n_i the estimation of the parametric effect size according to (55) and (57). $\bar{n}$ is the weighted average of the effect estimates according to (61).

w_i is defined to be the inverse within-study variance given for each ith study in a fixed-effects model. The weighting factor is therewith $w_i = \frac{1}{\sigma_i}$ were σ_i corresponds to the variances defined in (56) and (59) respectively [46]. n_i corresponds accordingly to g or d as defined in (55) or (57) respectively.

$$Q_h = \sum w_i (n_i - \bar{n})^2 \tag{60}$$

$$\bar{n} = \frac{\sum_i w_i n_i}{\sum_i w_i} \tag{61}$$

The way, Q_h is defined does not make it suitable for estimating the inhomogeneity in a single population distribution per se, as a comparison group needs to be given. In order to qualify the measure for the example distributions given in Fig. 47, we define a population distribution with the same size of $x = 16$ and with $n_i = 3$ for all unit cells. As the measure g is only based on the average of the distributions and the standard deviation of the comparison group, and the examples from Fig. 47 are chosen such that the average for all population distributions is the same, $Q_h = 0$ for $n_i = g$. It shows that this measure is not suitable for the comparison of distributions like that. When the measure d is used, $Q_h = 8.83$ results.

[46] mentions that Q_h statistics however only shows whether the set of studies is homogeneous or not, while the I^2 index quantifies the degree of inhomogeneity. To quantify the inhomogeneity of a set of studies, I^2 is then introduced according to (62) where the Q_h is compared to its expected value. k as mentioned above is therein the amount of studies that are to be compared.

$$I^2 = \begin{cases} \frac{Q_h - (k-1)}{Q_h} & \text{for } Q_h > (k-1) \\ 0 & \text{for } Q_h \leq (k-1) \end{cases} \tag{62}$$

For above example, this results in an I^2 value of $I^2 = 77.35\%$ when measure d is used as parametric effect size estimator, with higher percentages meaning a higher inhomogeneity.

For battery applications, if different cells within a whole pack are to be compared and measurement data of one example cell can be used as comparison group, these measures can be suitable. For the investigation of inhomogeneity in one single cell, the method can not be applied.

5.1.4 *Entropy-derived method*

The entropy S given in J/K is an extensive state function that describes the amount of disorder within a system. The change of entropy in thermodynamics is defined according to (63) over the reduced heat ΔQ, which was introduced in (15) for reversible processes [98, p. 587] with the heat capacity C.

$$\Delta S = \frac{d\Delta Q}{T} = \frac{C\Delta T}{T} \tag{63}$$

A more general definition that shows the correlation of entropy on the amount of micro states Ω in a system is given by (64) with the Boltzmann constant k_B [98, p.588].

$$S = k_B \log \Omega \tag{64}$$

While the entropy in its nature is the same at one point of time within a closed system [77], in [34] and [81] the measure is adjusted such that it can be generally used for inhomogeneity detections in spatial patterns. To receive a simplified description, the entropy values can be related to the Boltzmann constant and therewith $k_B = 1$. The amount of micro states, or "number of distinguishable spatial arrangements of the objects" Ω on an area s is calculated by (65) with the number of grid squares x^2 with a size of $k \times k$ and n_i being the integral fraction of the population in the unit cell (in the here described study the amount of black pixels) [81].

$$\Omega(k) = \prod_{i=1}^{x^2} \binom{k^2}{n_i}, \qquad \text{with } k^2 = \frac{s}{x^2} \tag{65}$$

The "highest value of configurational entropy" is defined in [34] and further elaborated in [81] as stated in (66), with $r_0 = (n \bmod x^2)$, $r_0 \in 0,\ 1,\ \ldots,\ x^2 - 1$ and $n_0 = (n - r_0)/x^2, n_0 \in 0,\ 1,\ \ldots,\ k^2 - 1$.

$$S_{max}(k) = \log \Omega_{max}(k) = \log \left[\binom{k^2}{n_0}^{x^2 - r_0} \binom{k^2}{n_0 + 1}^{r_0} \right] \tag{66}$$

The relative measure per cell of local inhomogeneity is therewith defined by building the difference between the maximum entropy $S_{max}(k)$ and the actual entropy in this cell $S(k)$ and averaging it over the total number of unit cells x^2. The thereof resulting MOI is given in (67) and simplified for point objects in (68)[81], [34]. Point objects are defined by [34] as single particles that are inclosed in a pixel grid.

$$S_\Delta(k) = \frac{S_{max} - S}{x^2} = \frac{r_0}{x^2} \log \frac{k^2 - n_0}{n_0 + 1} + \frac{1}{x^2} \sum_{i=2}^{x^2} \frac{n_i!(k^2 - n_i)!}{n_0!(k^2 - n_0)!} \tag{67}$$

$$S_\Delta(k, PO) = \frac{S_{max} - S}{x^2} = -\frac{r_0}{x^2} \log (n_0 + 1) + \frac{1}{x^2} \sum_{i=2}^{x^2} \frac{n_i!}{n_0!} \tag{68}$$

To see what this measure means, it, like the above measures, is applied for the example distributions in Fig. 47. Since the grid squares x in the example distributions are not subdivided in binary cells, k is chosen as a quadratic value such that the highest value of a unit cell in the whole area can be born with binary cells. In the example distributions, the highest value is 7. In order to cover this value, a quadratic value of $k = 9$ is chosen to divide the picture in binary cells. The amount of unit cells is $x^2 = 16$. The resulting values for S_Δ for the example distributions are presented in Table 6.

[35] is suggesting a strong correlation between the simplified measure from (68) and the measure h_G that is introduced in the following section.

5.1.5 *Garncarek's Method*

Czainski and Garncarek define in [35], [19] and [36] a "measure of the degree of inhomogeneity in a distribution", below referred to as "Garncarek's Method". [35] uses the measure to quantify the heterogeneity in a thermal field, while [36] applies this measure to quantify the variations in a fluidized bed, and [19] adapts the method for characterizing inhomogeneities in the thickness of thin metallic films.

A population of the size n is distributed on an area s which is separated into x^2 equally sized unit cells in order to estimate the inhomogeneity. The ith unit cell comprises the share n_i of the total population size according to (48).

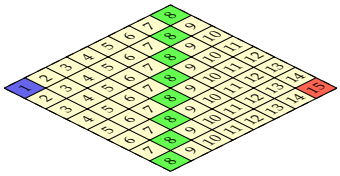

(a) Exemplary population distribution with a smooth gradient between neighboring unit cells. $h_G = 1.348$.

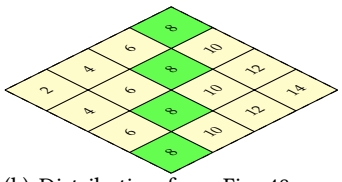

(b) Distribution from Fig. 48a with a $x = 4$. $h_G = 1.316$.

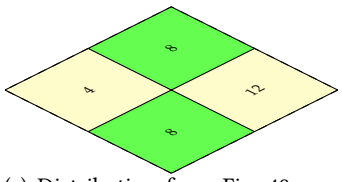

(c) Distribution from Fig. 48a with a $x = 2$. $h_G = 1.354$.

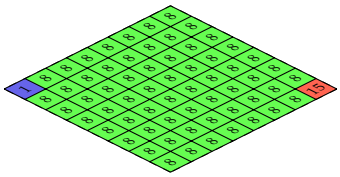

(d) Exemplary population distribution with a cold and a hot spot. $h_G = 0.194$.

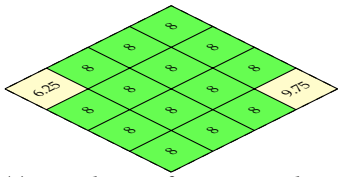

(e) Distribution from Fig. 48d with a $x = 4$. $h_G = 0.051$.

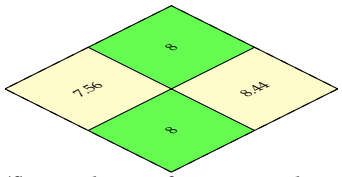

(f) Distribution from Fig. 48d with a $x = 2$. $h_G = 0.016$.

Figure 48: Exemplary population distributions with different grid sizes

The population is according to [19] considered to be homogeneously distributed on the scale s/x^2 if, for each ith unit cell, n_i is equal to the average number of objects per cell $n_i = n/x^2$. For $n = const.$ the measure of inhomogeneity is therewith defined according to (69).

$$\mu_G = \sum_{i=1}^{x^2} (n_i - \frac{n}{x^2})^2 \tag{69}$$

However, if different populations with a different size n need to be compared, μ_G cannot be applied as a measure. In order to be able to do so, h_G is introduced as a measure for inhomogeneity in (70) according to [35] and [36]. If $h_G = h_{G\,min} = 0$, the population is considered to be fully homogeneous. The highest number of inhomogeneity is reached for $h_G = h_{G\,max} = n$, meaning that all occurrences of the population happen in a single unit cell of the distribution.

$$h_G = -\frac{n}{x^2 - 1} + \frac{x^2}{n \cdot (x^2 - 1)} \sum_{i=1}^{x^2} n_i^2 \tag{70}$$

For the above given example distributions the results are again displayed in Table 6. For being able to compare different distributions, the sizes of the unit cells are varied from smalls cells that e.g. just contain one value or pixel to big cells that represent an average of a certain region in the distribution. To illustrate this, example distributions are shown in Fig. 48 with grid sizes of $x^2 = 64$, and $x^2 = 16$ and $x^2 = 4$ respectively. Figs. 48a to 48c show with Garncarek's method a quite constant inhomogeneity through all the grid sizes, while Figs. 48d to 48f get more homogeneous with rising grid sizes. From this fact it can be seen that the original distribution in Fig. 48d showed wider homogeneous regions than Fig. 48d with only minor deviations.

The definition of h_G is described as to be only valid for populations of similar size n which for above example distributions is valid. If the population size however defers by one or more orders of magnitude, a different measure needs to be applied to make populations comparable in terms of inhomogeneity. Therefore, [36] defines H_G based on (70), the expected value of the measure h_G, $E(h)$ and the standard deviation σ_h in (71) and (72) respectively. Another possibility for adjusting the measure to distributions with a larger deviation between single grids would be to introduce a standardization prefactor. For a temperature distribution, as it is present in batteries, the prefactor would need to be chosen such that the sum of all temperatures remains constant.

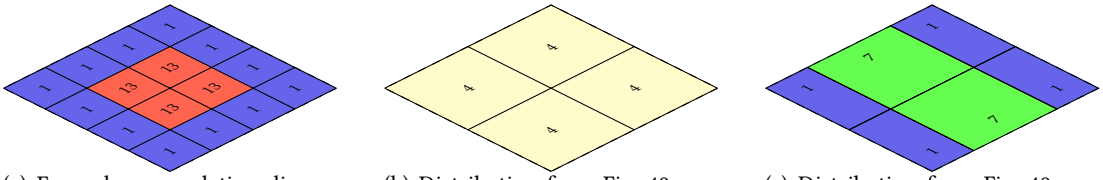

(a) Exemplary population distribution with a the temperature hot spot in the center. $h_G = 7.2$ and $h_S = 0.5625$.

(b) Distribution from Fig. 49a with a $x = 2$ and no offset. $h_G = 0$ and $h_S = 0$.

(c) Distribution from Fig. 49a with a $x = 2$ grid and an offset of $\delta_x = 1$. $h_G = 3$ and $h_S = 0.375$.

Figure 49: Exemplary population distributions with grid sizes of $x = 4$ and $x = 2$ without and with an offset in x direction

Both, h_G and H_G are dimensionless. h_G, as mentioned above, has a range of $[0, n]$. H_G in contrast has a range of $\left[-\sqrt{\frac{n(n-1)}{2(x^2-1)}}, 0.5n\sqrt{2n \cdot (n-1)(x^2-1)}\right]$, where $H_G = 0$ represents the state of absolute randomness. Negative values imply that the distribution diverges from randomness towards homogeneity while positive values show a divergence of the distribution towards heterogeneity [36].

$$H_G = \frac{h_G - E(h)}{\sigma_h} \tag{71}$$

$$H_G = \sqrt{\frac{n \cdot (x^2-1)}{2 \cdot (n-1)}} \left[\frac{1-n-x^2}{x^2-1} + \frac{x^2}{n \cdot (x^2-1)} \sum_{i=1}^{x^2} n_i^2\right] \tag{72}$$

Since the temperature distributions researched in this thesis all have $n = \sum_{i=1}^{x} T_i$ in the same order of magnitude $\times 10^5$, with T_i being the temperature of each grid point in °C, this measure is not further dealt with. If instead of the absolute temperatures temperature deviations which are referred to the temperature minimum are taken into account, the order of magnitude of n still remains in the same range.

5.1.6 *Schilcher's Method*

In [91], Schilcher describes a method for measuring the inhomogeneity in spatial distributions of n nodes in a population. Similar to the method developed by Garncarek and described in Section 5.1.5, the defined measure is grid-based and has the goal to quantify maxima or hot-spots in the distribution. A rectangular area s with side lengths a and b is segmented into x^2 unit cells x_i with $i = 1, 2, \ldots, x^2$. To be able to detect accumulations of elements in the population distribution, even if it is centered, which means to make the "measure independent of linear operations"[91], an offset $(\delta_x, \delta_y) \in [0, \frac{a}{x}) \times [0, \frac{b}{x})$ of the segmentation x^2 is defined. The grid of unit cells is shifted by the offset δ_x to the right in the horizontal direction. The parts of the segmentation that leave the area s on the right, are used to fill up the space on the left. δ_y has the same function in the vertical direction. Fig. 49 shows exemplary the offset in horizontal direction δ_x. It can be seen, that without an offset at the grid size of $x^2 = 4$ the population distribution seems to be homogeneous with $h_G = 0$ and $h_S = 0$ while, if an offset in x-direction of $\delta_x = 1$ is applied, a clear temperature increase in the middle is visible. The location of the hot spot can be further narrowed down by applying an offset in y-direction δ_y.

Based on this, Schilcher introduces the expected number $\bar{E}(x)$ for each unit cell x_i according to (73). The deviation $E_{i,(\delta_x,\delta_y)}$ of the actual number of nodes n_i in a section x_i from the expected

value $\bar{E}_i(x)$ is "an indicator of the local inhomogeneity" for the population distribution [91]. The measure of inhomogeneity is therefore defined as in (74).

$$\bar{E}(x) = \frac{n}{x^2} \tag{73}$$

$$h_{S(\delta_x,\delta_y)}(x) := \frac{1}{2 \cdot n} \sum_{i=1}^{x^2} |E_{i,(\delta_x,\delta_y)} - \bar{E}(x)| \tag{74}$$

As mentioned before, Schilcher's method is developed such that it is independent of linear operations. This is achieved by choosing an offset (δ_x, δ_y) that maximizes the inhomogeneity for a given segmentation x according to (75).

$$h_S(x) = \max_{(\delta_x,\delta_y)} h_{S(\delta_x,\delta_y)}(x) \tag{75}$$

Schilcher furthermore suggests a refinement of the segmentation in order to take more local deviations from a homogeneous distribution into account. As the examined population is integral, this is achieved by refining the segmentation $x = 2,\ 4,\ 8,\ \ldots,\ 2^r,\ r \in \mathbb{N}$, until each unit cell x_i contains maximum one node n_i. The final definition of h_S is given in (76) with the constant $w \approx 4.79129$ [91]. The range for h_S is $]0, 1]$ with values close to 0 representing a homogeneous distribution.

$$h_S := \frac{1}{n} \sum_{j=1}^{r} w^{1-j} \max_{(\delta_x,\delta_y)} \sum_{i=1}^{2^{2j}} |E_{i,(\delta_x,\delta_y)} - \frac{n}{2^{2j}}| \tag{76}$$

Since this method with the suggested refinement is only able to handle discrete numbers $n \in \mathbb{N}$, it is not directly applicable for temperature distributions. Therefore, the maximum amount of known values is chosen for the grid size. In case of an IR image, this means 1 pixel as resolution. For the example distribution from Fig. 49a the calculation is performed exemplary with $\delta_x = \delta_y = 1$ with a grid size of $x^2 = 4$ and inhomogeneity of $h_S = 0.5625 = 56.25\%$ results. This is equal to the result for PDC with a grid size of $x^2 = 16$ and shows that the offset leads to a space and - until a certain point - grid-size independent solution. For the example distributions from Fig. 47 the resulting values are displayed in Table 6.

5.1.7 *Evaluation of the Different Measures of Inhomogeneity for Temperature Distributions in Battery Cells*

Since, as comprehensively discussed in Chapter 2, the temperature has an exponential influence on the aging of a cell, the chosen MOI should represent this fact by weighting higher temperatures more than lower temperatures.

Q statistics and I^2 index are not suitable for the research of inhomogeneities within one single cell but rather could be used to compare different cells from the same manufacturing batch regarding their variations.

The linear approach described in Section 5.1.1 and Schilcher's method from Section 5.1.6 show linear dependencies. The latter however has the advantage of being space-independent, and therefor recognizing hot spots better, by shifting the grid by an optimized offset. Another advantage is, that the measure is normalized over n and therewith different PDCs are better comparable.

The entropy-derived method, since it is a combinatorial method, only allows discrete numbers as input. For temperature distributions with sometimes small differences, it is therefore not suitable without applying a discretization on the temperature values. This would however lead to a loss in accuracy.

The standard deviation Section 5.1.2 and Garncarek's method Section 5.1.5 take values quadratically into account which means, extrema, both lows and highs, are weighted more.

From above described methods for defining the MOI, Garncarek's and Schilcher's measures seem to be the most suitable ones for investigating the inhomogeneity of temperature distributions in solids like lithium ion pouch cells. Although Garncarek describes the measure h_G in [35] first for the application in thermal fields, some adjustments and definitions are necessary to calculate the MOI for temperature distributions in lithium ion cells. This is mainly caused by the fact that the temperature gradients analyzed in [35] as well as other analyzed populations from [36] and [19] are natural numbers and of several orders of magnitude bigger than the gradients usually present in battery cells during normal operation. A standardization or discretization of the temperature values could address this problem. A loss in accuracy is however the result. Also, similar to Schilcher's method, Garncarek should be adjusted such that it is universally applicable.

The offset in x and y direction is brought in with (77) depending on the segmentation x.

$$h_G(x) = \max_{(\delta_x,\delta_y)} h_{G(\delta_x,\delta_y)}(x) \tag{77}$$

The measure is made comparable for different PDCs with varying sizes n. $h_G(x)$ is normalized over n and (78) results.

$$h_n(x) = \frac{h_G(x)}{n}, \qquad \text{with } h_n \in [0,1] \tag{78}$$

For two dimensional distributions the analyzed surface is sectioned into arbitrary small equally distributed square segments. In an IR image this corresponds to pixels. If a three dimensional temperature distribution is to be analyzed, the body is segmented accordingly into arbitrary small cubes. The three-dimensional solution is not further described in the following, as the method works according to the two-dimensional approach.

This method works well for relatively small PDCs with lower x^2 values with big differences ($\geq 1\,\mathrm{K}$) between each unit cell. When however looking at the IR measurements from Fig. 56 that are based on 194×194 pixels, differences between the cells are small and values of $h_n = 6.87 \times 10^{-11}$ for an 8 C discharge at 0 % SOD and of $h_n = 3.29 \times 10^{-8}$ for 100 % SOD are the result. This gives the impression that both distributions are close to homogeneity, which is true for the distribution at 0 %SOD. Since the distribution at 100 %SOD shows a significantly bigger gradient, the value for inhomogeneity should also significantly diverge form homogeneity. With Schilcher's method in contrast $h_S = 9.04 \times 10^{-4}$ and $h_S = 0.02$ are achieved which show larger deviations from the state of homogeneity $h_S = 0$.

In Fig. 50 the normalized Garncarek measure is compared with Schilcher's measure for the 1 C discharge of the cell already shown in Fig. 56. Both measures show a similar trend, but the normalized Garncarek measure shows clearer the homogeneous distribution at the beginning of the discharge and a significant increase towards the end. Therefore, Garncarek, even though the values are smaller is better suitable.

Since, it's also desirable to have information about the location of extreme values in the cell, the inhomogeneity is calculated column and row wise and displayed in Fig. 51. In both plots it is again obvious that inhomogeneity rises over the SOD. Furthermore, in both directions the inhomogeneity seems to be higher towards the edges of the cell. This can be explained with the transition from the cell to the surrounding air. Variations in the MOI are lower ($\times 10^{-10}$) in x-direction than in y-direction ($\times 10^{-9}$). A significant increase in inhomogeneity can be detected in both graphs towards the side where the tabs, and, in the plot for the y-direction, especially the cathode tab is located. This is in good accordance with the images in Fig. 56. Another finding is a slightly increasing inhomogeneity between the tabs, which is also in good correspondence with the images in Fig. 56, where a small area with a large gradient is visible.

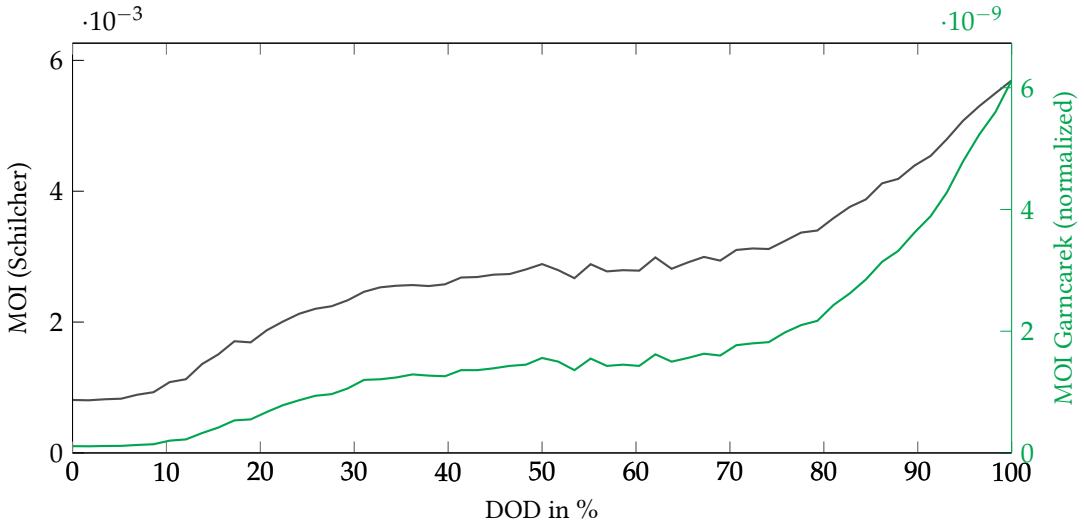

Figure 50: Comparison of the normalized Garncarek's measure h_n and Schilcher's measure h_S for a 1 C discharge from Fig. 56.

The curves for the 8 C discharge in Fig. 51 show of course bigger variations in the inhomogeneity. While again the area close to the cathode tab shows the biggest inhomogeneity. Another interesting finding is that at a higher discharge state the more homogeneous areas become larger. This corresponds again to the pictures in Fig. 56.

In summary, from the above mentioned measures, Garncarek provides the best qualitative measure to estimate local inhomogeneities in a temperature distribution. However, since the measure is originally designed for discrete population distributions with relatively big differences in the values of the unit cells, the resulting values are very small. For the 8 C discharge at the end of discharge, where temperature gradients are according to Fig. 55b in the range of 20 K, the resulting values are still only in the area of $\times 10^{-7}$. Since the range for h_n is however $[0, 1]$, this suggests a close to homogeneous distribution even for relatively large inhomogeneities. Table 7 shows a clearly presented comparison of the different methods. To better fit the demands of battery cells and also include the influence of the inhomogeneities on the aging, in the following a measure is defined that incorporates the Arrhenius equation, as introduced in Section 2.5.

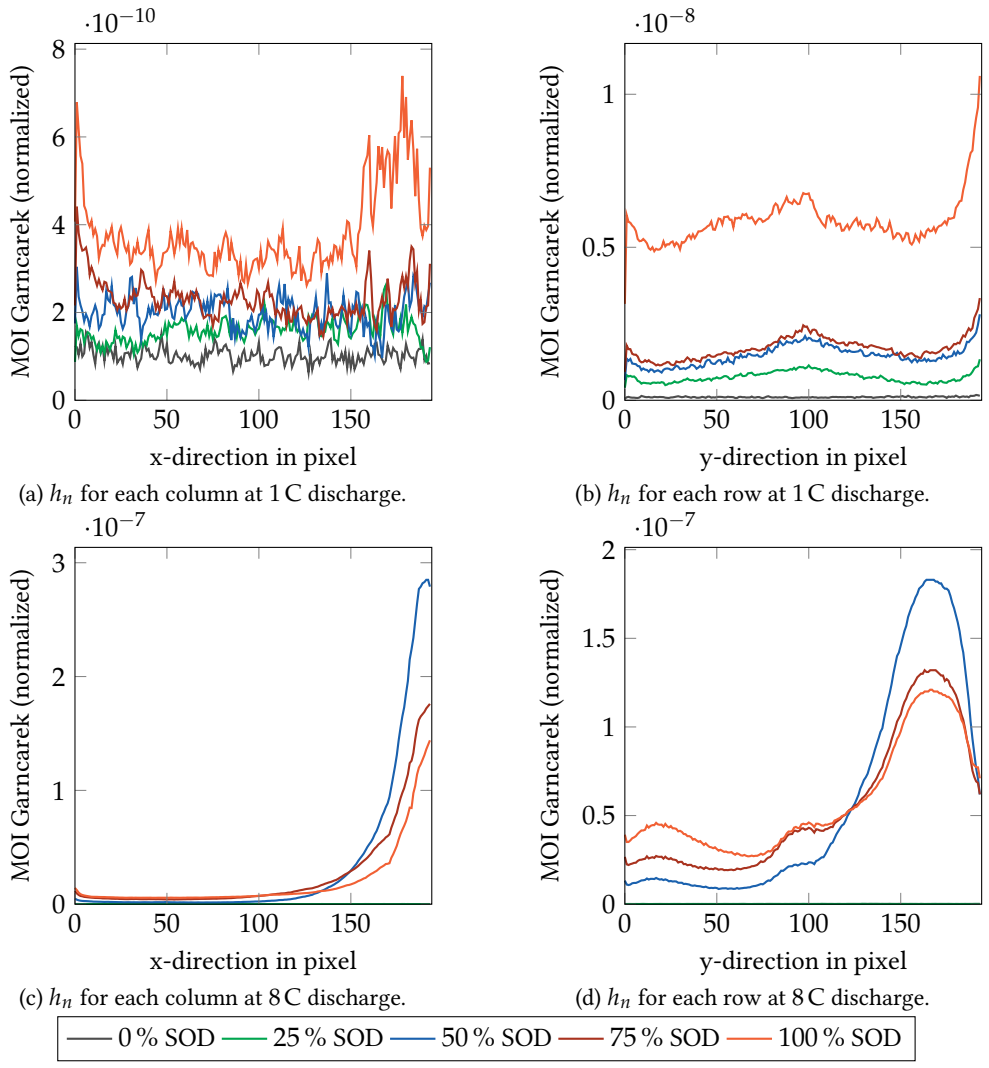

Figure 51: Inhomogeneity in x and y direction of a 40 Ah pouch cell at different SODs for 1 C and 8 C discharge based on the IR images from Fig. 56. The origin is on the opposite site of the tabs in accordance to Fig. 56 with the x and y maximum next to the cathode tab.

Method	Origin	Pro	Con	Suitability for Battery Application
Linear Approach	various disciplines	simple approach	no quantification of deviations from average	for basic information, no detection of hot spots
Average	various disciplines	simple approach	no detection of deviations or hot spots	Suitable for rough estimation for internal temperature
Standard deviation	various disciplines	simple approach, includes deviation from average	no detection of local hot spots	
Q statistic and I^2 Index	meta analysis of social studies	relative comparison of various studies	no suitability for quantification of deviations in one study	relative comparison of various cells, not for inhomogeneity in one cell
Entropy-derived method	quantification of disorder in a (electrochemical) system	good quantification of inhomogeneity	larger areas weigh more than small peaks	no quantification of hot spots
Garncarek's method	picture analysis, analysis of homogeneity of metal films	space resolved, grid based	larger areas weigh more than small peaks, only discrete numbers	no quantification of hot spots
Schilcher's method	population distribution	space resolved, grid based	only handling of discrete numbers	not suitable for small temperature gradients

Table 7: Comparison of different methods for MOI determination

5.2 ARRHENIUS-BASED MEASURE OF INHOMOGENEITY

The Arrhenius-based MOI that is defined in the following looks at the deviation in lifetime that is induced by local temperature inhomogeneities compared to a cell with the same average temperature but a homogeneous temperature distribution. For each measurement point, or - in case of an underlying IR measurement, relative lifetime change is calculated according to (18) and (21). With the assumed value for the activation energy $E_a = 50\,\mathrm{kJ\,mol^{-1}}$, as elaborated in Section 2.5, relative changes in the lifetime of a cell can be determined, assuming that E_a is nearly constant. $\lambda = E_a/R = 6013.66\,\mathrm{K}$ results. A 10 K temperature change leads therewith to a halving of the calendar life at room temperature of 300 K.

In order to find the best possible measure of inhomogeneity in a cell, the Arrhenius-based MOI for each measurement point is set in relation to three different temperatures T_{ref}. The three resulting measures are defined and evaluated in the following.

For the first defined measure of inhomogeneity, the calendar aging according to Arrhenius of each measurement point is set in relation to the aging of a homogeneously heated cell with the same **average temperature**. The lifetime deviation t_i of each measurement point is therewith calculated according to (79). Lifetime deviation means, the time difference between the point where a homogeneously heated cell at room temperature and a homogeneously heated cell at the temperature of the specific measurement point reach their EOL. The EOL is reached, when the relative capacity change compared to a new cell reaches 20 %.

The calendar aging t_i for each point i is calculated in comparison to the aging of the same cell at room temperature $T_0 = 300\,\mathrm{K}$ according to (79) with the relative capacity deviation ΔC_{rel}. The values for each point are summed up and normalized over the amount of measurement points x^2. The resulting time reduction is then compared to the time reduction from a homogeneously heated cell with the same average temperature t_{Av}. In case of the 8 C discharge at 100 % SOD (see Fig. 56j) this is $\overline{T} = 50.28\,^{\circ}\mathrm{C} = 323.43\,\mathrm{K}$. Fig. 52 shows a schematic drawing of the calculation of the lifetime deviation in comparison to a homogeneous temperature distribution at average temperature.

$$t_i = -\Delta C_{rel} e^{\left(\frac{\lambda}{T_i} - \frac{\lambda}{T_0}\right)} \tag{79}$$

For the whole cell with x^2 measurement points a measure of inhomogeneity M_A results according to (80) with $M_A : [0,1]$ where 1 is the highest degree of homogeneity and 0 the highest inhomogeneity. In this equation the relative capacity change ΔC_{rel} is canceled out. As Fig. 52 adumbrates, areas with higher temperatures decrease the overall lifetime, while areas with lower temperatures lead to an overall lifetime increase, which is physically correct. The measure through this fact might not fully reflect the inhomogeneity in the cell.

$$M_A = \frac{\sum_{i=1}^{x^2} t_i}{t_{ref} x^2}, \qquad \text{with } t_{ref} = t_{Av} = -\Delta C_{rel} e^{\left(\frac{\lambda}{T_{Average}} - \frac{\lambda}{T_0}\right)} \tag{80}$$

For this reason, the second reference temperature to which the inhomogeneity is related to, is the **minimum temperature** in a temperature distribution. The lifetime for each measurement point t_i is again calculated according to (79) with T_{min} being the minimum temperature at every test step. The resulting MOI can be also calculated with (80) but with $t_{ref} = t_{min} = -\Delta C_{rel} e^{\left(\frac{\lambda}{T_{min}} - \frac{\lambda}{T_0}\right)}$. The advantage of this measure compared to the above defined M_A is that deviations exist only in one direction, namely the lifetime reduction and the measure is therewith stronger.

A third reference temperature that should be taken into account is the temperature of the cell at the beginning of discharge. Since at this point the temperature distribution is considered to be homogeneous, the average temperature at this point is taken to calculate t_{ref} again with the help of (80), but with $T_{Av,0SOD}$ being the average temperature at 0 % SOD instead of $T_{Average}$. The advantage of this measure is, that the overall calendar life time reduction of the heated cells is

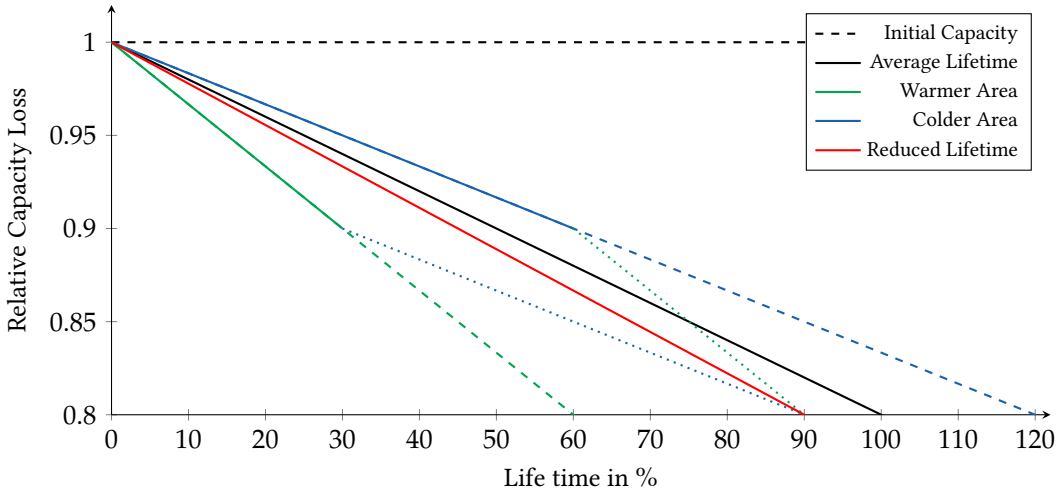

Figure 52: Schematic drawing of the calculation of the lifetime reduction due to inhomogeneity in a cell for two measurement points.

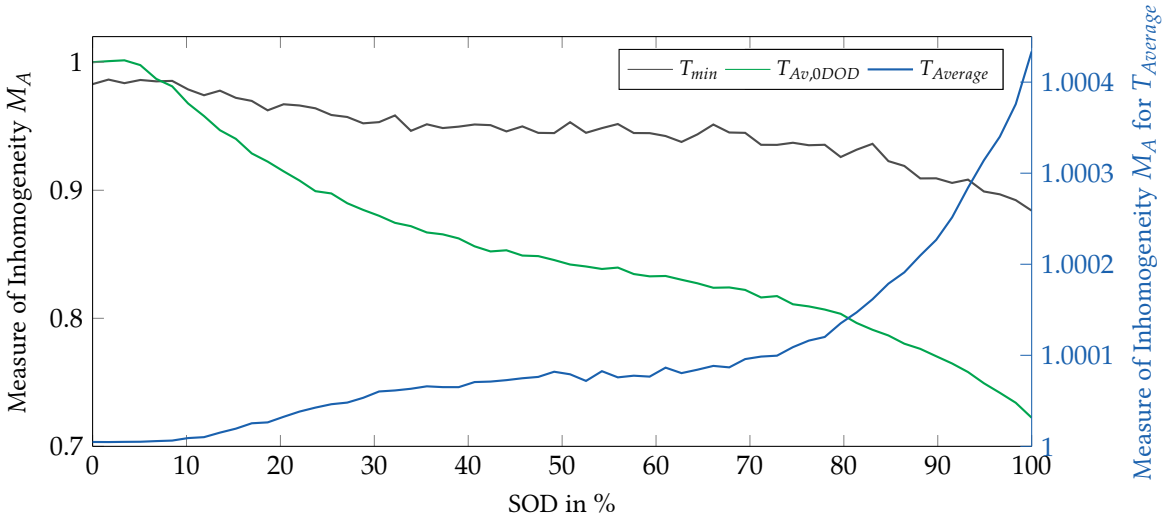

Figure 53: Measure of inhomogeneity M_A with different reference temperatures of the cells over SOD during 1 C discharge.

better considered in comparison to a cell stored at room temperature. Since the defined measure of inhomogeneity should however mainly consider influences of inhomogeneities but not influences of an overall temperature increase, this measure is considered to be less suitable. Inhomogeneities within the cell would become too insignificant compared to the overall temperature rise during discharge.

In Fig. 53 the three discussed measures are displayed for 1 C discharge based on aforementioned IR measurements. From this figure it becomes clear, that taking the average temperature of the current state $T_{Average}$ as a reference to calculate M_A is not suitable solution to estimate the inhomogeneity of a whole cell. Through the shift towards higher temperatures in the temperature distribution with a wider spread towards smaller temperatures, as it has been depicted in Fig. 55a, the measure is rising and reaches values above 1. This would mean a rising lifetime compared to the average value, which is not a realistic effect. When looking into the row- and column-wise inhomogeneity in Figs. 54e and 54f the measure shows an inhomogeneity minimum close to the

tabs and a maximum in the left quarter of the cells in x-direction. In y-direction the changes in inhomogeneity are very small and therefore with this measure negligible.

As suggested before, $T_{Av,0SOD}$ as a reference temperature for the calculation of M_A shows best the influence of the rising temperature on the aging. Since the rise in the average temperature at one state is however prevailing the inhomogeneities during this one state, this measure is not considered to be suitable. In Figs. 54c and 54d this fact becomes very clear. Therefore, for further considerations, the measure of inhomogeneity is defined with the minimum temperature as a reference, according to (81).

$$M_{AM} = \frac{\sum_{i=1}^{x^2} t_i}{t_{min} x^2}, \qquad \text{with } t_{min} = -\Delta C_{rel} e^{\left(\frac{\lambda}{T_{min}} - \frac{\lambda}{T_0}\right)} \tag{81}$$

The values for this measure reach from 0 for the highest possible inhomogeneity to 1, which depicts a homogeneous state. Figs. 54a and 54b show the MOI distribution in x and y direction for the cell at different SODs. Smaller temperature gradients show bigger deviations from the reference temperature. One drawback of this measure becomes clear when comparing the results in Fig. 54 with the IR images from Fig. 56: the detected inhomogeneity considers only deviations towards higher temperatures, while Garncarek's method is able to detect deviations in either way. Since a cold inhomogeneity, meaning an inhomogeneity with bigger deviations towards colder temperatures, is not considered to have an influence on the lifetime or safety of a cell, this draw back can be condoned. Furthermore, this cold inhomogeneity can be detected from inhomogeneity changes towards higher values of M_{AM}. Detecting the exact location of inhomogeneities, which seems better possible with $T_{Average}$ as reference temperature, plays a minor role in this measure. With these considerations, M_{AM} provides an overall strong MOI that fulfills all above mentioned requirements.

If not an infrared image builds the basis for calculating the temperature inhomogeneity in the cell but only a few sensors, a weighting factor needs to be engaged to quantify the inhomogeneity properly. In the course of the thesis, a weighting factor of $w = 500$ is suggested for sensing data corresponding to the average temperature compared to maximum and minimum values. This factor is taken in accordance to the Gaussian distribution that the temperature values show in the infrared measurements in Fig. 55, where the areas of the average value are significantly higher than the minimum and maximum areas. Eq. (82) shows the respective equation with w as the weighting factor and x^2 the amount of sensing points. The weighting factor has to be adjusted depending on the amount of sensing points in relation to the area which is investigated. $w = 500$ was found to suit best for an area in the range of $200\,\text{pixels} \times 200\,\text{pixels}$ and up to three to four sensing points.

$$M_{AM,w} = \frac{\sum_{i=1}^{x^2} t_i w}{t_{min} x^2}, \qquad \text{with } t_{min} = -\Delta C_{rel} e^{\left(\frac{\lambda}{T_{min}} - \frac{\lambda}{T_0}\right)} \tag{82}$$

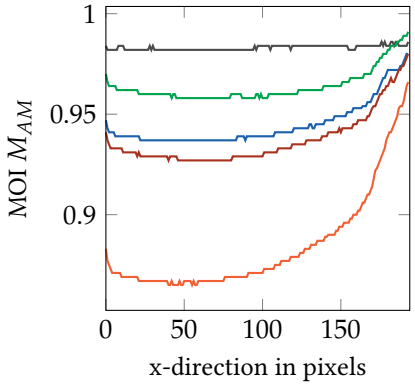

(a) MOI M_{AM} with $T_{ref} = T_{min}$ for each column at 1 C discharge.

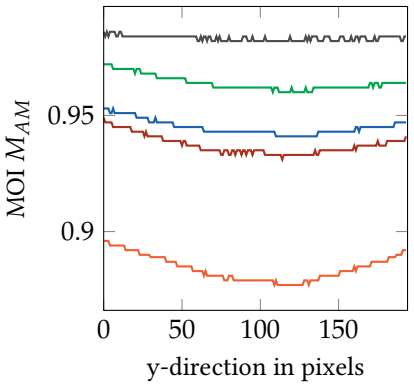

(b) MOI M_{AM} with $T_{ref} = T_{min}$ for each row at 1 C discharge.

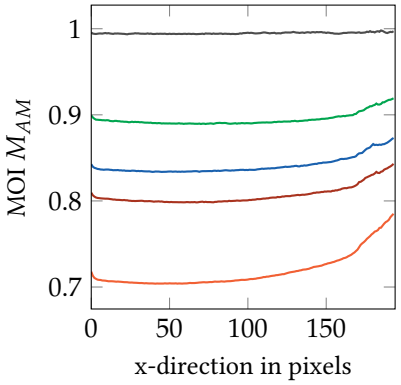

(c) MOI M_A with $T_{ref} = T_{Av,0SOD}$ for each column at 1 C discharge.

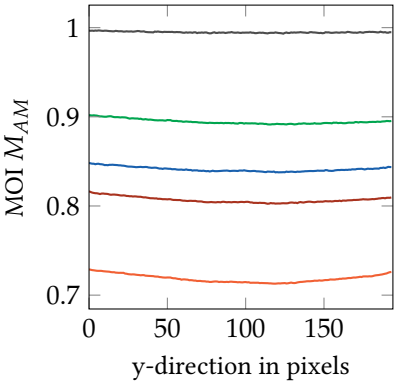

(d) MOI M_A with $T_{ref} = T_{Av,0SOD}$ for each row at 1 C discharge.

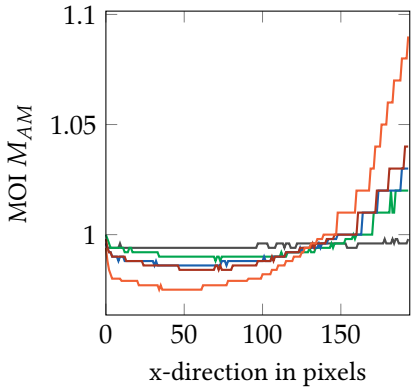

(e) MOI M_A with $T_{ref} = T_{Average}$ for each column at 1 C discharge.

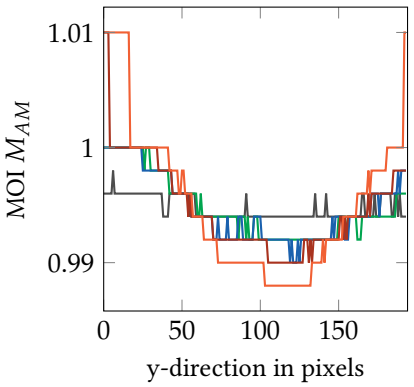

(f) MOI M_A with $T_{ref} = T_{Average}$ for each row at 1 C discharge.

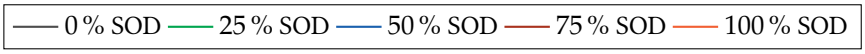

Figure 54: 1-dimensional inhomogeneity $M_{A(M)}$ in x and y direction of a 40 Ah pouch cell at different SODs for 1 C discharge based on the IR images from Fig. 56 with x^2 being the amount of pixels in each direction respectively.

5.3 CONCLUSION OF MOI

In this chapter, different measures to quantify inhomogeneity from literature have been investigated regarding their suitability for quantifying temperature inhomogeneity in lithium ion cells.

This includes basic measures like the average value with standard deviation, minimum-maximum investigations as well as more sophisticated methods like entropical measures or grid-based methods utilizing weighted average.

Based on the advantages and disadvantages from the described values, a new method is then developed that uses the Arrhenius function as a basis and uses the minimum temperature at each measurement time as reference temperature. The resulting value corresponds to the life-time reduction that a cell would experience, if it would be calendar aged at the specific inhomogeneous distribution. A weighting factor is introduced that allows a good estimation of the inhomogeneity if only a few temperature values from a cell surface are known. In the next chapter this will be further addressed and based on measurements evaluated.

6

TEMPERATURE INHOMOGENEITY MEASUREMENTS

Different possibilities of temperature and temperature inhomogeneity detection have been discussed before. To underline the suitability of the previously defined MOI however, different measurements are considered in the following.

6.1 INFRARED IMAGING

Infrared imaging is a reliable method to gain detailed surface temperature data of heated objects. In the following, measurements on a 40 Ah high energy pouch cell are described, using this method. The cell has a size of 225 mm × 225 mm × 9.9 mm and both tabs with a width of 80 mm at the same side. To avoid any reflection of the aluminum surface and therewith falsification of the measurement data, the cell is covered with a thin layer of black mat lacquer. The cell was put laying on an acrylic cell holder that covers the edges of the cell and allows therewith natural convection on the top of the cell and partially also on the bottom of the cell. The cell is then cycled with 1 C CC/CV charge with a cut-off current of 2 A followed by 1 h pause and different discharge rates. A maximum discharge rate of 8 C is chosen according to the cell specification. Fig. 56 shows the resulting images for 1 C and 8 C respectively at different SODs. The dimensions in x- and y-direction are given in pixels.

When comparing these images, it is obvious that inhomogeneities are higher for higher C-rates. While during the 1 C discharge the cell heats up pretty evenly with a temperature minimum near the terminals, a clear temperature maximum is visible at the negative terminal for the 8 C discharge.

A phenomenon that becomes even more obvious through these images is that at 25 %SOD the cell temperature increased already by 2 K compared to the idle state for the cell discharged with 1 C, while in the cell discharged with 8 C the temperature at this SOD did not change. This can be attributed to the time delay in the heating process, and different time frames that both discharges require. The delay is caused by the thermal capacity and heat conductivity, that is introduced in (16) and (17). While during 1 C discharge, the cell experienced a constant load for already 15 min at this SOD, the cell discharged with 8 C is only loaded for less than 2 min.

The temperature distribution development becomes even clearer when looking at Fig. 55. In these figures, the temperature distribution of said pouch cell is displayed for a 1 C and a 8 C discharge. Data are taken from the pixel-values of the infrared images in Fig. 56 . In the beginning of both discharges, temperature values show a Gaussian distribution and a gradient of only 0.5 K. This is probably caused by measurement noise. To better see the values for higher discharge states, the y-axis of the 8 C diagram Fig. 55b has been shortened to an amount of 1000 as the distribution is very similar to the 1 C discharge in this area.

As already visible in the IR images, the distribution for 0 % and 25 % SOD is almost identical for this high C-rate. While the peak of the distribution for 1 C is shifted further to the right for higher SODs and the spread reaches 2.5 K, the distribution for 8 C seems to be more Gaussian even at higher SODs but with a spread of almost 20 K. This becomes clear in the detailed view of the 100 % SOD in Fig. 55b.

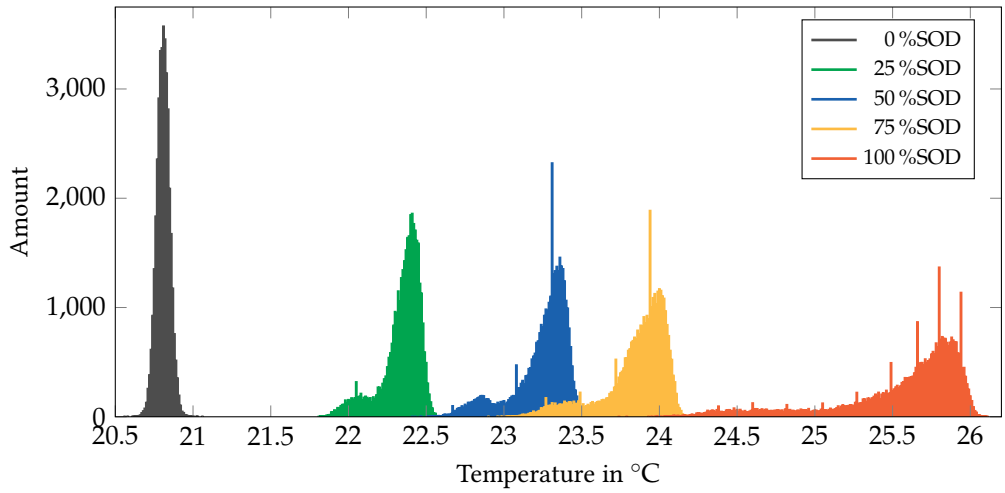

(a) Temperature distribution during 1 C discharge with a clear shift of the maximum towards the right.

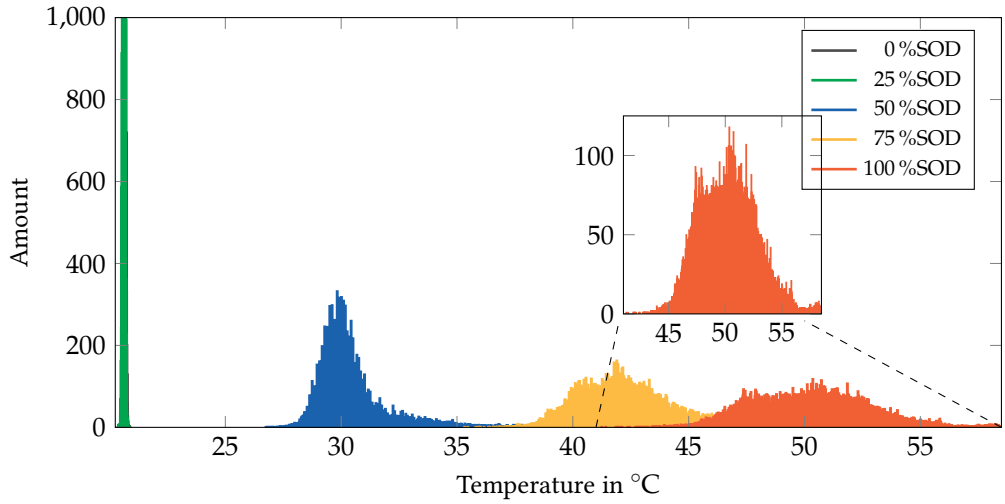

(b) Temperature distribution during 8 C discharge with congruent data during 0 % and 25 % SOD and a Gaussian-like distribution even at high SODs.

Figure 55: Temperature distribution in a 40 Ah pouch cell during 1 C and 8 C discharge at different SODs.

While infrared images provide a good insight in the surface temperature distribution, this method does not allow to get any information on in-cell inhomogeneities. Additionally, since the cameras are bulky and expensive, only laboratory investigations can be done with this method. For real-time monitoring during operation sensing with touching temperature probes is inevitable.

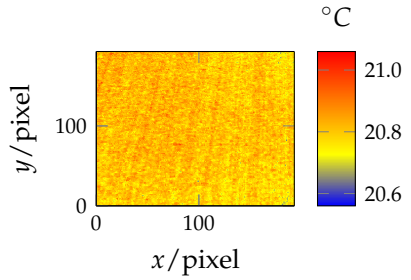

(a) 1C discharge at 0 % SOD, $T_{Av} = 20.81\,°C$

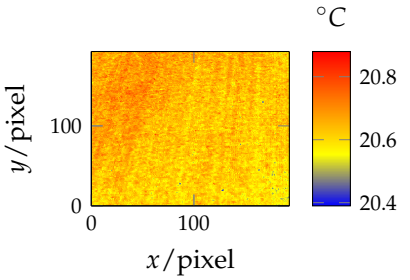

(b) 8C discharge at 0 % SOD, $T_{Av} = 20.64\,°C$

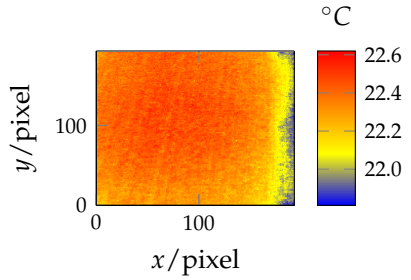

(c) 1C discharge at 25 % SOD, $T_{Av} = 22.34\,°C$

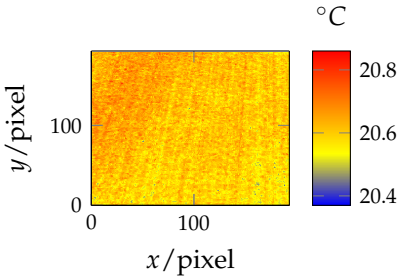

(d) 8C discharge at 25 % SOD, $T_{Av} = 20.61\,°C$

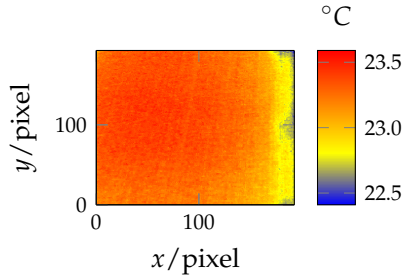

(e) 1C discharge at 50 % SOD, $T_{Av} = 23.24\,°C$

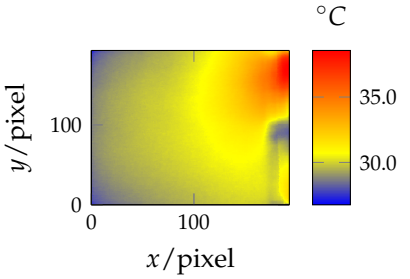

(f) 8C discharge at 50 % SOD, $T_{Av} = 30.42\,°C$

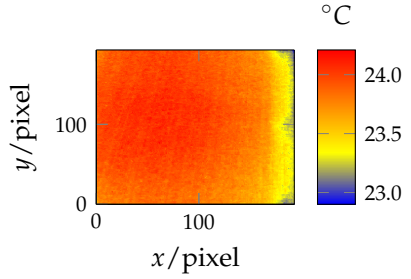

(g) 1C discharge at 75 % SOD, $T_{Av} = 23.85\,°C$

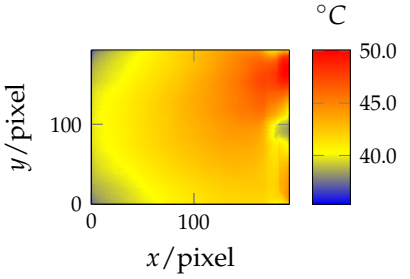

(h) 8C discharge at 75 % SOD, $T_{Av} = 42.30\,°C$

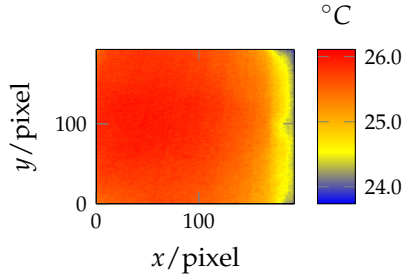

(i) 1C discharge at 100 % SOD, $T_{Av} = 25.56\,°C$

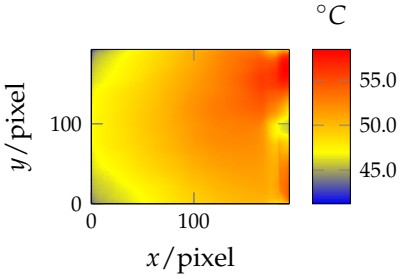

(j) 8C discharge at 100 % SOD, $T_{Av} = 50.28\,°C$

Figure 56: Infrared images of a 40 Ah pouch cell at different SODs discharged with 1 C (left) and 8 C (right). The tabs of the pouch cell are located on the right side of the pictures with the anode tap on the bottom.

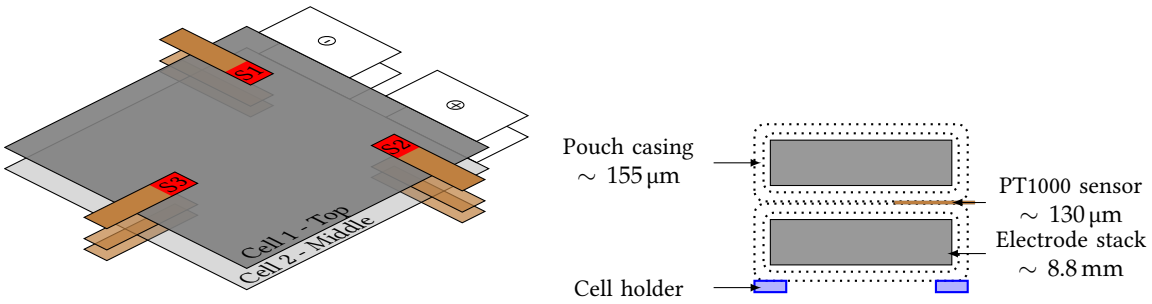

(a) On-site to the setup of cell sandwich with sensor positions and the sensing area marked in red.

(b) Sectional drawing of the cell sandwich.

Figure 57: Setup of cell sandwich.

6.2 CELL SANDWICH MEASUREMENTS

Since measurements with sensors integrated in cells are very challenging as elaborated before, an approximative method is used to estimate the temperature gradients in z-direction of a cell. With sensor arrays on the cell's surface or with the help of infrared imaging, in-plane temperature gradients can be investigated and based on that, cooling systems or sensing points optimized. What lacks from all these measuring methods is the information how the heat propagates from the inside of a cell to the outside and how internal hot-spots can be detected with only surface measurements. To investigate the time delays between the emergence of heat inside the cell and the detection of this heat on the surface as well as the arising temperature gradients, the following setup has been used.

Two 40 Ah cells, as described in Section 6.1, were connected in parallel and stacked onto each other in a cell sandwich. For this purpose the cells with the sensors in between have been closely fixed together with tape. On each layer, three thin-film *PT1000* foil sensors from *Heinz Meßwiderstände* were placed next to each terminal and at the opposite side of the terminals, as shown in Fig. 57. The dimensions of the pouch laminate can be taken from Fig. 3. With this method an estimation of the temperature gradients in z-direction of a cell can be made since the radiation and convection which normally takes place at the surface of a cell and contributes to cooling at the sensing point can be omitted between the sandwich. The method can not fully resemble the measurements of a in-situ sensor since an additional time delay caused by the thermal resistance of the pouch laminate has to be taken into account. A quantitative approximation of the gradients which occur in a cell can nevertheless be made.

To receive information about the gradients at the three sensing points in each layer, the cells were cycled with 1 C charge and different discharge rates at room temperature. The cell sandwich was placed onto an acrylic cell holder. A picture of this cell holder is given in Fig. 58.

Figs. 59a and 59b show the results for 8 C and 1 C discharge in comparison to the SOD over time. Fig. 59c depicts the same distribution for the charge phase over SOC. Table 8 presents the maximum temperature values at each sensor and the corresponding elapsed time of the discharge or charge respectively. In Fig. 59b and Fig. 59c a small offset of 0.5 °C in the beginning of the measurement can be seen between the sensors on the top of the cell and the sensors on the bottom and in the middle of the sandwich respectively. This can be attributed to manufacturing variances of the sensor which can be in the range of up to 0.6 °C according to *DIN EN 60751*.

It is obvious that the temperatures at the bottom of the cell sandwich are significantly lower than between the cells and on top of the cells especially for 8 C discharge. This is attributable to the conductive cooling effect of the cell holder on which the cell stack was placed. The sensors between the cell stack detected the highest temperatures. The in-plane temperature gradient is thereby around 5.7 K for both top of the cells and between the cells, while it is with 10 K significantly larger

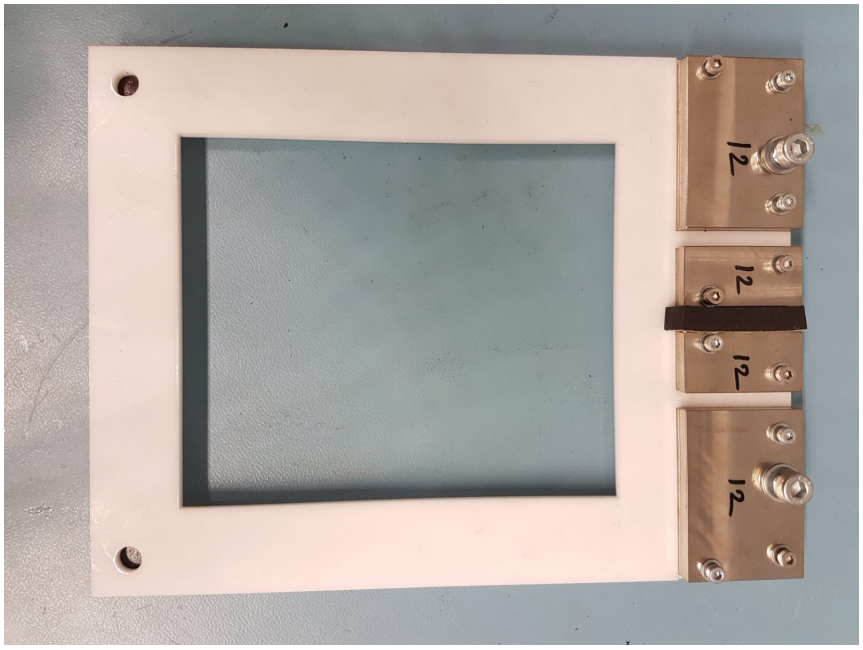

Figure 58: Cell holder for the 40 Ah cell used in the cell sandwich setup.

at the bottom of the cell during 8 C discharge. The warmest area was measured near the cathode tab at the top and middle layer. On the bottom, the hot spot was shifted to the side opposite of the tabs, which was the coolest area on the other layers.

The qualitative temperature distribution is similar for 1 C discharge. The in-plane gradients are however with less than 3 K significantly smaller. During 1 C charge these gradients are even below 2 K.

The through-cell temperature gradients vary between 1.7 K and 6.7 K between top and middle layer depending on the sensor position for 8 C discharge. Between bottom and middle layer these gradients are between 18.3 K and 34.1 K. Also the through-plane gradients are obivously significantly smaller for 1 C discharge and charge. Between top and middle layer they are below 0.8 K for discharge and below 0.5 K for charge respectively. The through-plane gradient between middle and bottom layer is with a maximum of 5.3 K (discharge) and 3.5 K (charge) again higher.

The bottom sensors detected the temperature maximum near the tabs earliest. The in-plane time difference between the temperature maxima is 9 s, 5 s and 36 s for top, middle and bottom sensors. The through-cell time difference between the detection of temperature maxima is between 2 s and 4 s between the middle and top layer while it is significantly bigger between 4 s and 17 s between middle and bottom layer.

Also for the time delay for detecting maxima, the 1 C discharge shows significantly lower values of maximum 6 s in-plane. Through plane however delivers higher time delays of up to 12 s between middle and bottom layer. The charge shows even higher discrepancies, which however are mainly caused by jittering of the signal within the the flat maximum and therefore provide false maxima. When looking at the temperature curve in Fig. 59c, no significant time shift is visible.

In [71] it was already referred to "research activities presented by [88]" that pointed out the biggest benefit of in-situ measurements during abuse scenarios. Also space-resolved temperature monitoring is presented therein as crucial in order to "detect critical hotspots and undesired temperature gradients."[71] The simulation results presented in Fig. 22 show evidence thereof. However the underlying cell was small with only 2 Ah. As expected, gradients in large-size cells like the 40 Ah cells used in the cell sandwich show much larger gradients in all directions.

From the results of the sandwich measurements the thermal behavior of a single pouch cell during normal operation can be estimated. The values from the top of the cell go well along with the IR measurements from Section 6.1. The cooling effect on the bottom of the cell can also be estimated to be the same as here in the cell sandwich. The temperature gradients in through-cell direction can therefore be estimated to be in the same range, the time difference can be assumed to be roughly halved according to (13) and (16). This shows that for detecting the exact temperature, in-cell measurement is a clear advantage. If only temperature rise is to be detected, in-situ measurement does not have a significant time-advantage compared to a sensor on the surface of an un-cooled cell. It does have an advantage of up to 8 s compared to surface sensors on a passively cooled cell though, depending on the C-rate. This time advantage rises especially if cooling systems on the cell surface are applied. This can already be seen from the passive cooling by the cell holder on the bottom of the cell and becomes more significant if active cooling systems are introduced. This leads to the possibility of detecting temperature maxima or hot-spots in the cell that cannot be detected on the surface. In a battery system the BMS normally shuts off at a certain temperature limit (e.g. 50 °C) to prevent the cell from damages. When looking at the temperature diagrams from the 8 C discharge on the cell sandwich in Fig. 59 it can be seen that it takes almost 100 s more until this threshold value can be detected on the surface compared to the sensors in the middle of the sandwich. Even more significant is the fact that on the passively cooled bottom surface, the temperature limit is never reached. Depending how the temperature shut-off limit is chosen this can, in case of surface sensors on a cooled cell, lead to a fatal mis-measurement and damage to the cell in the long run. An in-situ sensor is therefor of big advantage.

Table 8: Maximum temperatures measured at sensors in a cell sandwich of two parallel 40 Ah pouch cells and corresponding elapsed time during charge and discharge.

Position	Discharge / charge rate	Parameter	Top of cell	Between cells	Bottom of cell
Near Anode Tab (S1)	8C discharge	$T/°C$	61.248	62.977	39.017
		t/s	455	453	449
	1C discharge	$T/°C$	25.071	24.740	20.910
		t/s	3522	3525	3534
	1C charge	$T/°C$	23.035	22.570	20.287
		t/s	2858	2967	2826
Near Cathode Tab (S2)	8C discharge	$T/°C$	62.769	69.501	35.442
		t/s	452	452	435
	1C discharge	$T/°C$	24.925	25.589	20.222
		t/s	3522	3523	3535
	1C charge	$T/°C$	22.959	23.366	19.85
		t/s	2862	2932	3152
Opposite Tabs (S3)	8C discharge	$T/°C$	57.042	63.803	45.517
		t/s	461	457	471
	1C discharge	$T/°C$	25.264	26.057	22.95
		t/s	3526	3527	3529
	1C charge	$T/°C$	23.161	23.604	21.625
		t/s	2863	2949	2823

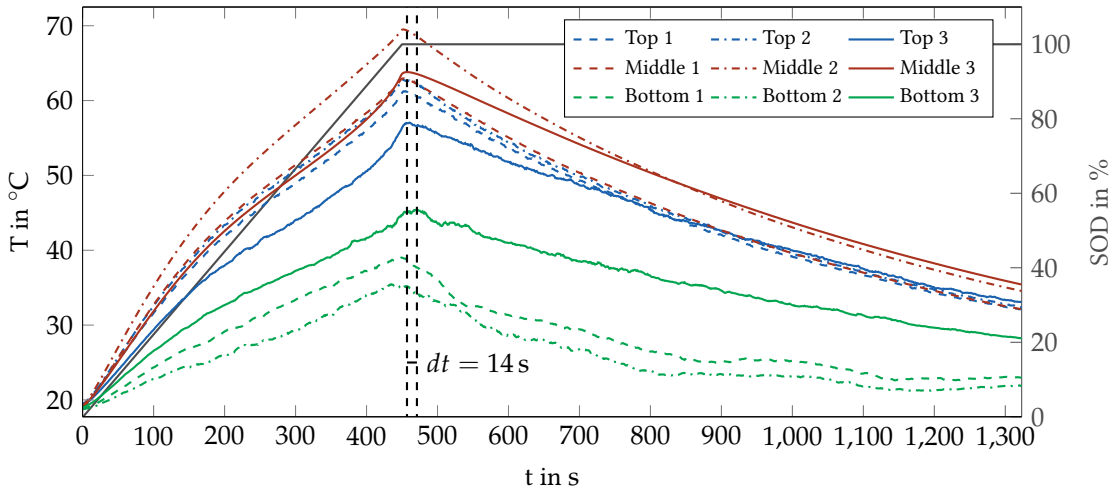

(a) Temperature measurements and SOD development over time of the cell sandwich at 8 C discharge.

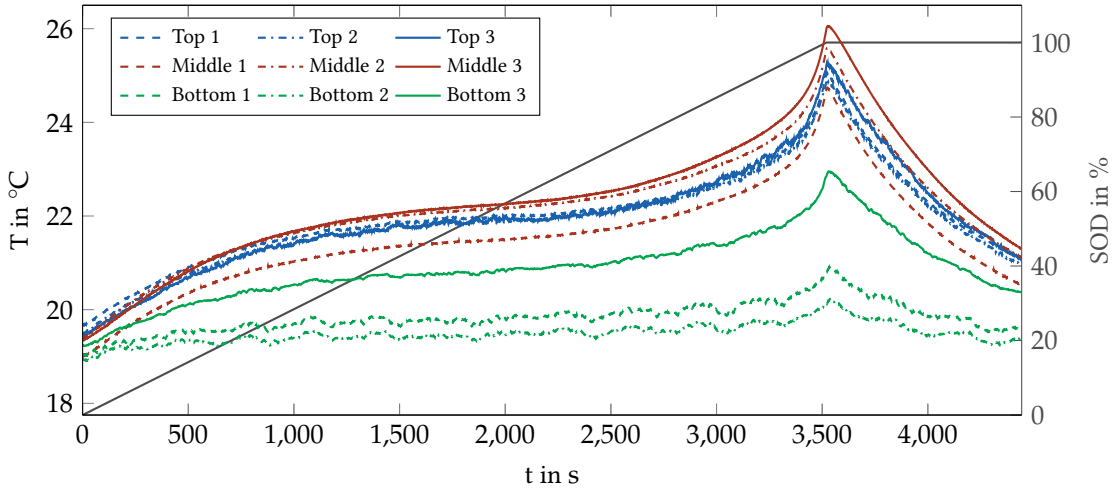

(b) Temperature measurements and SOD development over time of the cell sandwich at 1 C discharge.

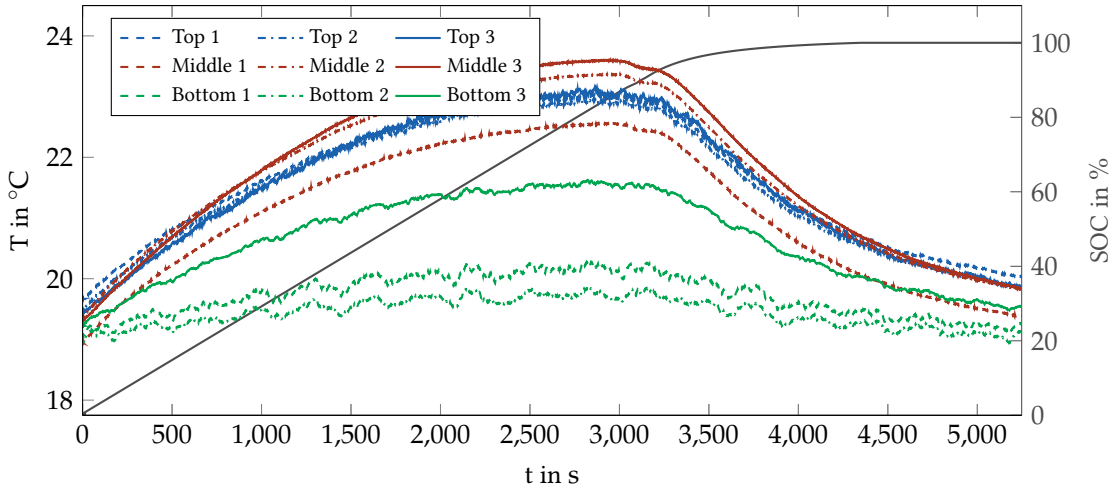

(c) Temperature measurements and SOC development over time of the cell sandwich at 1 C charge.

Figure 59: Temperatures measured in cell sandwich and at the surface of the cells at different discharge and charge rates.

6.3 CONCLUSION OF MEASUREMENTS

In this chapter, methods to estimate the inhomogeneity in a full cell are described. On the one hand, to understand the temperature distribution in plane in the cell, infrared measurements are therefore researched. For through-plane investigations on the other hand, a cell sandwich consisting of two pouch cells has been evaluated.

The results show that the degree of inhomogeneity depends on the C-rate as well as on the elapsed time during a discharge. While for lower currents the hot-spot is at the opposite of the cell tabs throughout the whole discharge with a stronger influence of the heat dissipation by the tabs, it propagates for higher currents from the cathode tab towards a more equally distributed heat maximum close to both tabs. In this case the bottle neck of the tabs where the current has to get through weighs more than the heat dissipation of the tabs. From the cell sandwich the necessity of in-cell measurements becomes obvious especially when cooling is applied to the cell. While the top surface was only exposed to thermal radiation and natural convection to the air, the bottom cell experienced passive cooling through the cell holder. In the middle of the sandwich only thermal conduction takes place. The results show that especially between the cooled bottom and the middle, the gradients are significant and for a temperature threshold of 50 °C the time delay can be up to 100 s between the middle and the top, while this threshold is never reached on the bottom. The time delay for reaching the maximum temperature is still 14 s as illustrated in Fig. 59a. For a temperature based safety shut-off this effect is significant and shows the necessity of in-cell measurements.

7

RESULTS

In this chapter distributed temperature measurements from IR and cell-sandwich data are analyzed with the help of the previously defined MOI. The gained knowledge from this analysis is used to investigate the optimal positioning of cell-sensors on the surface and whether, based on that, an estimation of the real cell temperature distribution is possible. Additionally, temperature data from a battery pack that is applied in the electric taxi *EVA* are analyzed with the help of the MOI.

7.1 EVALUATION OF THE INHOMOGENEITY MEASUREMENTS

For quantifying the results from the measurements in Chapter 6 and to be able to compare them, the previously defined MOI M_{AM} is applied on the data according to (81) where the minimum temperature is taken as reference. Figs. 60 and 61 show the results for 8 C and 1 C discharge with $x^2 = 3$ the amount of measurement points and T_{min} being the minimum temperature at each layer for each time step. The total inhomogeneity is calculated in the same manner as in the area according to Eq. (81) but with the overall minimum temperature from all layers T_{min} and the amount of measurement points $x^2 = 9$. As mentioned before, values close to $M_{AM} = 1$ represent a homogeneous distribution, while lower values show evidence of larger temperature discrepancies. The reason why the measure doesn't reach 1 in the beginning of the discharge is the offset of the sensors which was mentioned in Section 6.2.

Looking at 8 C discharge in Fig. 60, in all three layers, the inhomogeneity increases with higher SODs with a maximum in the last quarter of the discharge process. While the maximum inhomogeneity $M_{AM,max,top} = 0.793$ on top of the cell is reached at 83 %SOD, it is already reached at 76 %SOD in the middle of the sandwich with $M_{AM,max,mid} = 0.865$ and finds its maximum on the bottom at the end of discharge $M_{AM,max,bot} = 0.779$. The overall inhomogeneity maximum in the whole sandwich is reached at 100 %SOD with $M_{AM,max} = 0.397$.

During 1 C discharge, the behavior is slightly different. The corresponding diagram is shown in Fig. 61. Here, the top of the cell shows almost no inhomogeneity with $M_{AM,max,top} = 0.99$, while it is slightly bigger with a maximum of $M_{AM,max,mid} = 0.953$ and $M_{AM,max,bot} = 0.926$ for the middle and bottom layer respectively. The overall inhomogeneity reaches $M_{AM,max} = 0.778$ for 1 C discharge and is therewith significantly smaller than for higher C-rates. All inhomogeneity maxima for the 1 C discharge are reached at 100 % SOD. In Fig. 53 the MOI for 1 C discharge based on IR measurements was already displayed. The tendency is similar to that in Fig. 61 with an increasing inhomogeneity over SOD. The maximum inhomogeneity detected here is however $M_{AM,max,top} = 0.884$ at the end of discharge and therewith significantly higher than that detected by sensors in a cell sandwich. The reason is, that through IR data the full surface is reflected instead of only three selected points. In the next section, a discussion will follow, how this can be specifically addressed.

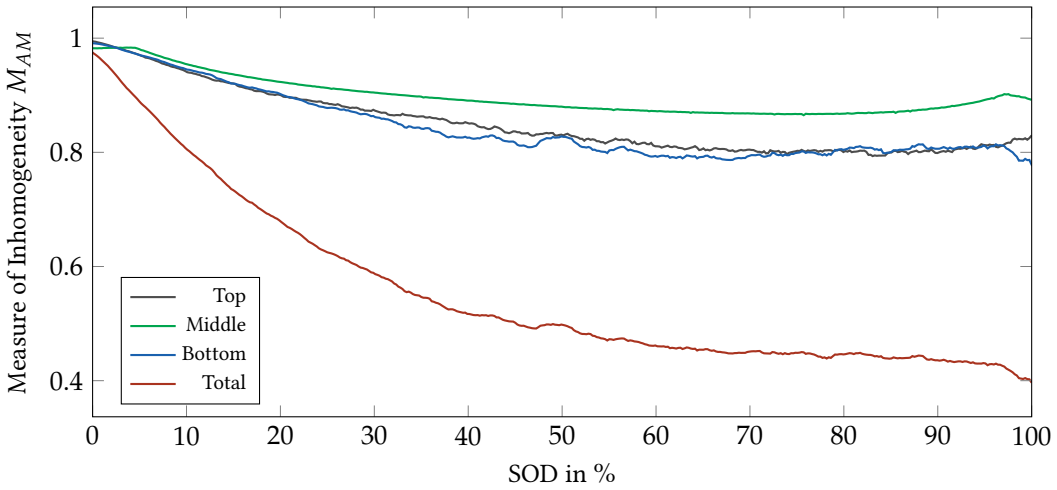

Figure 60: MOI M_{AM} for the cell sandwich during 8 C discharge based on three sensors per layer.

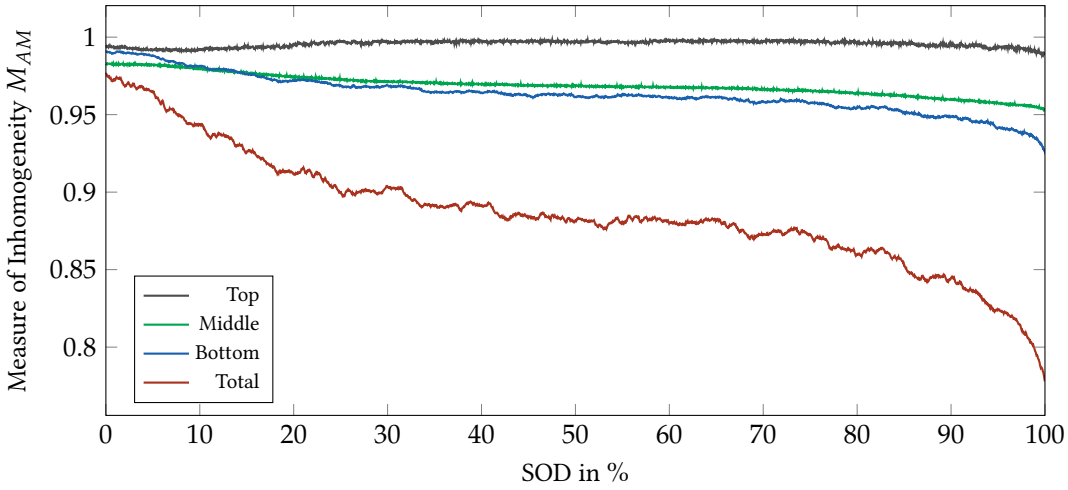

Figure 61: MOI M_{AM} for the cell sandwich during 1 C discharge based on three sensors per layer.

7.2 PLACEMENT OF SENSORS

As mentioned initially the temperature inhomogeneity depends on various factors like cell shape, cycling rate, placement, cooling systems, cell capacity and many more. To gain information about the real in-cell temperature, in-situ measurement is of big advantage. Multiple reasons why the integration especially of multiple sensors is challenging have been stated before. The cell sandwich measurements from Section 6.2 in combination with the IR measurements from Section 6.1 however provide valuable information on a reasonable sensor positioning.

As the IR images in Fig. 56 illustrated, the position of minimum and maximum values depends on the cycle rate as well as on the SOD. While at lower charging and discharging rates the cell tabs serve as heat sinks, the bottle neck near the tabs leads to a higher heating in this area at higher C-rates. On the opposite site of the cell tabs, the temperature distribution is rather symmetrical. To get full information about the inhomogeneity on the cell surface it is therefore suggested to place four sensors on the cell: On the hottest point, on the coldest point and to where the average temperature is mostly present. The latter is best approximated with a measurement point in the center of the cell, while the temperature extrema are - depending whether the cell is charged or discharged and

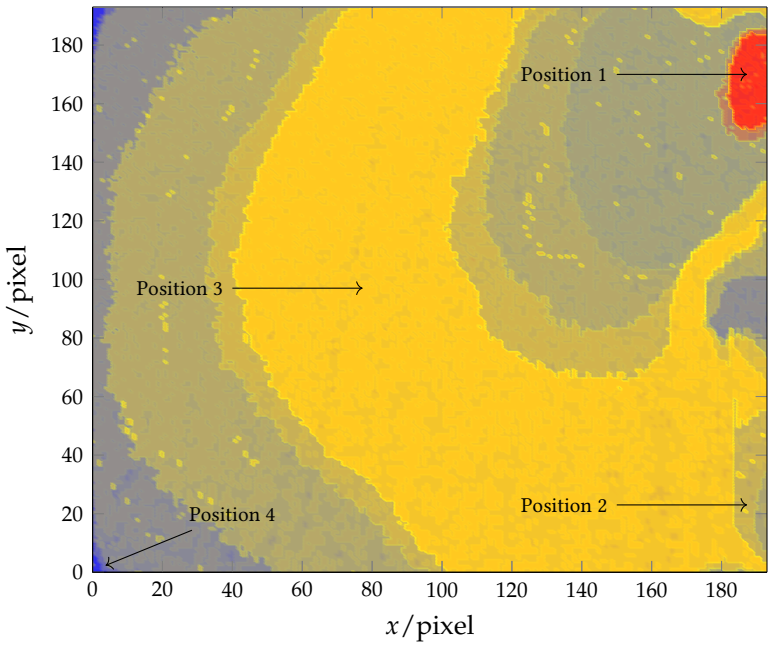

Figure 62: Temperature distribution chart with the area of maximum values in red, the area of average values in orange and that of minimum values in blue superimposed for 25 %, 50 %, 75 % and 100 %SOD for a 8C discharge. The anode tab is on the right bottom side near position 2.

in correspondence to the C-rate near the tabs and at the very edge of the cell on the opposite site. Fig. 62 shows a chart where the areas of minimum, average and maximum temperature at different SODs are superimposed to get a full picture of the behavior of the cell during a whole discharge cycle. Therefore the area with maximum temperature in red and the areas with average value in yellow during 8 C discharge at 25 %, 50 %, 75 % and 100 % SOD of the 40 Ah cell. The areas with minimum temperature are rather small in the edges in blue. The suggested positions are, based on that, marked in the figure.

With these measurement points and a suitable weighing factor, $M_{AM,w,max,top} = 0.9015$ could be detected. It is close to that calculated from the full IR data. The average value was weighted with a weighing factor of 500 as described in Section 5.2 compared to the other measurement points, to reach this result. Fig. 63 presents these values in comparison to those from the infrared image for 1 C discharge.

When looking at the through-plane data based on the cell-sandwich measurements from Section 6.2, it is obvious that the highest temperatures are detectable between the cells, since there the cooling effects from the surrounding air or from cooling media is lowest. For this reason, if used in a cell stack or module, the sensors should be placed between two cells to gain the best possible information. From the temperature distribution chart in Fig. 62, where the maximum, average and minimum areas through a whole discharge are displayed, the necessary position of sensors in the plane can be derived. To get a reasonable picture of the cell inhomogeneity and to be able to detect hot spots, four sensors, two near the cell tabs, one at the area of average temperatures and one at the opposite site of the cell tabs close to the corner is suggested.

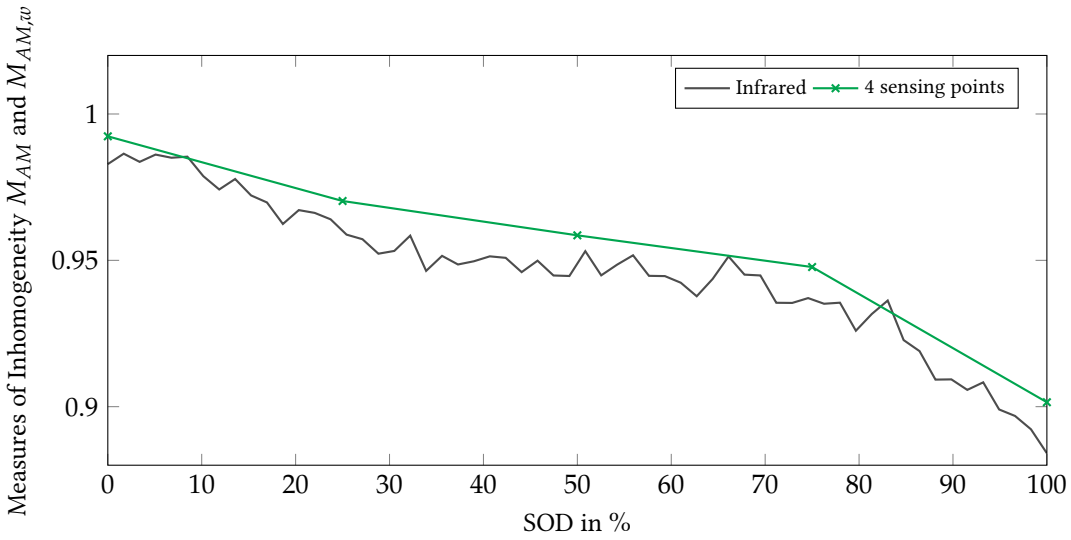

Figure 63: Measure of inhomogeneity from infrared measurements in comparison to weighted sensor measurements at 1 C discharge.

The gained information can be used to place sensors properly in a battery module or pack in order to monitor the temperature distribution best and to adjust cooling mechanisms properly. In *TUM CREATE* the battery pack shown in Fig. 64 has been designed for the usage in an electric taxi *EVA*. The pack consisted of 216 63 Ah pouch cells from *KOKAM* which used the same chemistry and basic conditions as the 40 Ah cells described before. In the pack always 2 cells were connected in parallel and 108 of those parallel modules have been connected in series. Between each of the cell sandwiches, researchers placed one PT1000 sensor right in the middle of the cell, where the average temperature of both cells could be detected.

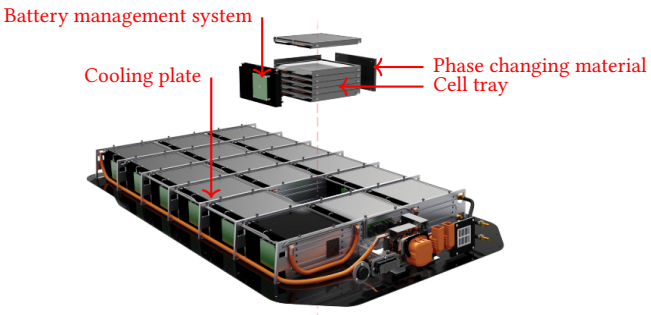

Figure 64: *EVA* battery pack setup according to [2].

A fast charging test was performed, where the pack was charged with almost 3 C to 67 % SOC. The design of the pack is displayed in Fig. 64. The cooling liquid is pumped through cooling plates which are directly connected to metal trays, where the cells are placed. Between the cells and the trays, and between the trays and the cooling plates, a thermally conducting polymer is applied to ensure the thermal connection. On the opposite side of the cell connectors, a phase changing material is attached to provide additional cooling. For the fast charging experiment, the pack was placed into a climate chamber and kept at 32 °C environmental temperature. The cooling liquid

was pre-cooled to 10 °C to maintain a reliable temperature. During the experiment, the temperatures are measured on each of the 108 cell pairs with one sensor per cell pair. Fig. 65 shows the minimum and maximum temperature in the pack and the measure of inhomogeneity. The MOI is calculated again according to Eq. (81) with $x^2 = 108$ the amount of cells in the pack and T_{min} being the minimum temperature in the whole pack at each SOC step. With a rising SOC, the temperature spread gets wider despite the cooling system and the inhomogeneity increases massively from $M_{AM,min} = 0.367$ at 5 % SOC to $M_{AM,max} = 0.016$ at 66.7 % SOC. The comparably large inhomogeneity already at 5 % SOC along with the strong jitter are probably caused by the cooling medium which flows along the sensing positions and does not equally dissipate the heat from all cells at the same time. Therefore the inhomogeneity at the cells is not correctly measured. A countermeasure for receiving more reliable data and also to reduce the jitter could be to place the sensors between two cells on the non-cooled surface, as suggested in Section 7.2.

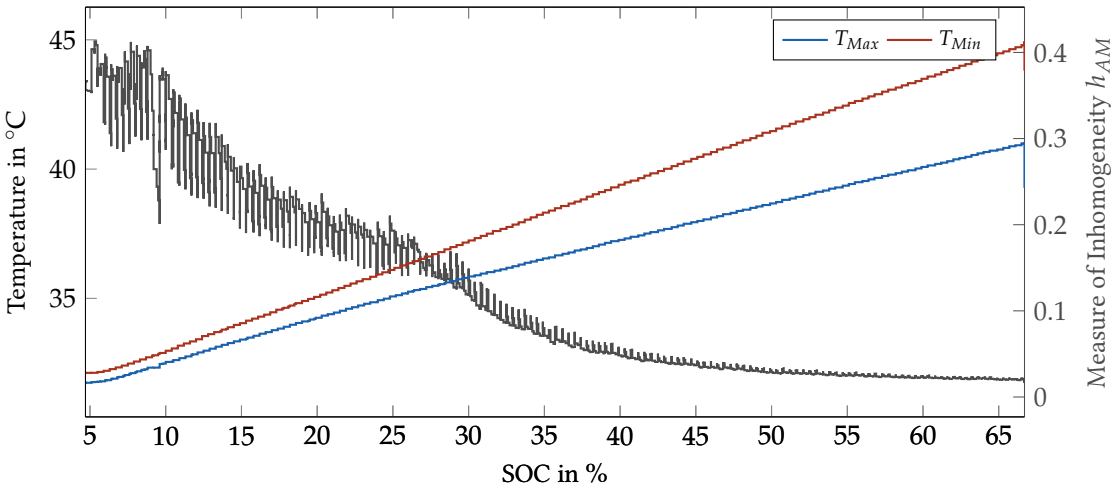

Figure 65: Minimum and maximum temperature in the *EVA* battery pack during 3 C fast charging along with the MOI for the battery pack.

7.4 CONCLUSION OF RESULTS

In this chapter, results from different experiments have been analyzed. On the one hand the previously discussed cell sandwich and infrared measurements have been evaluated. Based on that it was elaborated, where sensors should be preferably placed to be able to calculate the MOI even when only a small amount of sensors is used. A good correlation with data from more detailed measurements is present.

On the other hand, inhomogeneity of temperature in a battery pack is investigated during fast charging. Although simulations suggested the applied cooling method to provide a rather homogeneous temperature distribution, it is shown, that inhomogeneity within the pack is large and improvement here would be required.

8

CONCLUSION

Temperature plays an important role when dealing with Li-ion batteries. While low temperatures can lead to lithium plating and internal short circuits in the cell, higher temperatures deplete the lifetime of a cell significantly and can in the worst case cause a thermal runaway. Since during charging and discharging as well as due to different operation strategies like applied cooling the cells are not homogeneously heated, temperature inhomogeneity can be a similar limiting factor like overall high operating temperatures. Additionally, thermal hot spots can be an early indicator for failures in a cell.

8.1 SUMMARY

In this thesis the reasons for temperature inhomogeneity are extensively discussed. While external effects like the operation with cooling effects significantly influence the temperature distribution, mainly internal mechanisms are identified to cause these discrepancies: cycling, cell shape and also production impurities. Vice-versa, temperature inhomogeneity and hot spots can lead to or indicate safety risks, accelerated aging and local state of charge and current density peaks.

To determine the exact nature of inhomogeneities and how they can be detected, temperature dependent cell parameters are researched. However, the temperature dependency of most of these parameters is rather linear and therefore do not present good options for inhomogeneity detection. For those that provide non-linearity, the effect of temperature hot spots is too insignificant to make the parameters suitable.

For this reason various temperature sensing options mainly for in-situ monitoring are investigated. While all described analogue solutions have to deal with the problem of having to seal cables into the cell casing, the last suggested digital solution provides a promising solution. All data are collected digitally and sent through the cell casing with the help of capacitive coupling. By using capacitive coupling, wiring through the cell casing is omitted. Using a digital transmission scheme and corresponding components, reliable and fast data transfers of multiple temperature sensors are provided. In detail, the communication protocol as well as a hardware setup for proof of concept are discussed.

A major feature of the described pouch cells is that they can be designed in many different shapes to meat the application requirements. It however makes it difficult to compare the temperature distributions of different cells with each other. For this reason, a measure of inhomogeneity based on the Arrhenius equation is defined to quantify the inhomogeneity and how it influences the cell's performance.

Measurements from infrared images as well as from sensors in a cell sandwich are taken into account and analyzed with the help of this MOI. Suggestions of where sensors are ideally to be placed to gain the best possible impression of the temperature distribution with the least possible amount of sensors are developed based on that.

Finally, data from a battery pack are analyzed with the same method, showing that, even though the present cooling mechanism was carefully developed based on simulation data, improvements can still be done.

8.2 CHALLENGES AND FUTURE WORK

While this thesis presents approaches on how to estimate and quantify temperature inhomogeneities, some challenges still need to be addressed in future work. In the following it is discussed, which topics will be dealt with and how enhancements in future can take place.

8.2.1 *Digital measurement for in-situ sensing*

In Section 4.9.2 a prototype system is designed that proves the principle of data communication through a soft casing of a pouch cell by capacitive coupling. The described system is made of bulk components and not yet suitable for the integration into actual cells. Considerations about miniaturization and the integration into one single chip are given. In a next step, these considerations need to be taken into account and a next step towards miniaturization done. Due to the bulkiness of the described system, tests in the cell environment have not been performed within the scope of this thesis. A verification of the functionality of the data transmission system during cell operation is still pending. Since the described data transfer method provides a very small likelihood of errors, a stable data processing is expected though.

The system is so far only tested for pouch cell casings. Therefore, a conceptual hardware test for other cell casings is desirable to make the presented system suitable for all cell types.

8.2.2 *Verification of MOI*

A Measure of Inhomogeneity (MOI) is proposed that quantifies inhomogeneity in temperature distributions in order to make different cells comparable. Based on this comparison it helps to better design operating and cooling strategies. In the thesis at hand, the designed measure is applied to one specific cell type. Suggestions for measurement point reduction are made and it is shown that the resulting measure still provides significant information about the deviation of the temperature distribution from homogeneity. The measure provided is well suitable for comparison of different cells from the same type. To prove the universality of this measure also for other cell types like cylindrical or hard-case cells and for other chemistries, further investigations are desirable.

8.2.3 *Implementation of MOI and Digital System in BMS*

As a last step the developed digital temperature measurement system as well as the calculation of MOI needs to be implemented into a Battery Management System (BMS). By this, the current temperature distribution in each cell of a battery pack can be analyzed and the operation of each individual cell adjusted such that a homogeneous temperature distribution is secured while providing the necessary power. By analyzing and optimizing the MOI in addition to the minimum and maximum temperature values in a pack, cooling strategies can be improved and help to improve fast-charging behavior as well as optimize the lifetime of the whole pack. Hot spots can be detected and systematically dealt with by applying countermeasures. Failures can be detected earlier and single cells switched off before a irreversible event happens. By this minimization of aging and hence a longer overall lifetime of the whole pack can be reached.

A

APPENDICES

A.1 USED BATTERY CELLS

Table 9: Cells used within this thesis with basic parameters and sections of appearance.

Cell	Chemistry	$\frac{C_N}{\mathrm{Ah}}$	$\frac{W \times L \times H}{\mathrm{mm}^3}$	$\frac{V_{min}}{\mathrm{V}}$	$\frac{V_{max}}{\mathrm{V}}$	$\frac{I_{max,DC}}{\mathrm{A}}$	$\frac{I_{max,C}}{\mathrm{A}}$	Sections
XALT 40 High Power, Kokam	NMC-C	40	$225 \times 225 \times 9.9$	2.7	4.2	320	120	6.1,6.2
XALT 40 High Power, Kokam	NMC-C	63	$268 \times 265 \times 11$	2.7	4.2	504	N/A	7
SPB7668130 B1, Enertech	NMC+LMO - C	6	$68 \times 130 \times 7.6$	3.0	4.2	72	18	3.1,3.4
SPB605060, Enertech	LCO-C/Polymer	2.0	$60 \times 50 \times 6$	3.0	4.2	4.0	2.0	4.7,4.2
APR18650M1A, A123	LFP-C	1.1	18650	2	3.6	30	4	3.3
IFR13N0-SP1100-08, PHET	LFP-C	1.05	18650	2	3.65	10	2	3.3
IFR18650-09K(C), PHET	LFP-LTO	1	18650	1.1	2.4	5	10	3.3

A.1 USED BATTERY CELLS

BIBLIOGRAPHY

[1] Aircraft serious incident investigation report. Japan Transport Safety Board, 2014.

[2] www.eva-taxi.sg, 2016.

[3] S. T. Ali, J. Lebaek, L. P. Nielsen, C. Mathiasen, P. Moller, and S. K. Kaer. Thin film thermocouples for in situ membrane electrode assembly temperature measurements in a polybenzimidazole-based high temperature proton exchange membrane unit cell. *Journal of Power Sources*, 195(15):4835–4841, 2010.

[4] Analog Devices, Inc. ADT7310 datasheet: 16-Bit Digital SPI Temperature Sensor, 2011.

[5] Analog Devices, Inc. ADT7312 datasheet: Automotive, $\pm$ 1 $^{\circ}$ C Accurate, 16-Bit, 175 $^{\circ}$ C, Digital SPI Temperature Sensor in Die Form, 2012.

[6] R. Arunachala, S. Arnold, L. Moraleja, T. Pixis, A. Jossen, and J. Garche. Influence of cell size on performance of lithium ion battery. In *Presentation at Kraftwerk Batterie, Muenster, Germany*, 2015.

[7] P. Balakrishnan, R. Ramesh, and T. P. Kumar. Safety mechanisms in lithium-ion batteries. *Journal of Power Sources*, 155:401–414, 2006.

[8] T. M. Bandhauer, S. Garimella, and T. F. Fuller. A critical review of thermal issues in lithium-ion batteries. *Journal of the*, 158(3):R1–R25, 2011.

[9] W. Bechmann and J. Schmidt. *Einstieg in die Physikalische Chemie*. Vieweg+Teubner, 4 edition, 2010.

[10] J. Belt, V. Utgikar, and I. Bloom. Calendar and PHEV cycle life aging of high-energy, lithium-ion cells containing blended spinel and layered-oxide cathodes. *Journal of Power Sources*, 196 (23):10213–10221, 2011. doi: 10.1016/j.jpowsour.2011.08.067.

[11] C. Birkl and D. Howey. Model identification and parameter estimation for LiFePO4 batteries. *Hybrid and Electric Vehicles Conference 2013 (HEVC 2013)*, 2013. doi: 10.1049/cp.2013.1889.

[12] J. O. Bockris and A. K. Reddy. *Modern Electrochemistry 2*. Plenum Press, 1970.

[13] M. Borenstein, L. V. Hedges, J. P. T. Higgins, and H. R. Rothstein. *Introduction to Meta-Analysis*. Wiley, 2009. Fixed-Effect Versus Random-Effects Models.

[14] M. Broussely, S. Herreyre, P. Biensan, P. Kasztejna, K. Nechev, and R. Staniewicz. Aging mechanism in li ion cells and calendar life predictions. *Journal of Power Sources*, 97:13–21, 2001.

[15] S. Buller, M. Thele, R. DeDoncker, and E. Karden. Impedance-based simulation models of supercapacitors and li-ion batteries for power electronic applications. *IEEE Transactions on Industry Applications*, 41(3):742–747, 2005. doi: 10.1109/tia.2005.847280.

[16] S. Buller. *Impedance-Based Simulation Models for Energy Storage Devices in Advanced Automotive Power Systems*. PhD thesis, Institut für Leistungselektronik und Elektrische Antriebe, RWTH Aachen University, 2003.

[17] J. Cannarella and C. B. Arnold. The effects of defects on localized plating in lithium-ion batteries. *Journal of the Electrochemical Society*, 162(7):A1365 – A1373, 2015. doi: 10.1149/2.1051507jes.

[18] K. L. Chopra. *Thin film phenomena*. McGraw-Hill, 1969.

[19] A. Czainski, Z. Garncarek, and R. Piasecki. Quantitative characterization of inhomogeneity in thin metallic films using Garncarek's method. *Journal of Physics D: Applied Physics*, 27(3): 616–622, 1994. doi: 10.1088/0022-3727/27/3/030.

[20] R. Deshpande, M. Verbrugge, Y.-T. Cheng, J. Wang, and P. Liu. Battery cycle life prediction with coupled chemical degradation and fatigue mechanics. *Journal of the Electrochemical Society*, 159(10):A1730 – A1738, 2012. doi: 10.1149/2.049210jes.

[21] W. Dreyer, J. Jamnik, C. Guhlke, R. Huth, J. Moskon, and M. Gaberscek. The thermodynamic origin of hysteresis in insertion batteries. *Nature Materials*, 2010.

[22] Dupont. Kapton mt - technical data sheet. `http://www.dupont.com/content/dam/dupont/products-and-services/membranes-and-films/polyimde-films/documents/DEC-Kapton-MT-datasheet.pdf`.

[23] F. Ebenkofler. Development of a thin film rtd sensor matrix for in situ temperature measurement in lithium ion pouch cells. Master's thesis, Technical University of Munich, 2014.

[24] M. Ecker, T. K. D. Tran, P. Dechent, S. Käbitz, A. Warnecke, and D. U. Sauer. Parameterization of a physico-chemical model of a lithium-ion battery: I. determination of parameters. *Journal of the Electrochemical Society*, 162(9):A1836–A1848, 2015. doi: 10.1149/2.0551509jes.

[25] M. Ecker, N. Nieto, S. Käbitz, J. Schmalstieg, H. Blanke, A. Warnecke, and D. U. Sauer. Calendar and cycle life study of Li(NiMnCo)O2-based 18650 lithium-ion batteries. *Journal of Power Sources*, 248:839–851, 2014. doi: 10.1016/j.jpowsour.2013.09.143.

[26] S. Elizabeth. *Standard-deviation - Unabridged Guide*. Emereo Publishing, 2012.

[27] T. Erdey-Grúz and M. Volmer. Zur theorie der wasserstoffüberspannung. *Zeitschrift für physikalische Chemie*, 150:203–213, 1930.

[28] S. V. Erhard, P. J. Osswald, J. Wilhelm, A. Rheinfeld, S. Kosch, and A. Jossen. Simulation and measurement of local potentials of modified commercial cylindrical cells. *Journal of The Electrochemical Society*, 162(14):A2707–A2719, 2015. doi: 10.1149/2.0431514jes.

[29] X. Feng, M. Fang, X. He, M. Ouyang, H. Lu, Languang anf Wang, and M. Zhang. Thermal runaway features of large format prismatic lithium ion battery using extended volume accelerating rate calorimetry. *Journal of Power Sources*, 255:294–301, 2014.

[30] M. Fleckenstein, O. Bohlen, M. A. Roscher, and B. Bäker. Current density and state of charge inhomogeneities in li-ion battery cells with lifepo4 as cathode material due to temperature gradients. *Journal of Power Sources*, 196(10):4769 – 4778, 2011. doi: 10.1016/j.jpowsour.2011.01.043.

[31] J. Fraden. *Handbook of modern sensors: physics, design and applications*. Springer, 3 edition, 2004.

[32] J. Fraden. *Handbook Of Modern Sensors - Physics, Designs, and Applications*. Springer, Third Edition, pp.59-66, 86-91, 461-464, 545-546, 548, 565, 2006.

[33] D. Gall. Electron mean free path in elemental metals. *Journal of Applied Physics*, 119(8): 085101, 2016. doi: 10.1063/1.4942216.

[34] Z. Garncarek and R. Piasecki. What is a physical measure of spatial inhomogeneity comparable to the mathematical approach? *The European Physical Journal Applied Physics*, 5(3): 243–249, 1999. doi: 10.1051/epjap:1999135.

[35] Z. Garncarek and J. Idzik. Degree of heterogeneity of thermal field a method of evaluation. *International Journal of Heat and Mass Transfer*, 35(11):2769–2775, 1992. doi: 10.1016/0017-9310(92)90297-6.

[36] Z. Garncarek, L. Przybylski, J. S. Botterill, J. Bridgwater, and C. J. Broadbent. A measure of the degree of inhomogeneity in a distribution and its application in characterising the particle circulation in a fluidized bed. *Powder Technology*, 80(3):221–225, 1994. doi: 10.1016/0032-5910(94)02858-3.

[37] J. Gerschler, F. Kirchhoff, H. Witzenhausen, F. Hust, and D. Sauer. Spatially resolved model for lithium-ion batteries for identifying and analyzing influences of inhomogeneous stress inside the cells. *2009 IEEE Vehicle Power and Propulsion Conference*, 2009. doi: 10.1109/vppc.2009.5289836.

[38] J. B. Gerschler. *Ortsaufgelöste Modellbildung von Lithium-Ionen-Systemen unter spezieller Berücksichtigung der Batteriealterung*. PhD thesis, RWTH Aachen, 2012.

[39] M. Ghosh. *Polyimides: Fundamentals and Applications*. Plastics Engineering. Taylor & Francis, 1996.

[40] G. Glass, B. McGaw, and M. Smith. *Meta-analysis in social research*. Sage Library of Social Research. Sage Publications, 1981.

[41] T. Handschuh. *Untersuchung des Betriebs- und Alterungsverhaltens von Blei-Säure-Akkumulatoren bei für Hybridantriebssysteme typischen Belastungen*. PhD thesis, Ulm University, 2007.

[42] HDMicroSystems. *Product Bulletin - PI-5878G - Wet Etch Applications*, 2009.

[43] S. He, M. M. Mench, and S. Tadigadapa. Thin film temperature sensor for real-time measurement of electrolyte temperature in a polymer electrolyte fuel cell. *Sensors and Actuactors A*, 125:170–177, 2006.

[44] L. Hedges and I. Olkin. *Statistical Methods for Meta-analysis*. Academic Press, 1985.

[45] D. A. P. Hersman. Investigative Update of Battery Fire Japan Airlines B-787 - Jan 7, 2013. Technical report, National Transportation Safety Board, 2013.

[46] T. Huedo-Medina, J. Sanchez-Meca, F. Martin-Martinez, and J. Botella. Assessing heterogeneity in meta-analysis: Q statistic or I2 index. *Physical Methods*, 11(2):193–206, 2006.

[47] Y. Inui, Y. Kobayashi, Y. Watanabe, Y. Watase, and Y. Kitamura. Simulation of temperature distribution in cylindrical and prismatic lithium ion secondary batteries. *Energy Conversion and Management*, 48(7):2103 – 2109, 2007. doi: 10.1016/j.enconman.2006.12.012.

[48] P. Keil. *Aging of Lithium-Ion Batteries in Electric Vehicles*. PhD thesis, Technical University of Munich, 2017.

[49] P. Keil, S. F. Schuster, J. Wilhelm, J. Travi, A. Hauser, R. C. Karl, and A. Jossen. Calendar aging of lithium-ion batteries. *Journal of The Electrochemical Society*, 163(9):A1872–A1880, 2016. doi: 10.1149/2.0411609jes.

[50] U. Kim, C. Shin, and C.-S. Kim. Effect of electrode configuration on the thermal behavior of a lithium-polymer battery. *Journal of Power Sources*, 180(2):909–916, 2008.

[51] R. Koch and A. Jossen. Temperature measurement of large format pouch cells with impedance spectroscopy. In *EVS28 International Electric Vehicle Symposium and Exhibition*, 2015.

[52] T. Kontschinsky. Methods for temperature measurement of a single battery cell. Master's thesis, Technical University of Munich, 2011.

[53] K. Kumaresan, G. Sikha, and R. E. White. Thermal model for a li-ion cell. *Journal of The Electrochemical Society*, 155(2):A164 – A171, 2008. doi: 10.1149/1.2817888.

[54] K. Kwon, C. Shin, T. Kang, and C.-S. Kim. A two-dimensional modeling of a lithium-polymer battery. *Journal of Power Sources*, 163(1):151–157, 2006.

[55] C.-Y. Lee, W.-J. Hsieh, and G.-W. Wu. Embedded flexible micro-sensors in MEA for measuring temperature and humidity in a micro-fuel cell. *Journal of Power Sources*, 181:237–243, 2008.

[56] C.-Y. Lee, S.-J. Lee, M.-S. Tang, and P.-C. Chen. In Situ Monitoring of Temperature inside Lithium-Ion Batteries by Flexible Micro Temperature Sensors. *Sensors*, 11:9942–9950, 2011.

[57] C.-Y. Lee, S.-J. Lee, Y.-M. Lee, M.-S. Tang, P.-C. Chen, and Y.-M. Chang. In situ monitoring of temperature using flexible micro temperature sensors inside polymer lithium-ion battery. In *7th IEEE International Conference on Nano/Micro Engineered and Molecular Systems (NEMS)*. IEEE, 2012. doi: 10.1109/nems.2012.6196871.

[58] M. D. Levi and D. Aurbach. Diffusion coefficients of lithium ions during intercalation into graphite derived from the simultaneous measurements and modeling of electrochemical impedance and potentiostatic intermittent titration characteristics of thin graphite electrodes. *The Journal of Physical Chemistry B*, 101(23):4641–4647, 1997. doi: 10.1021/jp9701911.

[59] Z. Li, J. Zhang, B. Wu, J. Huang, Z. Nie, Y. Sun, F. An, and N. Wu. Examining temporal and spatial variations of internal temperature in large-format laminated battery with embedded thermocouples. *Journal of Power Sources*, 241:536–553, 2013.

[60] B. Y. Liaw, E. Roth, R. G. Jungst, G. Nagasubramanian, H. L. Case, and D. H. Doughty. Correlation of arrhenius behaviors in power and capacity fades with cell impedance and heat generation in cylindrical lithium-ion cells. *Journal of Power Sources*, 119-121:874–886, 2003. doi: 10.1016/s0378-7753(03)00196-4.

[61] J. H. Lienhard IV and J. H. Lienhard V. *A Heat Transfer Textbook*. Phlogiston Press, 4 edition, 2011.

[62] H. Löhn. *Leistungsvergleich von Nieder- und Hochtemperatur-Polymerelektrolytmembran-Brennstoffzellen - Experimentelle Untersuchungen, Modellierung und numerische Simulation*. PhD thesis, Technische Universität Darmstadt, 2010.

[63] V. Lorentz, M. Wenger, J. Grosch, M. Giegerich, M. Jank, M. Marz, and L. Frey. Novel cost-efficient contactless distributed monitoring concept for smart battery cells. In *Industrial Electronics (ISIE), 2012 IEEE International Symposium on*, pages 1342–1347, 2012. doi: 10.1109/ISIE.2012.6237285.

[64] H. Maleki. Thermal stability studies of li-ion cells and components. *J. Electrochem. Soc.*, 146 (9):3224, 1999. doi: 10.1149/1.1392458.

[65] H. Maleki, S. Al Hallaj, J. R. Selman, R. B. Dinwiddie, and H. Wang. Thermal properties of lithium-ion battery and components. *Journal of The Electrochemical Society*, 146(3):947–954, 1999. doi: 10.1149/1.1391704.

[66] N. Martiny and A. Jossen. Challenges of battery systems in a tropical environment. 1st MSE Colloquium - Sustainable Energy Supply of the Future, Munich, Poster, 2011.

[67] N. Martiny, S. Arnold, and A. Jossen. Temperature Analysis of Li-Ion Cells for Safety Simulation. Kraftwerk Batterie 2012, Muenster, Presentation, 2012.

[68] N. Martiny, P. Osswald, C. Huber, and A. Jossen. Safety Management for Electric Vehicle Batteries in a Tropic Environment. Electric Vehicle Symposium 26, Los Angeles, California, 2012.

[69] N. Martiny, J. Geder, Y. Wang, W. Kraus, and A. Jossen. Development of a thin-film thermocouple matrix for in-situ temperature measurement in a lithium ion pouch cell. In *IEEE SENSORS*. IEEE, 2013. doi: 10.1109/icsens.2013.6688485.

[70] N. Martiny, A. Hornung, M. Schussler, and A. Jossen. A capacitively coupled data transmission system for resistance based sensor arrays for in-situ monitoring of lithium-ion battery cells. *IEEE SENSORS 2014 Proceedings*, 2014. doi: 10.1109/icsens.2014.6985053.

[71] N. Martiny, A. Rheinfeld, J. Geder, Y. Wang, and A. Jossen. Development of an all Kapton-based Thin-Film Thermocouple Matrix for In-Situ Temperature Measurement in a Lithium Ion Pouch Cell. *IEEE Sensors Journal*, 2014. doi: 10.1109/jsen.2014.2331996.

[72] N. Martiny, T. Mühlbauer, S. Steinhorst, M. Lukasiewycz, and A. Jossen. Digital data transmission system with capacitive coupling for in-situ temperature sensing in lithium ion cells. *Journal of Energy Storage*, 2015. doi: 10.1016/j.est.2015.10.001.

[73] S. Mathewson. *Experimental Measurements of LiFePO4 Battery Thermal Characteristics*. PhD thesis, University of Waterloo, 2014.

[74] J. R. Mcdonald. Impedance spectroscopy. *Annals of Biomedical Engineering*, 20:289–305, 1992.

[75] T. Mühlbauer. Development study and prototype implementation of a capacitively coupled digital data transmission system for in-situ sensors in lithium-ion pouch cells. Master's thesis, Technical University of Munich, 2015.

[76] M. S. K. Mutyala, J. Zhao, J. Li, H. Pan, C. Yuan, and X. Li. In-situ temperature measurement in lithium ion battery by transferable flexible thin film thermocouples. *Journal of Power Sources*, 260:43–49, 2014.

[77] A. M. Obukhov. Structure of the temperature field in turbulent flow. *ARMY BIOLOGICAL LABS FREDERICK MD*, Translation No. 334, 1968.

[78] H. Ohya, V. V. Kudryavtsev, and S. I. Semenova. *Polyimide Membranes: Applications, Fabrications and Properties*. CRC PR INC, 1997.

[79] A. Otto, S. Rzepka, T. Mager, B. Michel, C. Lanciotti, T. Günther, and O. Kanoun. Battery management network for fully electrical vehicles featuring smart systems at cell and pack level. In G. Meyer, editor, *Advanced Microsystems for Automotive Applications 2012*. Springer Berlin Heidelberg, 2012. doi: 10.1007/978-3-642-29673-4_1.

[80] T. W. Peter von Boeckh. *Wärmeübertragung - Grundlagen und Praxis*. Springer, 4 edition, 2011.

[81] R. Piasecki, M. Martin, and A. Plastino. Inhomogeneity and complexity measures for spatial patterns. *Physica A: Statistical Mechanics and its Applications*, 307(1-2):157–171, 2002. doi: 10.1016/s0378-4371(01)00591-x.

[82] B. Pruit and A. Okamura. Flexible strain gage array. Technical report, University of Stanford, 1998.

[83] B. Pruitt and A. Okamura. Flexible strain gage array - ee357 final report. `http://www-cdr.stanford.edu/~pruitt/ee357`, 1998. Last called 2017-07-12.

[84] L. Rade and B. Westergren. *Springers Mathematische Formeln* . Springer Science + Business Media, 3 edition, 2000. doi: 10.1007/978-3-642-57239-5.

[85] L. Raijmakers, D. Danilov, J. van Lammeren, M. Lammers, and P. Notten. Sensorless battery temperature measurements based on electrochemical impedance spectroscopy. *Journal of Power Sources*, 247:539–544, 2014. doi: 10.1016/j.jpowsour.2013.09.005.

[86] A. Reinfelder. Development of a sensor for in-cell temperature measurement of a li-ion pouch cell. Master's thesis, Technical University of Munich, 2012.

[87] A. Reinfelder, N. Martiny, and A. Jossen. Thermal In-Cell Measurement for Li-Ion Pouch Cells. In Proceedings of Conference on Future Automotive Technology, Munich, 2012.

[88] A. Rheinfeld, S. Erhard, S. Kosch, and A. Jossen. Modelling of temperature distribution within a large format Li-ion battery during discharge and its implications towards internal temperature sensor placement for designing safe battery systems. Kraftwerk Batterie Proceedings, Münster, Germany, 2014., 2014.

[89] R. R. Richardson, P. T. Ireland, and D. A. Howey. Battery internal temperature estimation by combined impedance and surface temperature measurement. *Journal of Power Sources*, 265: 254–261, 2014. doi: 10.1016/j.jpowsour.2014.04.129.

[90] *SPECIFICATION OF PRODUCT - Rechargeable Li-ion Polymer Battery- Model : SPB605060 (1900mAh)*. SAEHAN-ENERTECH. INC., 2006.

[91] U. Schilcher, M. Gyarmati, C. Bettstetter, Y. W. Chung, and Y. H. Kim. Measuring inhomogeneity in spatial distributions. *Proceedings of the Vehicular Technology Conference*, pages 2690–2694, 2008. doi: 10.1109/VETECS.2008.589.

[92] J. P. Schmidt, D. Manka, D. Klotz, and E. Ivers-Tiffée. Investigation of the thermal properties of a li-ion pouch-cell by electrothermal impedance spectroscopy. *Journal of Power Sources*, 196(19):8140–8146, 2011.

[93] J. P. Schmidt, S. Arnold, A. Loges, D. Werner, T. Wetzel, and E. Ivers-Tiffee. Measurement of the internal cell temperature via impedance: Evaluation and application of a new method. *Journal of Power Sources*, 243:110 – 117, 2013. doi: 10.1016/j.jpowsour.2013.06.013.

[94] A. Senner, H. Breimer, and H. Burkard. *Tabellenbuch Elektrotechnik*. Europa Lehrmittel, 1966.

[95] R. Spotnitz and J. Franklin. Abuse behavior of high-power, lithium-ion cells. *Journal of Power Sources*, 113(1):81 – 100, 2003. doi: 10.1016/s0378-7753(02)00488-3.

[96] R. Srinivasan, B. G. Carkhuff, M. H. Butler, and A. C. Baisden. Instantaneous measurement of the internal temperature in lithium-ion rechargeable cells. *Electrochimica Acta*, 56(17): 6198–6204, 2011. doi: 10.1016/j.electacta.2011.03.136.

[97] S. Steinhorst, M. Lukasiewycz, S. Narayanaswamy, M. Kauer, and S. Chakraborty. Smart cells for embedded battery management. *2014 IEEE International Conference on Cyber-Physical Systems, Networks, and Applications*, 2014. doi: 10.1109/cpsna.2014.22.

[98] H. Stöcker, editor. *Taschenbuch der Physik*. Harri Deutscher, 2000.

[99] H. Stöcker, editor. *Taschenbuch der Physik*. Verlag Harri Deutsch, 6 edition, 2010.

[100] T. R. Tanim, C. D. Rahn, and C.-Y. Wang. A temperature dependent, single particle, lithium ion cell model including electrolyte diffusion. *J. Dyn. Sys., Meas., Control*, 137(1):011005, 2014. doi: 10.1115/1.4028154.

[101] Targray. Aluminum Laminate Pouch. `http://www.targray.com/documents/pds-targray-aluminum-laminate-pouch.pdf`, 2011.

[102] W. Tiedemann and J. Newman. Current and potential distribution in lead-acid battery plates. In S. Gross, editor, *Proceedings of the Symposium on Battery Design and Optimization*, Princeton, NJ, 1979. The Electrochemical Society.

[103] P. A. Tipler and G. Mosca. *Physics for scientists and engineers*, volume 6. W. H. Freeman and Company, 2008.

[104] Y. Troxler, B. Wu, M. Marinescu, V. Yufit, Y. Patel, A. J. Marquis, N. P. Brandon, and G. J. Offer. The effect of thermal gradients on the performance of lithium-ion batteries. *Journal of Power Sources*, 247:1018–1025, 2014. doi: 10.1016/j.jpowsour.2013.06.084.

[105] L. O. Valøen and J. N. Reimers. Transport properties of $LiPF_6$-based li-ion battery electrolytes. *Journal of The Electrochemical Society*, 152(5):A882, 2005. doi: 10.1149/1.1872737.

[106] T. Waldmann, G. Bisle, B.-I. Hogg, S. Stumpp, M. A. Danzer, M. Kasper, P. Axmann, and M. Wohlfahrt-Mehrens. Influence of cell design on temperatures and temperature gradients in lithium-ion cells: An in operando study. *Journal of the Electrochemical Society*, 162(6):A921 – A927, 2015. doi: 10.1149/2.0561506jes.

[107] J. Wen, Y. Yu, and C. Chen. A review on lithium-ion batteries safety issues: Existing problems and possible solutions. *Materials Express*, 2(3):197–212, 2012. doi: 10.1166/mex.2012.1075.

[108] Y. Yang, X. Hu, D. Qing, and F. Chen. Arrhenius equation-based cell-health assessment: Application to thermal energy management design of a hev nimh battery pack. *Energies*, 6 (5):2709–2725, 2013. doi: 10.3390/en6052709.

[109] Y. Ye, Y. Shi, N. Cai, J. Lee, and X. He. Electro-thermal modeling and experimental validation for lithium ion battery. *Journal of Power Sources*, 199:227–238, 2012. doi: 10.1016/j.jpowsour.2011.10.027.

[110] J. Yi, U. Kim, C. Shin, T. Han, and S. Park. Three-Dimensional Thermal Modeling of a Lithium-Ion Battery Considering the Combined Effects of the Electrical and Thermal Contact Resistances between Current Collecting Tab and Lead Wire. *Journal of the Electrochemical Society*, 160(3):A437 – A443, 2013.

[111] X. Zhang, H. Choi, A. Datta, and X. Li. Design, fabrication and characterization of metal embedded thin film thermocouples with various film thicknesses and junction sizes. *Journal of Micromechanics and Microengineering*, 16:900–905, 2006.

[112] V. Zinth, C. von Lüders, M. Hofmann, J. Hattendorff, I. Buchberger, S. Erhard, J. Rebelo-Kornmeier, A. Jossen, and R. Gilles. Lithium plating in lithium-ion batteries at sub-ambient temperatures investigated by in situ neutron diffraction. *Journal of Power Sources*, 271:152–159, 2014. doi: 10.1016/j.jpowsour.2014.07.168.